PART I: A STUDY OF THE $Na^{23}(p, \alpha)Ne^{20}$ REACTION FOR PROTON BOMBARDING ENERGIES FROM 100 TO 450 KEV

PART II: A MEASUREMENT OF THE N^{12} AND B^{12} HALF-LIVES

Thesis by

Thornton Roberts Fisher

In Partial Fulfillment of the Requirements

for the Degree of

Doctor of Philosophy

California Institute of Technology

Pasadena, California

1963

ACKNOWLEDGEMENTS

The author is indebted to Professor Ward Whaling for continued guidance and supervision during the course of the experiment. Helpful suggestions on experimental technique were provided by Professors C. A. Barnes and R. W. Kavanagh, and the author is indebted to Professors W. A. Folwer and T. Lauritsen for valuable discussions and encouragement. It is a pleasure to acknowledge the help of Barbara Zimmerman in performing the calculations for the analysis of the B^{12} and N^{12} half-life data. The author is also grateful to Lionel Senhouse for providing the solid-state particle detector used in taking the $Na^{23}(p, \alpha)Ne^{20}$ data.

This research was supported in part by the joint program of the Office of Naval Research and the U. S. Atomic Energy Commission.

ABSTRACT

I

The $Na^{23}(p, \alpha)Ne^{20}$ reaction has been studied for proton bombarding energies in the range 100 to 450 kev. Four narrow, isolated resonances have been observed in this region at proton bombarding energies of 286, 338, 374, and 445 kev. Excitation functions have been taken at each of these resonances, and the alpha yield, width, and resonance energy has been determined for each resonance. On the basis of angular distribution measurements, spin and parity assignments have been made for the resonances at 286, 338, and 374 kev. Upper limits have been established for the non-resonant cross section factor S and for the alpha yield from any unobserved resonance in the energy region covered. This experimental data has been used to calculate reaction rates for the $Na^{23}(p, \alpha)Ne^{20}$ reaction in stars whose temperature is in the range 5 to 10 x 10^8 °K. This is the range of temperatures in which the carbon burning process takes place.

II

The half-lives of N^{12} and B^{12} have been measured with greater experimental precision than had been achieved in previous measurements. Using the improved values for the half-lives, accurate ft values have been calculated for the decays of N^{12} and B^{12} to the C^{12} ground state. It is found that $ft(N^{12})/ft(B^{12}) = 1.14 \pm 0.025$ implying that the ratio of the nuclear matrix elements $|\int \sigma|^2(B^{12})/|\int \sigma|^2(N^{12})$ is 1.14. The significance of the 14% difference in these matrix elements is discussed briefly.

TABLE OF CONTENTS

PART I

PART II

PART I.

A STUDY OF THE $Na^{23}(p, \alpha)Ne^{20}$ REACTION FOR PROTON BOMBARDING ENERGIES FROM 100 to 450 KEV

I. INTRODUCTION

The $Na^{23}(p, \alpha)Ne^{20}$ reaction ($Q = 2.38$ Mev[7]) has been studied by several investigators.[1, 2, 3, 4] Of these, only Flack et al. made measurements for proton bombarding energies below 500 kev. They found two resonances in this region, at 287 and 338 kev, and measured the alpha yield from these resonances at an angle of 90 degrees with respect to the incident proton beam. Recently interest has been focused on this reaction due to a paper by Reeves and Salpeter.[5] They analyze a carbon burning star, i.e. a star in which the primary source of energy release involves the collision of two C^{12} nuclei. The carbon burning sets in when the helium burning phase has ended and the subsequent gravitational contraction of the core has raised its temperature to 6 to 9×10^8 ^oK. The C^{12} collisions lead to the reactions $C^{12}(C^{12}, p)Na^{23}$ and $C^{12}(C^{12}, \alpha)Ne^{20}$, and as the carbon burning phase progresses, the protons and alpha particles thus liberated take part in a complicated network of interactions with the other constituents of the stellar gas.

In order to analyze the carbon burning process completely and obtain the relative abundances of the elements remaining when the carbon supply has been exhausted, it is necessary to know the following things: (1) the initial composition, density, and temperature of the core, (2) the cross section for the primary reaction $C^{12} + C^{12} \rightarrow Mg^{24*}$ and the branching ratio for the two principal modes of decay $Mg^{24*} \rightarrow Na^{23} + p$ and $Mg^{24*} \rightarrow Ne^{20} + \alpha$, (3) the reaction rates for other reactions which can take place as the carbon burning phase progresses. The present experiment was undertaken in order to obtain an accurate value for the reaction rate of the $Na^{23}(p, \alpha)Ne^{20}$ reaction, which is one of the most

important of the "other reactions" mentioned in (3). We will not concern ourselves with a discussion of points (1) and (2), which are discussed extensively in the original paper of Reeves and Salpeter and in a later paper by Cameron[6] on the carbon burning process. We may mention that Reeves and Salpeter assume an initial composition of equal amounts of C^{12}, O^{16}, and Ne^{20}. Cameron assumes an initial composition of 80% C^{12} and 20% O^{16}, taking advantage of the recent discovery that the 4.97 Mev level in Ne^{20} has $J^{\pi} = 2^{-}$, and that as a result a negligible amount of Ne^{20} is produced in helium burning.

The importance of the $Na^{23}(p, \alpha)Ne^{20}$ reaction in the carbon burning process is evident since the C^{12} collisions produce large amounts of Na^{23}. The rate of this reaction largely determines the final ratio of Na^{23} to Mg^{24} (see Reference (5)). This reaction rate was previously uncertain by a factor of 10 or 20 due to the sketchy nature of the data available in the proton energy region below 500 kev. We have carefully covered the region from 100 to 450 kev and measured the yields, widths, and resonance energies of four observed resonances. This information is to be found in table 1. For three of these resonances, we have been able to make spin and parity assignments on the basis of angular distributions (see figs. 18, 19, and 20). Our values for the reaction rate as a function of temperature for temperatures in the range 5 to 10 x 10^{8} ^{o}K are accurate to within 25% in all cases (see table 4).

II. EXPERIMENTAL PROCEDURE

Diagrams of the target chamber and associated equipment are shown in figs. 1 and 2. The proton beam from the 600 kev electrostatic accelerator at the Kellogg Radiation Laboratory was deflected magnetically to separate the protons from other mass components present, then passed through a 90 degree electrostatic analyzer. Emerging from the analyzer, the beam passed into the target chamber striking the target which was mounted on the end of a 1/2 in. diameter rod. A cold trap surrounded the target to reduce the build-up of contaminants during bombardment. The alpha particle counter was mounted at a distance of 5/8 in. from the target, and could be rotated symmetrically about an axis through the center of the target rod. A window placed just in front of the counter defined a solid angle of 0.100 steradians, determined by a measurement of the dimensions of the window and its distance from the target. The estimated uncertainty in this determination is ± 5%. The number of protons striking the target was measured by an electronic current integrator, discussed in section II D. The target was maintained at a potential of +300 volts to suppress secondary electron emission, and a ring located about four inches in front of the target was maintained at a potential of -300 volts to suppress electrons present in the beam. The various parts of the experimental arrangement will now be discussed separately in more detail.

A. Targets

The first targets which were tried were targets of pure sodium evaporated onto thick copper backings. Because of the reactivity of

pure sodium, the evaporation had to be done in the target chamber itself and equipment for doing this was part of the original experimental arrangement. These targets, however, did not hold up well under bombardments of several millicoulombs which were necessary because of the low yield of the reaction. A gradual decrease in the number of counts was observed when the proton energy was held constant and the target was bombarded with successive equal amounts of charge. This is illustrated in fig. 3. A second difficulty encountered with the pure sodium targets is illustrated in fig. 4. The trailing edge of the excitation function taken with the pure sodium target is considerably "smeared out." The target thickness is rather ambiguous, but is presumably several times the width of the resonance. One would expect the excitation function to be flat on top with well-defined front and back edges if the target were uniform. The reason for this apparent non-uniformity in the pure sodium targets has not been explained. Gradual oxidation of the sodium layer could account for the first difficulty mentioned above.

Sodium chloride targets did not suffer from either of the above difficulties, as can be seen from figs. 3 and 4. These targets were made by vacuum evaporation of the salt onto thick copper and silver backings, and were the ones used in taking the experimental data. The backings were polished to a mirror finish with emery paper and jeweler's rouge. Silver backings were used for some of the targets because they gave fewer counts due to contaminants than the copper backings.

Only one contaminant group was observed from the sodium chloride targets. This was an alpha group at 4 Mev which was identified as coming from the reaction $B^{11}(p, \alpha)Be^{8*}(2\alpha)$ (the $Na^{23}(p, \alpha)Ne^{20}$

reaction produces 2.3 Mev alpha particles at the corresponding proton energy and angle). The identification was made on the basis of the energy of the group and the fact that it exhibited a resonance at a proton bombarding energy of 160 kev, as illustrated in fig. 5. The energy spectrum of the alphas from this reaction is shown in fig. 6. The continuous energy distribution is due to the breakup of the Be^{8*} nucleus into two alpha particles. Because of this continuous energy distribution, it was necessary to correct the counting rates for the presence of this contaminant group, and the correction procedure is described in section III B. The source of the B^{11} contaminant was not determined.

We will give special consideration to the possibility of a small F^{19} contaminant because the reaction $F^{19}(p, \alpha)O^{16*}$ has a large cross section at the 340 kev resonance, very close in energy to the 338 kev resonance which we studied in the $Na^{23}(p, \alpha)Ne^{20}$ reaction. Fig. 7 shows the energy spectrum of the alphas from the Na^{23} reaction taken at the 338 kev resonance. Alpha particles from the $F^{19}(p, \alpha)O^{16*}$ reaction would make their appearance in channel 20 of this figure. Since no significant change was observed in the region around channel 20 as the proton energy was varied from 339 to 345 kev, the possibility of an F^{19} contaminant was not considered further.

B. Alpha Particle Counter

The alpha particles were detected in a silicon p-n junction counter. The good energy resolution, linear energy response, and small size of this counter made it ideal for our purposes. Such a counter requires a high gain low noise amplification system for its operation, and

a special low noise pre-amplifier obtained from E. Nordberg was used. The pre-amplifier output was fed into an Atomic Instrument model 304 C linear amplifier. The response of the counter, pre-amplifier, and amplifier combination to alpha particles from ThC' is shown in fig. 8.

The window in front of the counter (see fig. 2) served a dual purpose. The window defined the solid angle subtended by the counter, and it was covered by a foil which stopped elastically scattered protons from reaching the counter. This foil had to meet rigid specifications for thickness and uniformity. Commercially available foils were unsuitable in these respects, but it was found that a suitable foil could be constructed by superimposing several layers of commercial gold leaf. These foils were very uniform, since nonuniformities in the individual layers tended to average out, and the thickness could be varied in steps of 0.194 mg/cm^2, the thickness of an individual layer.

Fig. 7, which shows the alpha spectrum from the Na^{23} reaction, illustrates the importance of choosing the correct foil thickness. The pulses below channel 20 in the figure are due to counter noise and counts from protons straggling through the foil. If the foil is too thin, the proton pulses pile up and obscure the alpha peak. If the foil is too thick, the alpha particles will lose so much energy in the foil that the alpha pulses cannot be resolved from the noise background. The optimum foil thickness, the one which gives the best resolution of the alpha peak from the background edge, varies with proton bombarding energy. Therefore foils varying in thickness from 13 to 20 layers were used in our experiment (a 20 layer foil will just stop 400 kev protons). Since the range of

a proton is approximately the same as the range of an alpha particle of four times the energy, the resolution of the alpha peak from the background edge becomes poor as the elastically scattered proton energy approaches 1/4 the energy of the alpha particles. For this reason we were unable to obtain useful data for proton bombarding energies above 450 kev.

Because of the alpha peak from the B^{11} contaminant (also shown in fig. 7), two integral discriminators were used in taking data. Referring to fig. 7, typical bias settings for these two discriminators would be channel 25 and channel 90, with the upper discriminator biased just above the Na^{23} peak and the lower discriminator biased in the valley between the Na^{23} peak and the background edge. The resolution of the Na^{23} peak from the background edge was not always so good as in fig. 7, and in some cases small corrections had to be made for alpha particles lost outside the counting window. These corrections are discussed in sections III(C) and IV(B).

C. Electrostatic Analyzer

The electrostatic analyzer was of standard design and has been described previously by Wenzel[8]. The calibration procedure for such an analyzer is contained in many previous theses and will be dealt with only briefly here. The voltage between the analyzer plates is determined by measuring a small fraction of this voltage with a potentiometer. We have the following relation between the potentiometer reading V_{pot} and the energy E of a particle of charge Z which can be passed by the analyzer:

$$E = ZCV_{pot}\left(1 + \frac{E}{2Mc^2}\right) \qquad (1)$$

The calibration constant C can be determined by measuring the resonance energy of a known resonance. We determined C by observing the gamma rays from the 340.5 ± 0.3 kev[9] resonance in the reaction $F^{19}(p, \alpha\gamma)O^{16}$. The calibration measurements were made using thick CaF_2 targets evaporated on to tantalum backings. Frequent calibrations were performed during the course of the experiment.

The energy resolution of the analyzer is given approximately by the formula:

$$\frac{\Delta E}{E} = \frac{d}{R} \qquad (2)$$

where $\frac{\Delta E}{E}$ is the per cent energy resolution, d is the width of the slits at the top and bottom of the analyzer, and R is the radius of curvature of the analyzer. R = 30.25 inches in the present case, so that with the analyzer slits narrowed to 0.030 in. top and bottom an energy resolution of one part in one thousand was obtainable.

D. Current Integrator

The electronic current integrator measures the amount of charge deposited on the target by charging a capacitor to a pre-set voltage. When this voltage is reached, a relay is triggered which discharges the capacitor and the cycle can then be repeated. The current integrator is calibrated by measuring the amount of charge deposited per cycle.

Fig. 9 illustrates the current integrator and the calibration

apparatus. Point g is normally connected to the target rod. For calibration, the procedure is as follows. Point g is connected to point d and R_1 adjusted until the trigger for discharging capacitor C just fires. The corresponding voltage reading on meter M is designated by V_{max}. Then points g and d are disconnected, the capacitor C is shorted out, and the corresponding voltage reading on meter M is designated by V_{min}. Then, with the switch S open, point b is connected to point g, point a to point d, and the time T required for the capacitor to charge up to its maximum value is measured. We can now derive a relationship connecting V_{max}, V_{min}, T, and Q_0 where Q_0 is the charge required to charge up the capacitor to the point where the trigger fires.

If V(t) is the voltage across meter M as a function of time, and if the cathode follower arrangement is a linear amplifier we have:

$$V(t) = V_{min} + \frac{V_{max} - V_{min}}{CV_{max}} Q(t) \qquad (1)$$

where $Q(t)$ is the charge on the capacitor as a function of time and C is its capacitance. $CV_{max} = Q_0$, the charge required to fire the trigger. $Q(t)$ satisfies the differential equation:

$$E = R \frac{dQ(t)}{dt} + \frac{Q(t)}{C} - \left[V_{min} + \frac{V_{max} - V_{min}}{CV_{max}} Q(t) \right] \qquad (2)$$

where E and R are the known voltage and resistance shown in fig. 9. The solution of equation 2 satisfying the boundary condition $Q(0) = 0$ is:

$$Q(t) = C\left[E + V_{min}\right]\left[\frac{V_{max}}{V_{min}}\right]\left[1 - \exp\left(-\frac{V_{min}t}{V_{max}RC}\right)\right] \qquad (3)$$

Since $Q(T) = Q_0 = CV_{max}$, we have:

$$\frac{1}{1 + \frac{V_{min}}{E}} = \exp\left(-\frac{V_{min}T}{V_{max}RC}\right) \qquad (4)$$

Hence

$$\frac{Q_0}{T} = \frac{V_{min}}{R \ln\left(1 + \frac{V_{min}}{E}\right)} \qquad (5)$$

If $V_{min}/E << 1$ we can write approximately:

$$\frac{Q_0}{T} = \frac{E}{R}\left[1 + \frac{V_{min}}{2E}\right] \qquad (6)$$

The approximate values of E and R which were used in the actual calibration were E = 300 volts and R = 120 megohms. It was not necessary to determine both E and R accurately, but only to determine the ratio E/R accurately. This was done by connecting a precision resistor R' = 150 ± 0.1% kohms across points b and a as shown in fig. 9 and measuring the voltage V' across this resistor with a potentiometer. We then have E/R = V'/R'. The estimated uncertainty for the value of E/R thus obtained is ±2%. V_{min} was 20 volts so $V_{min}/E = 1/15$ and equation 6 could be used. An estimated uncertainty of ±2% was assigned to the value of the calibration constant Q_0, and this comes entirely from the uncertainty in E/R, since T can be

measured very accurately and the uncertainty in $V_{min}/2E$ has a negligible effect on Q_0. With a 1μf capacitor for C, we obtained Q_0 = 95.2 μ coulombs/integrator.

E. Procedure for Taking Data

In the proton energy range 100 to 450 kev, four resonances were observed at proton energies of 286, 338, 374, and 445 kev. The region of each resonance was studied with a $CaCl_2$ target to make sure none of the resonances was due to chlorine. Excitation functions were taken at each of these resonances and angular distributions were taken at the first three. At the 450 kev resonance, the resolution of the alpha peak from the elastically scattered protons was poor even for the optimum foil thickness, and the kinematic shift of the alpha peak with observation angle introduced large uncertainties in an angular distribution measurement. Therefore, no useful angular distribution data could be obtained at this resonance.

The four resonances studied were all narrow (< 5 kev) and well isolated so targets could be used which were thick compared to the width of a resonance but were thin enough to give only small contributions from lower resonances. The first step in taking data was to set the biases of the two discriminators (section B) with the aid of a spectrum such as fig. 7. This spectrum was always taken at the 286 or 338 kev resonances since the yield from these resonances was greater by a factor of ten than the yield from the other two. The difference in the counts recorded by the upper and lower discriminators, when corrected for counts from the B^{11} contaminant, gave the number of counts due to

alpha particles from the Na^{23} reaction. Excitation functions were taken by varying the incident proton energy in steps small compared with the width of a resonance. The off-resonance regions were carefully studied to obtain limits on yields from unobserved resonances and on the non-resonant cross section. The results of the excitation function measurements are discussed in section III.

Angular distributions were taken by holding the proton energy constant and rotating the alpha counter about the target rod axis. The maximum angular range was from 60 degrees to 150 degrees. The target surface was always positioned so that the normal to the surface bisected the angle between the proton beam and the alpha particle direction (see fig. 2). The 90 degree position of the alpha counter was determined by making measurements on both sides of the proton beam at the 338 kev resonance which has a large $\cos^2\theta$ anisotropy. Because of the proximity of the counter and target, an uncertainty of ± 4 degrees was assigned to this determination. The results of the angular distribution measurements are discussed in section IV.

III. EXCITATION FUNCTIONS

A. Introduction

The experimental data from an excitation function measurement are a set of numbers giving alpha particle counts per incident proton as a function of proton bombarding energy, all other experimental parameters remaining constant. We want to obtain from the data the yields, widths, and resonance energies of observed resonances and upper limits on yields from possible unobserved resonances. We also want to obtain an upper limit for the non-resonant cross section, by which we mean that part of the cross section not due to the observed resonances.

We have outlined our experimental procedure in section II E. Let us call the upper and lower discriminator biases V_U and V_L. For a proton energy E, we designate the number of counts recorded above V_L by $N_L(E)$ and the number of counts recorded above V_U by $N_U(E)$. V_U and V_L are chosen on the basis of a spectrum such as fig. 7 so that $N_U(E)$ contains no counts due to the alphas from the Na^{23} reaction and the main contribution to the difference $N(E) = N_L(E) - N_U(E)$ comes from the Na^{23} reaction.

B. Correction for Counts Due to B^{11} Contaminant

The first step in analyzing the data was to subtract from $N(E)$ the number of counts $N_B(E)$ due to the B^{11} contaminant (section II A). Fig. 6 shows the energy spectrum of the alpha particles from the $B^{11}(p,\alpha)Be^{8*}(2\alpha)$ reaction measured by Beckman, Huus, and Zupancic[10] at an angle of 97 degrees and a proton energy of 700 kev. A later measurement by Dearnaley et al.[11] at an angle of 90 degrees and

a proton energy of 530 kev is also shown and is almost identical. Dearnaley et al. report that the shape of the spectrum does not change appreciably as the proton bombarding energy is varied from 250 to 1400 kev. We assume that the shape in the energy range we are considering (100 to 450 kev) is that given in fig. 6.

The upper and lower discriminator biases, V_U and V_L, define the boundaries E_U and E_L of the region of fig. 6 which can contribute to N(E). This region, for a typical case, is indicated in the figure. If A is the area of this region and A_U is the area of the region above E_U, the ratio A/A_U is equal to the ratio $N_B(E)/N_U(E)$. (We assume $N_U(E)$ contains only counts from the B^{11} reaction, since no other alpha groups with energies greater than E_U were observed.) The above procedure determines $N_B(E)$ and subtracting this from N(E) leaves $N_{Na}(E)$, the counts due to the $Na^{23}(p, \alpha)Ne^{20}$ reaction.

The quantity $N_B(E)$ remained almost constant over the region of a resonance since the resonances were narrow. For this reason, possible errors in its determination have been neglected in the treatment of the resonances. Since it accounted for a large percentage of the off-resonance counting rates, its evaluation was important in establishing an upper limit for the non-resonant cross section.

C. Extraction of Yields, Widths, and Resonance Energies

If the numbers $N_{Na}(E)$ had a constant non-zero value N_{const} at energies below a resonance, this was subtracted to obtain the contribution of the resonance alone. For a particular resonance R let us call

the set of numbers thus obtained $N_R(E)$, $N_R(E) = N_{Na}(E) - N_{const}$. Let $N_R(\infty)$ and $N(\infty)$ be the values of $N_R(E)$ and $N(E)$ above the resonance. If necessary, the numbers $N_R(E)$ were multiplied by a factor C to correct for counts lost below the lower bias setting due to incomplete resolution of the Na^{23} alpha peak. The slight energy dependence of C was neglected, since the resonances were narrow.

In the extraction of the resonance parameters, the cross section in the region of a resonance was assumed to be given by the Breit-Wigner single level formula in the form of equation 2 appendix I. Since the exact treatment of the different resonances varied, we will consider each resonance separately.

286 kev Resonance

The excitation function at 90 degrees for this resonance is shown in fig. 10. The target thickness is greater than 35 kev. The points represent the numbers $N_R(E)$, and error bars indicate statistical uncertainties only. $N_B(E)$ was less than 1% of $N(\infty)$, N_{const} was negligible, and C was unity. The solid curve is a least squares fit following the procedure outlined in appendix I. Values obtained for the yield per steradian per proton at 90 degrees $Y(90)$, the width Γ, and the resonance energy E_R are listed in table 1.

It was also possible to measure the yield from this resonance with a pure sodium target. Since there are no lower energy resonances, an infinitely thick target could be used, and to measure the yield it was necessary to determine accurately only two points on the excitation

function, one above and one below the resonance energy. Therefore the two difficulties discussed in section II A did not interfere seriously with the yield measurement. The ratio of the yields from a sodium chloride target and a pure sodium target should be equal to $\epsilon_{Na}/(\epsilon_{Na}+\epsilon_{Cl})$. Using values for ϵ_{Na} and ϵ_{Cl} obtained in appendix II, the experimentally determined ratio agreed with $\epsilon_{Na}/(\epsilon_{Na}+\epsilon_{Cl})$ to within 5%. This agreement is considered satisfactory since an uncertainty of ±10% was allowed in the determination of ϵ_{Na} and ϵ_{cl} in appendix II. The yield measurement with the pure sodium target thus served as a check on our method for obtaining the values of ϵ_{Na} and ϵ_{Cl}.

338 kev Resonance

Fig. 11 shows the excitation function at 90 degrees for the 338 kev resonance. The target thickness, determined from the distance between the half-maximum points on an excitation function taken at the 286 kev resonance, is 35 kev for 320 kev protons. Corrections for $N_B(E)$ and N_{const} amounted respectively to 3% and 9% of $N(\infty)$ and the factor C was unity. The solid curve in fig. 11 is a least squares fit following the procedure of appendix I. Values of $Y(90)$, Γ and E_R are listed in table 1.

374 kev Resonance

The 374 kev resonance has been previously observed in the reaction $Na^{23}(p,\gamma)Mg^{24}$ (12) but not in the $Na^{23}(p,\alpha)Ne^{20}$ reaction due to its low yield. Fig. 12 shows the excitation function at 90 degrees

for this resonance. Corrections for $N_B(E)$ and N_{const} amounted respectively to 50% and 5% of $N(\infty)$, and the factor C was unity. The target thickness in fig. 12 is 10 kev for 350 kev protons, as determined from an excitation function taken at the 338 kev resonance.

Because of the low yield from this resonance, the experimental points in fig. 12 are sparse and the statistical uncertainties are large. It is also not immediately evident that we are justified in treating fig. 12 as a thick target excitation function. We therefore use a different procedure from that outlined in appendix I to obtain the parameters of this resonance.

To get the values of E_R and Γ, we assume the cross section is proportional to $[(E - E_R)^2 + \Gamma^2/4]^{-1}$. We know the target thickness is 10 kev, and using this fact we can calculate the theoretical shape of the excitation function for any values of E_R and Γ. The calculated curves for several different values of E_R and Γ are shown in figs. 12 and 13. The curves have all been normalized to the same height, and are symmetrical since we have neglected the straggling of protons in the target and possible non-uniformities in target thickness. These effects will tend to broaden the trailing edge of the experimental excitation function, as can be seen from fig. 4, so the experimental points at 386 and 394 kev are expected to lie somewhat above the theoretical curves in figs. 12 and 13.

In fig. 12, E_R has been chosen to give the best visual fit to the experimental points for a particular value of Γ. In fig. 13 Γ has been chosen to give the best visual fit to the experimental points for a particular value of E_R. On the basis of these figures, we take $\Gamma < 5$ kev,

E_R = 374 ± 1 kev. We would like to treat fig. 12 as a thick target excitation function to obtain Y(90), in which case Y(90) would be given by the point at 378 kev. To justify this procedure, we make use of the width measurements of previous investigators. The value 374 ± 1 kev for E_R establishes this resonance as identical to the resonance reported in $Na^{23}(p, \gamma)Mg^{24}$ reaction by Hancock and Verdaguer[12] and by Wagner and Heitzman[13]. Hancock and Verdaguer report E_R = 373.5 ± 0.4 kev, Γ = 2 ± 1 kev; Wagner and Heitzman report E_R = 373.7 ± 0.4 kev, Γ = 60 ± 20 ev. We therefore assume that the true value of Γ is much less than the 5 kev limit which we have established on the basis of our data, and treat fig. 12 as a thick target excitation function. The value of Y(90) obtained from the point at 378 kev is listed in table 1.

445 kev Resonance

This resonance has not been observed previously in the reaction $Na^{23}(p, \alpha)Ne^{20}$, but has been reported in the reaction $Na^{23}(p, \gamma)Mg^{24}$ [12]. However, Wagner and Heitzman[13] in the most recent study of this reaction have ascribed the resonance to chlorine rather than Na^{23}. Whether or not there is a resonance at this energy in the $Na^{23}(p, \gamma)Mg^{24}$ reaction, our data leave no doubt that a resonance does exist at this energy in the $Na^{23}(p, \alpha)Ne^{20}$ reaction.

Because of the incomplete resolution of the alpha peak, 400 channel analyzer spectra were taken at each proton energy. This enabled us to make certain that elastically scattered protons were not contributing

counts to N(E). Three such spectra are shown in fig. 14. In the spectrum at E = 446 kev, the position of the alpha peak corresponds to the calculated position of alpha particles from Na^{23}, which would have an energy of 2.22 Mev. Alpha particles from Cl^{37}, which would have an energy of 3.0 Mev, would appear in channel 70; alpha particles from Cl^{35}, which would have an energy of 1.95 Mev, would fall in channel 15 and be obscured by the background of elastically scattered protons. (We remind the reader that the alpha particles pass through a foil, and the energies of alpha particles from Cl^{35}, Na^{23}, and Cl^{37} after passing through this foil are reduced to 350, 670, and 1800 kev.)

The excitation function at 140 degrees is shown in fig. 15. (Placing the counter at 140 degrees rather than 90 degrees gave better resolution of the alpha peak.) The target thickness, as determined from an excitation function at the 338 kev resonance, is 15 kev for 355 kev protons. $N_B(E)$ and N_{const} amounted to 25% and 20% of $N(\infty)$. The lower discriminator bias V_L was set at channel 25 in fig. 14, and the correction factor C was determined by assuming that the shape of the alpha peak was symmetrical about its maximum. C was equal to 1.35, and an uncertainty of $\pm$ 15% was allowed.

In fig. 15, the target thickness is clearly much greater than the width of the resonance, so we treat this as a thick target excitation function. The excitation function rises from zero at 444 kev to almost its maximum value at 446 kev. We therefore take E_R as 445 $\pm$ 1 kev, and place an upper limit of 2 kev on the width Γ. We determine Y(140), the yield per steradian per proton at 140 degrees, from the two points

at 448 and 453 kev, and this quantity is listed in table 1.

D. Discussion of Errors

We summarize the sources of error considered in the determination of the resonance parameters as follows:

1) Determination of yields.

   a) Statistical uncertainty.
   b) Solid angle determination.
   c) Current integrator calibration.
   d) Uncertainty in correction factor C.
   e) Error introduced by treating finite target as infinite.

2) Determination of widths.

   a) Statistical uncertainty.
   b) Finite electrostatic analyzer resolution.

3) Determination of resonance energies.

   a) Statistical uncertainty.
   b) Electrostatic analyzer calibration.
   c) Contaminant buildup on target surface.

The magnitudes of the above sources of uncertainty are shown in table 1 for each resonance. 1(e), 2(b), and 3(c) are negligible in all cases. The other uncertainties are all independent, so we can combine them by taking the square root of the sum of their squares to obtain the total uncertainty in a particular case, and this has been done in table 1.

E. Upper Limits on Non-Resonant Cross Section and Yields From Other Resonances

In the off-resonance regions, the numbers $N_{Na}(E)$ (counter angle 90 degrees) were reduced to the differential cross section at 90 degrees, $(d\sigma(E)/d\Omega)_{90^\circ}$. Cross sections, solid angles, and angles appearing in the following discussion refer to the lab system. We have the relation:

$$N_{Na}(E) = \Omega_L n \int_{E-\Delta E}^{E} \frac{1}{\epsilon(E')} \left(\frac{d\sigma(E')}{d\Omega}\right)_{90^\circ} dE' \qquad (1)$$

where Ω_L is the solid angle of the counter, n is the number of incident protons, and ΔE is the target thickness. The determination of the stopping cross section ϵ is discussed in appendix II. To use equation 1, we make the approximation that the integrand is a linear function of the energy:

$$N_{Na}(E) = \Omega_L n \left(\frac{1}{\epsilon(E - \frac{\Delta E}{2})}\right) \left(\frac{d\sigma(E - \frac{\Delta E}{2})}{d\Omega}\right)_{90^\circ} (\Delta E) \qquad (2)$$

The quantity $\left(\frac{d\sigma(E)}{d\Omega}\right)_{90^\circ}$ contains the contribution of the non-resonant cross section $\left(\frac{d\sigma_{NR}(E)}{d\Omega}\right)_{90^\circ}$ plus small contributions from the observed resonances. The contribution of a resonance is assumed to be given by:

$$\left(\frac{d\sigma_R(E)}{d\Omega}\right)_{90^\circ} = Y(90) \frac{\epsilon(E_R)}{2\pi} \frac{\Gamma}{(E-E_R)^2 + \frac{\Gamma^2}{4}} \frac{\Gamma_p(E)}{\Gamma_p(E_R)} \qquad (3)$$

i.e. by the Breit-Wigner single-level formula in the form of equation 2 appendix I. The energy dependence of the proton width Γ_p is included since we are interested in values of E for which $\Gamma_p(E)/\Gamma_p(E_R)$ can differ considerably from unity. At the low energies we are considering, $\Gamma_p(E)/\Gamma_p(E_R) = \exp\{-2\pi\eta(E) + 2\pi\eta(E_R)\}$ where η is the coulomb factor for the proton, $\eta = z_1 z_2 e^2/\hbar V$. We can calculate the resonance contributions using the values for $Y(90)$, Γ, and E_R obtained in section C

and thus obtain $\left(\frac{d\sigma_{NR}(E)}{d\Omega}\right)_{90^\circ} = \left(\frac{d\sigma(E)}{d\Omega}\right)_{90^\circ} - \sum_R \left(\frac{d\sigma_R(E)}{d\Omega}\right)_{90^\circ}$. The experimental values of $\left(\frac{d\sigma_{NR}(E)}{d\Omega}\right)_{90^\circ}$ are plotted in fig. 16. Error bars represent statistical errors.

The non-resonant cross section is assumed to be isotropic so that $\sigma_{NR}(E) = 4\pi\left(\frac{d\sigma_{NR}(E)}{d\Omega}\right)_{90^\circ}$. For application to the calculation of reaction rates, it is convenient to express the non-resonant cross section in terms of the center of mass energy E_{CM} and the cross section factor S which is almost energy independent:

$$\sigma_{NR}(E_{CM}) = \frac{S}{E_{CM}} \exp(-2\pi\eta) \qquad (4)$$

The solid curve in fig. 16 corresponds to the value 100 Mev barns for S, and we take this as an upper limit for S on the basis of our data.

The upper limit placed on yields from possible resonances other than those observed in the energy region 100 to 450 kev is listed in table 1. To arrive at this limit, it was assumed that any such resonance would be much narrower than the thickness of the targets used. There are three known states in Mg^{24} lying in the energy range covered from which no alpha yield was detected. Two have been observed as resonances at 251 and 308 kev in the reaction $Na^{23}(p,\gamma)Mg^{24}$ (12). The third has been found in the reaction $Ne^{20}(\alpha,\alpha)Ne^{20}$ (14) and requires protons of about 180 kev energy for its formation. The failure to observe any alpha yield from the 251 and 308 kev resonances can be explained if these states have the wrong spin and parity to decay into two spin zero particles. The alpha scattering resonance, however, would be expected to appear also

in the $Na^{23}(p, \alpha)Ne^{20}$ reaction.

Fig. 17 shows an excitation function covering the region from 120 to 220 kev. The target is 40 kev thick for 325 kev protons. There is some evidence for a resonance at 170 kev, but we make no definite claim on the basis of fig. 17 due to the large statistical uncertainties and the long (as much as 1 hour per point) periods of bombardment which were required to obtain the points. If a resonance does exist in the region around 170 kev, the alpha yield per steradian per incident proton at 90°, Y(90), is less than 3×10^{-14}.

Table 1

Resonance Parameters for Resonances in the $Na^{23}(p, \alpha)Ne^{20}$ Reaction (See Section III D for Identification of Sources of Error)

Resonance	Parameter	Sources of Experimental Error	Experimental Value
286 kev	Y(90)	1(a) 1.5%; 1(b) 5% 1(c) 2%	$(1.70 \pm 0.1) \times 10^{-12}$
	Γ	2(a) 20%	1.75 ± 0.35 kev
	E_R	3(a) 0.04% 3(b) 0.15%	285.9 ± 0.5 kev
338 kev	Y(90)	1(a) 3%; 1(b) 5% 1(c) 2%	$(1.77 \pm 0.1) \times 10^{-12}$
	Γ	2(a) 25%	0.7 ± 0.2 kev
	E_R	3(a) 0.04% 3(b) 0.15%	338.6 ± 0.6 kev
374 kev	Y(90)	1(a) 15%; 1(b) 5% 1(c) 2%	$(1.3 \pm 0.2) \times 10^{-13}$
	Γ		< 5 kev
	E_R	3(a) $\pm$ 1 kev	374 ± 1 kev
445 kev	Y(140)	1(a) 10%; 1(b) 5% 1(c) 2%; 1(d) 15%	$(2.2 \pm 0.45) \times 10^{-13}$
	Γ		< 2 kev
	E_R	3(a) $\pm$ 1 kev	445 ± 1 kev
Unobserved Resonances 120 - 450 kev	Y(90)		$< 3 \times 10^{-14}$

IV. ANGULAR DISTRIBUTIONS

A. Theory

The general theory of angular correlations and distributions has been worked out by Blatt and Biedenharn[15]. We are interested here in the special case where a nuclear reaction, $Na^{23}(p, \alpha)Ne^{20}$, proceeds through a single compound nucleus level having definite spin and parity J^{π}. A previous application of the theory to the $Na^{23}(p, \alpha)Ne^{20}$ reaction has been made by Stelson[4], and we have repeated the calculations independently to check his results. We believe there are a few errors in the figures he has published, but most of our calculations are in agreement with his and the differences occur in terms which prove to be unimportant in the analysis of our experimental results.

The differential reaction cross section in the center of mass system can be written in the form

$$\frac{d\sigma}{d\Omega} = \varphi(E) \sum_{L} \frac{B_L}{B_0} P_L(\cos\theta) \qquad (1)$$

Here $\varphi(E)$ is a function of incident proton energy which need not be written explicitly. $P_L(\cos\theta)$ is the Legendre polynomial of order L. The coefficients B_L are given, in general, by a summation over all possible values of incident channel spin s and exit channel spin s', but since we have $s' = 0$ we can write them as a sum over s alone:

$$B_L = \sum_{s} B_L(s) \qquad (2)$$

Since the spin of Na^{23} is 3/2, the possible values of s are 1 and 2.

$B_L(s)$ is given by

$$B_L(s) = (-)^s f(E) Z(JJJJ, 0L) \Gamma_a \sum_{\ell_1=|J-s|}^{|J+s|} \sum_{\ell_2=|J-s|}^{|J+s|} Z(\ell_1 J \ell_2 J, s, L) g_{s\ell_1} g_{s\ell_2} \cos [\xi_{\ell_1} - \xi_{\ell_2}] \qquad (3)$$

which is the simplified form which equation 5.9 of Blatt and Biedenharn takes when $s' = 0$. The function $f(E)$ is not written explicitly since it will cancel in the ratio B_L/B_0. The Z's are well-known quantities which have been extensively tabulated[16]. The quantities $g_{s\ell}$ are defined by $g_{s\ell} = \pm(\Gamma_{s\ell})^{1/2}$ where $\Gamma_{s\ell}$ is the partial width for the formation of the state J^π by protons with channel spin s and orbital angular momentum ℓ. Γ_a is the width for the decay of the state J^π into $Ne^{20} + a$. The ξ_ℓ's are defined by:

$$\exp(2i\xi_\ell) = \frac{(\ell + i\eta)!}{(\ell - i\eta)!} \left[\frac{G_\ell(kR) - iF_\ell(kR)}{G_\ell(kR) + iF_\ell(kR)} \right] \qquad (4)$$

where k is the wave number for the proton, R is the interaction radius, and F_ℓ and G_ℓ are the regular and irregular coulomb wave functions. η is the coulomb factor for the proton, $\eta = z_1 z_2 e^2/\hbar V$. If $G_\ell \gg F_\ell$, which is true for the energies we will be considering, the term in brackets in equation 4 can be replaced by 1.

The Z's vanish unless certain selection rules are satisfied, and this greatly simplifies the evaluation of expression 3. The selection rules are $L \leq 2J$, $L \leq \ell_1 + \ell_2$ and $\ell_1 + \ell_2 + L$ even. Because the

compound state has a definite parity π, we must have $(-)^{\ell_1} = (-)^{\ell_2} = \pi$ which implies $\ell_1 + \ell_2$ must be even. The preceding remarks show that B_L is non-vanishing only if L is even and less than 2J.

Equation 4 which defines ξ_ℓ is an unwieldy expression to handle, but we can derive from it a simple expression for the quantity $\xi_{\ell+2} - \xi_\ell$ which is all we will need:

$$\xi_{\ell+2} - \xi_\ell = \tan^{-1} \frac{\eta}{\ell+1} + \tan^{-1} \frac{\eta}{\ell+2} \qquad (5)$$

Using equations 3 and 5 we are now in a position to calculate theoretical values of B_L/B_0 for any value of J. By comparing these with the experimental values measured at a particular resonance, we hope to learn the spin of the compound Mg^{24} state involved. The parity will be given by $\pi = (-)^J$ since the exit channel spin s' is zero.

Table 2 gives calculated expressions for the angular distribution coefficients B_L/B_0 for values of $J^\pi = 0^+, 1^-, 2^+, 3^-, 4^+$ and 5^-. The expressions involve ratios of the g's, such as g_{11}/g_{13}, which are left in as parameters since it is not possible to calculate them. The quantity $\cos(\xi_{\ell+2} - \xi_\ell)$ is not evaluated explicitly in these expressions since it is a function of proton energy. For any desired energy, it can be evaluated from equation 5. In table 2, as is indicated, we have neglected some terms in the calculated angular distribution coefficients for $J^\pi = 2^+$ and 5^-. This omission will be justified when we apply the formulas to a particular case.

In using table 2 to obtain a spin and parity assignment from an experimental angular distribution measurement, we will follow a pro-

Table 2

Angular Distribution Coefficients for $Na^{23}(p, \alpha)Ne^{20}$ Reaction

J^π	B_2/B_0
0^+	0
1^-	$\dfrac{-(g_{11}/g_{21})^2 + 0.2 + 0.8(g_{23}/g_{21})^2 + 2.94(g_{23}/g_{21})\cos(\xi_3-\xi_1)}{1 + (g_{11}/g_{21})^2 + (g_{23}/g_{21})^2}$
2^{+*}	$\dfrac{-0.31(g_{22}/g_{20})^2 + 0.71(g_{12}/g_{20})^2 + 2.38(g_{22}/g_{20})\cos(\xi_2-\xi_0)}{1 + (g_{22}/g_{20})^2 + (g_{12}/g_{20})^2}$
3^-	$\dfrac{0.8 + 0.42(g_{23}/g_{21})^2 + (g_{13}/g_{21})^2 - 1.34(g_{23}/g_{21})\cos(\xi_3-\xi_1)}{1 + (g_{23}/g_{21})^2 + (g_{13}/g_{21})^2}$
4^+	$\dfrac{1.02 + 0.74(g_{24}/g_{22})^2 + 1.1(g_{14}/g_{22})^2 + 0.5(g_{24}/g_{22})\cos(\xi_4-\xi_2)}{1 + (g_{24}/g_{22})^2 + (g_{14}/g_{22})^2}$
5^{-**}	1.11

J^π	B_4/B_0
0^+	0
1^-	0
2^{+*}	$\dfrac{-1.71(g_{12}/g_{20})^2 + 0.73(g_{22}/g_{20})^2}{1 + (g_{12}/g_{20})^2 + (g_{22}/g_{20})^2}$
3^-	$\dfrac{-0.82(g_{23}/g_{21})^2 + 0.27(g_{13}/g_{21})^2 + 3.4(g_{23}/g_{21})\cos(\xi_3-\xi_1)}{1 + (g_{23}/g_{21})^2 + (g_{13}/g_{21})^2}$
4^+	$\dfrac{0.55 - 0.22(g_{24}/g_{22})^2 + 0.73(g_{14}/g_{22})^2 + 1.5(g_{24}/g_{22})\cos(\xi_4-\xi_2)}{1 + (g_{24}/g_{22})^2 + (g_{14}/g_{22})^2}$
5^{-**}	0.31

Table 2 (Continued)

J^{π}	B_6/B_0
0^+	0
1^-	0
2^+	0
3^-	$\dfrac{1.26(g_{23}/g_{21})^2 - 2.27(g_{13}/g_{21})^2}{1 + (g_{23}/g_{21})^2 + (g_{13}/g_{21})^2}$
4^+	$\dfrac{-0.93(g_{24}/g_{22})^2 - 0.09(g_{14}/g_{22})^2 + 3.9(g_{24}/g_{22})\cos(\xi_4 - \xi_2)}{1 + (g_{24}/g_{22})^2 + (g_{14}/g_{22})^2}$
5^{-**}	0.40

J^{π}	B_8/B_0
0^+	0
1^-	0
2^+	0
3^-	0
4^+	$\dfrac{1.73(g_{24}/g_{22})^2 - 2.74(g_{14}/g_{22})^2}{1 + (g_{24}/g_{22})^2 + (g_{14}/g_{22})^2}$
5^{-**}	0

* Terms involving g_{24} neglected.

** Terms involving g_{25}, g_{27}, and g_{15} neglected.

cedure of systematic elimination; we hope to be able to eliminate all but one possibility and obtain a unique assignment. We will rely on some arguments based on the theory of reduced widths, which will now be briefly described.

In the formalism of Wigner, the partial width $\Gamma_{s\ell}$ for protons with channel spin s and orbital angular momentum ℓ is written as:

$$\Gamma_{s\ell} = 2kR\,T_\ell \quad \frac{3}{2}\,\frac{\hbar^2}{MR^2} \quad \theta^2_{s\ell} \tag{6}$$

R is the channel radius, M is the reduced mass, and the penetration factor T_ℓ is defined by $T_\ell = [F^2_\ell(kR) + G^2_\ell(kR)]^{-1}$. $\theta^2_{s\ell}$ is called the reduced width and obeys the condition $\sum_{s,\ell} \theta^2_{s\ell} \leq 1$, which has been well verified experimentally. The value of $\Gamma_{s\ell}$ obtained by setting $\theta^2_{s\ell} = 1$ in equation 6 is called the Wigner limit for $\Gamma_{s\ell}$ which we will designate by $\Gamma_{s\ell}$ (Wigner). The total proton width Γ_p is equal to the sum of all the partial widths $\Gamma_p = \sum_{s,\ell} \Gamma_{s\ell}$. We have $\Gamma_p > \Gamma_p\Gamma_\alpha/\Gamma$, and experimental values of $\omega\Gamma_p\Gamma_\alpha/\Gamma$ are tabulated in table 3. The $\Gamma_{s\ell}$'s must then satisfy the set of equations:

$$\begin{aligned} &\sum_{s,\ell} \Gamma_{s\ell} = \Gamma_p(\text{exp}) > \Gamma_p\Gamma_\alpha/\Gamma \\ &\sum_{s,\ell} \Gamma_{s\ell}/T_\ell \leq 2kR \quad \frac{3}{2}\,\frac{\hbar^2}{MR^2} \end{aligned} \tag{7}$$

As an illustration of how we will use equations 7 in determining a unique spin and parity assignment, suppose we are considering the assignment $J^\pi = J^{\pi}_o$ and ℓ_o is the minimum value of ℓ by which the

state $J_o^{\pi_o}$ can be made. If $\Gamma_p(\text{exp}) > \Gamma_{s\ell_o}(\text{Wigner})$ equations 7 cannot be satisfied and we can rule out $J_o^{\pi_o}$ as a possible assignment. This type of argument will enable us to rule out values of J greater than a certain value. It may occur that $\Gamma_p(\text{exp}) < \Gamma_{s\ell_o}(\text{Wigner})$ but $\Gamma_p(\text{exp}) > \Gamma_{s\ell_o+2}(\text{Wigner})$ in which case equations 7 impose a restriction on the magnitude of $\Gamma_{s\ell_o+2}/\Gamma_{s\ell_o}$ and hence on $g_{s\ell_o+2}/g_{s\ell_o}$. With the aid of this restriction, we may be able to use the expressions in table 2 to eliminate $J_o^{\pi_o}$ as a possible assignment when we could not have done so otherwise.

We can place a more drastic restriction on the parameters $g_{s\ell+2}/g_{s\ell}$ by assuming that $\theta^2_{s\ell}$ does not depend on s and ℓ. This will be the case if the incident proton shares its excitation energy with many other nucleons in reaching the final compound nucleus configuration. On the other hand, if the incident proton retains all the energy of excitation and goes into a well-defined single-particle orbit, all the $\theta_{s\ell}$'s except one will be zero. At the high excitation energies (17 Mev) which we will be considering, however, we may expect the first picture to be more nearly correct.

The assumption that $\theta^2_{s\ell}$ is independent of s and ℓ implies that $\left|\frac{g_{s\ell+2}}{g_{s\ell}}\right| = \left(\frac{T_{\ell+2}}{T_\ell}\right)^{1/2}$ which is small (0.08 for $\ell = 0$, 0.03 for $\ell = 1$). With this assumption, then, the main contribution to the coefficients B_L/B_0 will come from the lowest ℓ value by which the state J^π can be made. We will be glad if we can find an assignment for J^π which does not violate the above assumption since it is a reasonable one, but will try to avoid using it to eliminate other possible assignments.

B. Experimental Determination of Angular Distribution Coefficients

Angular distributions were taken at the 286, 338, and 374 kev resonances. In each case, the angular distribution was measured at two energies, one above and one below the resonance energy. By subtraction, the angular distribution of alpha particles from the particular resonance in question was obtained. We call this set of numbers $N_R(\theta_L)$, where θ_L refers to the angle of the counter in the lab system. The numbers $N_R(\theta_L)$ must be corrected for the loss of counts below the lower bias setting, and transformed to the center of mass system before further analysis. We write the corrected values in the center of mass system as $\overline{N}_R(\theta)$, where:

$$\overline{N}_R(\theta) = C(\theta_L)G(E,\theta_L)N_R(\theta_L) \qquad (1)$$

The correction factor $C(\theta_L)$ has the same significance as the factor C defined in section III C, but must be written here as a function of θ_L since the alpha peak is shifted considerably as the counter angle is varied. It was always unity for $\theta_L < 135^\circ$ and was never greater than 1.15. The factor $G(E,\theta_L)$ appears in equation 1 because the solid angle subtended by the counter varies with angle in the center of mass system. Formulas for calculating $G(E,\theta_L)$ have been worked out by many authors. We give here the expression of Richards:[17]

$$G(x,\theta_L) = [1 - x^2\sin^2\theta_L]^{1/2}[x\cos\theta_L + (1-x^2\sin^2\theta_L)^{1/2}]^{-2}$$

$$x^2(E) = \frac{m_1 m_2}{m_0 m_3}\left[1 + \frac{m_1+m_0}{m_0}\frac{Q}{E}\right]^{-1} \qquad (2)$$

The subscripts 1 and 2 refer to the incident and emitted particle; the subscripts 0 and 3 refer to target and residual nuclei. E is the kinetic energy of the incident particle in the lab system. The quantity $G(E, \theta_L)$ was always close to unity in our case. For $E = 374$ kev $G(E, \theta_L)$ ranged from 0.97 at 60° to 1.06 at 150°.

The numbers $\overline{N}_R(\theta)$ were fitted by least squares to an expression of the form $A_0'(1 + \frac{A_2'}{A_0'}\cos^2\theta + \frac{A_4'}{A_0'}\cos^4\theta)$. B_2'/B_0' and B_4'/B_0' were calculated from A_2'/A_0' and A_4'/A_0'; this procedure proved to be simpler than fitting the expression $B_0'(1 + \frac{B_2'}{B_0'}P_2(\cos\theta) + \frac{B_4'}{B_0'}P_4(\cos\theta))$ originally. We have marked the above quantities with primes to indicate that they are not the true angular distribution coefficients since they are not corrected for the smearing out of the angular distribution due to the finite size of the counter and target spot. We shall refer to this correction as the finite geometry correction, and now proceed to desribe two procedures which we used to estimate it.

If the true angular distribution is of the form $1 + \frac{B_2}{B_0}P_2(\cos\theta) + \frac{B_4}{B_0}P_4(\cos\theta)$ the angular distribution which will be observed with finite experimental geometry is $1 + Q_2(\theta)\frac{B_2}{B_0}P_2(\cos\theta) + Q_4(\theta)\frac{B_4}{B_0}P_4(\cos\theta)$. For the special case of a circular counter and a point target spot, the Q's are constants and an exact expression for them is given by Rose:[18]

$$Q_L = \frac{P_{L-1}(\cos\gamma) - \cos\gamma\, P_L(\cos\gamma)}{(L+1)(1-\cos\gamma)} \qquad (3)$$

where γ is the half-angle subtended by the counter. Our actual geometry is shown in fig. 2. If we neglect the finite size of the target spot and approximate the counter shape by a circle 1/4 in. in diameter,

equation 3 gives $Q_2 = 0.98$ and $Q_4 = 0.90$. These values are close to unity, which is another way of saying that the finite geometry correction is small for this simplified picture of our actual geometry. For this reason, we may expect the correction to be small in the actual case, and should not introduce much error by using the simplified picture. We then obtain $\frac{B_2}{B_0} = \frac{1}{0.98}\frac{B'_2}{B'_0}$ and $\frac{B_4}{B_0} = \frac{1}{0.90}\frac{B'_4}{B'_0}$ as the corrected values for the angular distribution coefficients.

We have also worked out the finite geometry correction for the actual geometry of fig. 2, with the exception that the counter shape was approximated by a rectangle of dimensions 1/4 x 3/16 in. In this case, we cannot take advantage of the orthogonality properties of the Legendre polynomials, and it is simpler to work out the correction to A'_2/A'_0 and A'_4/A'_0. We write the true angular distribution in the form $1 + \frac{A_2}{A_0}\cos^2\theta + \frac{A_4}{A_0}\cos^4\theta$, and the angular distribution which will be observed with finite geometry is $1 + f_2(\theta)\frac{A_2}{A_0}\cos^2\theta + f_4(\theta)\frac{A_4}{A_0}\cos^4\theta$. The quantities $f_2(\theta)$ and $f_4(\theta)$ are not constants and no simple exact expression for them can be given, but we have evaluated the appropriate integrals approximately. We obtain the result $f_2(\theta)\cos^2\theta \approx 0.97\cos^2\theta$ and $f_4(\theta)\cos^4\theta \approx 0.95\cos^4\theta$ for $60^\circ \leq \theta \leq 150^\circ$ so $\frac{A_2}{A_0} = \frac{1}{0.97}\frac{A'_2}{A'_0}$ and $\frac{A_4}{A_0} = \frac{1}{0.95}\frac{A'_4}{A'_0}$. The two procedures described for making the finite geometry corrections gave results which differed by less than 2% for the final values of B_L/B_0, and in practice it was unimportant which procedure was adopted.

The experimental angular distributions are shown in figs. 18 to 20. The points represent the numbers $\overline{N}_R(\theta)$ and error bars represent

statistical errors. Two angular distributions were taken for the 374 kev resonance because of the large statistical errors in the points, but only one is shown. The uncertainties quoted in the values of B_2/B_0 and B_4/B_0 include statistical uncertainties and the uncertainty of $\pm 4^\circ$ in the determination of the 90 degree position of the counter.

C. Spin and Parity Assignments

We will organize this section by listing, under each resonance, the assignments eliminated on the basis of the theoretical arguments of section A together with the reason for their elimination.

286 kev Resonance

The experimentally measured values of the angular distribution coefficients are $B_2/B_0 = 0.09 \pm 0.06$ and $B_4/B_0 = 0$.

J^π	Reason Eliminated
0^+	This assignment gives $B_2/B_0 = 0$. Also $\Gamma_p(\text{exp}) > \Gamma_{22}$ (Wigner).
3^-	This assignment gives $B_2/B_0 > 0.4$ for any choice of the parameters g_{23}/g_{21} and g_{13}/g_{21} (see table 2).
4^+	Equations 7, section A restrict the parameters g_{24}/g_{22} and g_{14}/g_{22} to absolute values less than 0.01. The theoretical prediction for the angular distribution coefficients is then $B_2/B_0 = 1.02$ and $B_4/B_0 = 0.55$ (see table 2).
$J \geq 5$	For $J \geq 5$, $\Gamma_p(\text{exp}) > \Gamma_{s\ell_o}$ (Wigner) where ℓ_o is the minimum value of orbital angular momentum by which J can be formed.

We are left with the possibilities $J^{\pi} = 1^-$ and $J^{\pi} = 2^+$. A 1^- assignment gives $B_2/B_0 = 0.09$ and $B_4/B_0 = 0$ if $\theta^2_{21} = 10\,\theta^2_{11}$. The assumption $\theta^2_{21} = \theta^2_{11}$ discussed in section A would eliminate a 1^- assignment, but we cannot expect this assumption to hold rigorously and a difference of a factor of 10 in θ^2_{21} and θ^2_{11} is not impossible. A 2^+ assignment gives $B_2/B_0 = 0.09$ and $B_4/B_0 = 0$ if $\theta^2_{20} = 2\,\theta^2_{22}$ and $\theta^2_{20} = \theta^2_{12}$. Our preference is for the 2^+ assignment, but a 1^- assignment is also possible on the basis of our data.

338 kev Resonance

The experimentally measured values of the angular distribution coefficients are $B_2/B_0 = 0.84 \pm 0.08$ and $B_4/B_0 = 0$.

J^{π}	Reason Eliminated
0^+	This assignment gives $B_2/B_0 = 0$.
1^-	With the restriction imposed on the parameters g_{23}/g_{21} and g_{13}/g_{21} by equations 7 section A, this assignment gives $-1 \leq B_2/B_0 \leq 0.4$.
2^+	Using equations 7 section A, we can show that at least one of the quantities g_{20}, g_{22}, and g_{12}, must be greater than g_{24} by a factor of 100 so our omission of terms involving g_{24} in the expressions given in table 2 is justified. We have $B_2/B_0 < 0.7$ for any choice of g_{22}/g_{20} and g_{12}/g_{20}.
4^+	We can use equations 7 section A to restrict the parameters g_{24}/g_{22} and g_{14}/g_{22} to absolute values less than 0.03. We then have $B_2/B_0 = 1.02$ and $B_4/B_0 = 0.55$.

$J \geq 5$ For $J \geq 5$, $\Gamma_p(\text{exp}) > \Gamma_{s\ell_o}(\text{Wigner})$.

The only possibility left is $J^\pi = 3^-$. If $\theta^2_{21} = \theta^2_{23} = \theta^2_{13}$, this assignment gives $B_2/B_0 = 0.81$, $B_4/B_0 = -0.02$ in good agreement with the experimental values. The 3^- assignment for this resonance is unique and does not depend on the assumption of the equality of the reduced widths, $\theta^2_{s\ell}$, for its uniqueness.

374 kev Resonance

For two independent angular distributions taken at this resonance, we obtain two sets of values for the angular distribution coefficients: $B_2/B_0 = 0.70 \pm 0.18$, $B_4/B_0 = 0.36 \pm 0.17$ (not shown), and $B_2/B_0 = 1.09 \pm 0.22$, $B_4/B_0 = 0.70 \pm 0.22$ (fig. 20). The uncertainties quoted are standard deviations, and the two sets of values are not in very good agreement. It cannot be said that they are statistically inconsistent, however, since the two values of B_2/B_0 and the two values of B_4/B_0 do not differ by more than the sum of their standard deviations. We therefore average the two sets of values and obtain $B_2/B_0 = 0.90 \pm 0.15$ and $B_4/B_0 = 0.59 \pm 0.15$.

Reason Eliminated

J^π	
0^+	This assignment gives $B_2/B_0 = 0$, $B_4/B_0 = 0$.
1^-	This assignment gives $B_4/B_0 = 0$.
2^+	The closest we can come to the experimental values with this assignment is $B_2/B_0 = 0.55$, $B_4/B_0 = 0.40$.
3^-	By a suitable choice of the parameters, the experimental value of B_2/B_0 can be matched with this

assignment but it is impossible to obtain a value greater than 0.27 for B_4/B_0.

5^- Use of equations 7 section A, justifies the omission of terms involving g_{25}, g_{27}, and g_{15}. The theoretical angular distribution is plotted in fig. 20, and clearly does not fit the experimental points.

$J \geq 6$ For $J \geq 6$, $\Gamma_p(\text{exp}) > \Gamma_{s\ell_o}(\text{Wigner})$.

We are left with the assignment $J^\pi = 4^+$. The 4^+ assignment, with $\theta^2_{22} = \theta^2_{24} = \theta^2_{14}$, gives $B_2/B_0 = 1.02$, $B_4/B_0 = 0.55$, $B_6/B_0 = 0$, $B_8/B_0 = 0$, in good agreement with the experimental values.

In the preceding discussion, we have not used the assumption of the equality of the reduced widths to obtain the 4^+ assignment. We have relied, however, on the uncertainties quoted for the average experimental values of B_2/B_0 and B_4/B_0 in order to eliminate the possibilities $J^\pi = 2^+$ and $J^\pi = 3^-$. Because of the poor agreement between the two sets of experimental values for the angular distribution coefficients, there is some question as to whether the uncertainties in the average values should not be larger than the ones quoted. Lest it appear that we have rejected the assignments $J^\pi = 2^+$ and $J^\pi = 3^-$ too hastily, we point out that if the assumption of the equality of the reduced widths holds even approximately, we must have $J \geq 4$ in order to get an appreciable $P_4(\cos\theta)$ term in the angular distribution. The assignments $J^\pi = 2^+$ and $J^\pi = 3^-$ give $B_4/B_0 < 0.10$ unless the reduced widths for different s and ℓ differ by more than a factor of 30.

V. CALCULATION OF REACTION RATES

A. Determination of Resonance Strengths $\omega\Gamma_p\Gamma_\alpha/\Gamma$

A brief derivation of the formulas needed in the calculation of reaction rates is given in appendix III. We wish to calculate the quantity P using equations 7, 13, and 14 of appendix III. P is called the reaction rate per pair of particles by Reeves and Salpeter[5], and for a specific reaction depends only on the temperature of the stellar gas in which the reaction takes place. For the calculation of P, we need to know the non-resonant cross section factor S and the values of the resonance strengths $\omega\Gamma_p\Gamma_\alpha/\Gamma$ for all resonances which can give significant contributions to P. In section III E we establish an upper limit of 100 Mev barns for S, and we now turn to the problem of obtaining the resonance strengths.

We will consider known resonances at 286, 338, 374, 445, 593, 797, and 815 kev. Resonances at higher energies do not give a significant contribution to P for temperatures in the range 5 to 10 x 10^8 ^oK, and we limit our calculations to this range of temperatures because this is the range in which carbon-burning takes place (see section I).

286, 338, 374, and 445 kev Resonances

Here we use the data from the present experiment. The resonance strengths are given by the equations:

$$Y = Y(90)\int \left[1 + \frac{A_2}{A_0}\cos^2\theta + \frac{A_4}{A_0}\cos^4\theta\right] d\Omega \qquad (1)$$

$$\frac{\omega\Gamma_p\Gamma_\alpha}{\Gamma} = \frac{Y\epsilon}{2\pi^2\lambda^2} \qquad (2)$$

Y is the total yield from the resonance, and the method for obtaining the stopping cross section ϵ is discussed in appendix II. For the 286, 338, and 374 kev resonances, Y(90) is listed in table 1 section III and the angular distribution coefficients A_2/A_0 and A_4/A_0 have been obtained in section IV. Since no angular distribution was taken at the 445 kev resonance, we assume the angular distribution is isotropic and write $Y = 4\pi Y(140)$ in place of equation 1 where Y(140) is listed in table 1, section III. This assumption will not introduce any error into our calculations of P, since the contribution of the 445 kev resonance to P is negligible in any case.

The values of Y and $\omega\Gamma_p\Gamma_\alpha/\Gamma$ are listed in table 3. The uncertainties quoted for Y include the uncertainty in the angular distribution coefficients, and the uncertainties quoted for $\omega\Gamma_p\Gamma_\alpha/\Gamma$ include the uncertainty of $\pm$ 15% in the stopping cross section ϵ.

593 kev Resonance

We have available the data of Flack et al.[1] and Bauman et al.[2] and will use both sets of data. The first problem is to determine the angular distribution coefficients. Although no angular distribution data are available on this resonance in the $Na^{23}(p, \alpha)Ne^{20}$ reaction, the angular distribution coefficients can be inferred from the alpha scattering data of Goldberg et al.[14] and the proton scattering data of Bauman et al. Goldberg et al. have established $J^\pi = 3^-$ for the compound Mg^{24} state, and Bauman et al. report that the formation of this state from $Na^{23} + p$ proceeds almost exclusively through the combination $s = 2$, $\ell = 1$. Referring to table 2, we have $g_{13}/g_{21} = 0$ and $g_{23}/g_{21} = 0$ so the angular

Table 3

Resonance Contributions to Total Reaction Rate P

For Different Temperatures

Resonance Energy in kev	$Y/10^{10}$	$\frac{\omega\Gamma_p\Gamma_a}{\Gamma}$ in Mev
286	0.224 ± 0.016	$(4.60 \pm 0.7) \times 10^{-8}$
338	0.374 ± 0.027	$(8.40 \pm 1.3) \times 10^{-8}$
374	0.021 ± 0.005	$(4.9 \pm 1.3) \times 10^{-9}$
445	0.028 ± 0.006	$(6.9 \pm 1.7) \times 10^{-9}$
593		$(4.7 \pm 0.8) \times 10^{-5}$
797		$(2.0 \pm 0.5) \times 10^{-4}$
815		$(6.0 \pm 1.5) \times 10^{-5}$
Possible unobserved resonances in region 120 - 450 kev		$< (6 \times 10^{-10})$

Resonance Energy in kev	P_R			
	5×10^8 °K	6×10^8 °K	8×10^8 °K	10×10^8 °K
286	$(64\pm10)\times10^{-24}$	$(14\pm2)\times10^{-23}$	$(3\pm0.5)\times10^{-22}$	--
338	$(36\pm6)\times10^{-24}$	$(9\pm2)\times10^{-23}$	$(3\pm0.5)\times10^{-22}$	--
374	--	--	--	--
445	--	--	--	--
593	$(68\pm12)\times10^{-24}$	$(48\pm8)\times10^{-23}$	$(51\pm9)\times10^{-22}$	$(18\pm3)\times10^{-21}$
797	$(2\pm0.5)\times10^{-24}$	$(3\pm0.7)\times10^{-23}$	$(10\pm2.5)\times10^{-22}$	$(6.5\pm1.8)\times10^{-21}$
815	--	--	$(3\pm0.7)\times10^{-22}$	$(2\pm0.5)\times10^{-21}$

Table 4

Total Reaction Rate P for Different Temperatures

	5×10^8 °K	6×10^8 °K	8×10^8 °K	10×10^8 °K
Possible Unobserved Resonances 120-450 kev P_R	$< 30 \times 10^{-24}$	$< 4 \times 10^{-23}$	--	--
Non-resonant $P_{N.R.}$	$< 18 \times 10^{-24}$	$< 7 \times 10^{-23}$	$< 7 \times 10^{-22}$	$< 3 \times 10^{-21}$
$P = \sum_R P_R$	$170^{+42}_{-24} \times 10^{-24}$	$74^{+12}_{-9} \times 10^{-23}$	$70^{+11}_{-9} \times 10^{-22}$	$26^{+5}_{-3.5} \times 10^{-21}$
$\text{Log}_{10} P$	-21.77	-21.13	-20.16	-19.58
$\text{Log}_{10} P$ (Reeves and Salpeter)	-21.9	-21.1	-20.1	-19.6

distribution coefficients are $B_2/B_0 = 0.80$, $B_4/B_0 = 0$ or $A_2/A_0 = 2$, $A_4/A_0 = 0$.

Flack et al. report a yield measurement at 90 degrees with an uncertainty of ± 20%. Using their value and equations 1 and 2 we obtain $\omega\Gamma_p\Gamma_\alpha/\Gamma = (4.15 \pm 1) \times 10^{-5}$ Mev. The uncertainty quoted includes the additional uncertainty of ± 15% in our value for ϵ. Bauman et al. give a differential cross section curve for the reaction $Na^{23}(p, \alpha)Ne^{20}$ taken at 157.5 degrees. From this curve and the known form of the angular distribution, we can determine $\frac{d\sigma_R}{d\Omega}(90)$, the differential cross section at 90 degrees at the resonance energy. The appropriate equations for determining $\omega\Gamma_p\Gamma_\alpha/\Gamma$ are then

$$\sigma_R = \frac{d\sigma_R}{d\Omega}(90) \int \left[1 + \frac{A_2}{A_0}\cos^2\theta + \frac{A_4}{A_0}\cos^4\theta\right] d\Omega \qquad (3)$$

$$\frac{\omega\Gamma_p\Gamma_\alpha}{\Gamma} = \frac{\Gamma\sigma_R}{4\pi\lambda^2} \qquad (4)$$

The value of $\omega\Gamma_p\Gamma_\alpha/\Gamma$ obtained using Bauman's cross section curve is 5.2×10^{-5} Mev. Since Bauman quotes no uncertainty for his curve, we have arbitrarily assigned an uncertainty of 25% to give the value of $\omega\Gamma_p\Gamma_\alpha/\Gamma$ obtained from his data equal weight with the value obtained from Flack's data. Averaging the two values gives $(4.7 \pm 0.8) \times 10^{-5}$ Mev which is the value we will use.

797 and 815 kev Resonances

For these resonances, we must rely on Bauman's data alone. From his elastic proton scattering data, Bauman obtains $J^{\pi} = 1^{-}$ for the 797 kev resonance with equal participation by $s = 1$, $\ell = 1$ and $s = 2$, $\ell = 1$ in the formation of the compound nucleus. This implies $(g_{11}/g_{21})^2 = 1$, $g_{23}/g_{21} = 0$ and from table 2 the angular distribution coefficients are $B_2/B_0 = -0.4$, $B_4/B_0 = 0$ or $A_2/A_0 = -0.5$, $A_4/A_0 = 0$. For the 815 kev resonance, Bauman gives $J^{\pi} = 2^{+}$ with the compound nucleus formed mainly by the combination $s = 2$, $\ell = 0$. The angular distribution at this resonance is therefore isotropic.

Having determined the angular distribution coefficients for these resonances, we can use Bauman's cross section curve and equations 3 and 4 to obtain the resonance strengths. These are listed in table 3, and we have again assigned an uncertainty of ± 25%.

B. Uncertainty Limits for Reaction Rates

Table 3 lists the values of P_R calculated from the resonance strengths obtained in the previous section using equation 7 of appendix III. The upper limit on P_{NR} based on the upper limit of 100 Mev barns for S is also given in the table. We have obtained the values of the total reaction rate P listed in table 4 by summing the contributions of all the resonances in table 3. A non-resonant contribution is not included in the sum, because we have not determined the actual value of the non-resonant contribution but only an upper limit for its value.

The lower uncertainty, U_L, quoted for P is just the square root

of the sum of the squares of the uncertainties in the values of P_R. In determining the upper uncertainty, U_U, we must allow for the possibility that P can be increased by a non-resonant contribution and by contributions from unobserved resonances.

The magnitude of P_R for a resonance occurring at some energy E_R is controlled by the product $(\omega\Gamma_p\Gamma_\alpha/\Gamma) \exp(-E_R/kT)$. In table 1 of section III we have listed the experimental upper limit on Y(90) for any unobserved resonance in the region 120 to 450 kev. From this we obtain $(\omega\Gamma_p\Gamma_\alpha/\Gamma) < 6 \times 10^{-10}$ Mev, for any unobserved resonance above 120 kev, assuming the angular distribution from any such resonance to be isotropic. Since $\exp(-E_R/kT)$ is a sharply decreasing function of E_R, an unobserved resonance having $\omega\Gamma_p\Gamma_\alpha/\Gamma$ equal to the experimental limit of 6×10^{-10} Mev will have the maximum possible value of P_R if it occurs at 120 kev. Otherwise, the value of P_R will be much less, even though $\omega\Gamma_p\Gamma_\alpha/\Gamma$ is equal to the experimental limit. Below 120 kev we have no experimental data to establish an upper limit for $\omega\Gamma_p\Gamma_\alpha/\Gamma$, but we can assume that $(\omega\Gamma_p\Gamma_\alpha/\Gamma) < \omega\Gamma_p < \frac{5}{8}\Gamma_{s\ell_o}$ (Wigner) where $\Gamma_{s\ell_o}$(Wigner) is the Wigner limit for protons of zero orbital angular momentum. The factor 5/8 comes from the fact protons with zero orbital angular momentum must form the compound state $J^\pi = 2^+$ in which case $\omega = 5/8$. At 120 kev, $\frac{5}{8}\Gamma_{s\ell_o}$(Wigner) $\approx 6 \times 10^{-10}$ Mev, i.e. the limit on $\omega\Gamma_p\Gamma_\alpha/\Gamma$ imposed by the Wigner limit for Γ_p is equal to the limit imposed by our experimental sensitivity. Since $\Gamma_{s\ell_o}$(Wigner) depends on the proton barrier factor, it decreases sharply with decreasing energy and for temperatures in the range we are considering the product

$\Gamma_{s\ell_o}$(Wigner) exp $(-E_R/kT)$ also decreases sharply with decreasing energy below 120 kev. Therefore the value of P_R for any resonance occurring below 120 kev will also be much less than the value of P_R for a resonance occurring at 120 kev and having $\omega\Gamma_p\Gamma_a/\Gamma = 6 \times 10^{-10}$ Mev.

Let us assume that there exists a resonance at 120 kev which we failed to observe and which has $\omega\Gamma_p\Gamma_a/\Gamma = 6 \times 10^{-10}$ Mev. We designate the value of P_R for such a resonance by $P_R(\max)$. The above considerations have shown that if other resonances exist which we failed to observe, P_R for these resonances will be much less than $P_R(\max)$. We also assume that the non-resonant contribution has its maximum value $P_{NR}(\max)$, corresponding to $S = 100$ Mev barns. As a reasonable prescription for the upper uncertainty U_U in P we take $U_U^2 = U_L^2 + (P_R(\max) + P_{NR}(\max))^2$. We note that we have considered only the possibility of an unobserved resonance below 450 kev, in the preceding discussion, but this is sufficient since the region above 450 kev has been covered by Flack et al. and Bauman et al. with sufficient experimental sensitivity to establish that there are no unknown resonances above 450 kev which can give a significant contribution to P.

VI. DISCUSSION OF RESULTS

In this section, we give a brief discussion of the significance of our results in the light of the work of other investigators. We will discuss sections III, IV, and V, in order.

The only excitation function data available for comparison is the data of Flack et al.[1] Our values of $(1.70 \pm 0.1) \times 10^{-12}$ and $(1.77 \pm 0.1) \times 10^{-12}$ for Y(90) at the 286 and 338 kev resonances are in agreement with Flack's values of $(1.6 \pm 0.3) \times 10^{-12}$ and $(1.45 \pm 0.3) \times 10^{-12}$. Our values of 285.9 ± 0.5 kev and 338.6 ± 0.6 kev for the resonance energies also agree with his values of 287 ± 1.5 kev and 338 ± 1.5 kev. Flack does not report widths for these resonances, and failed to observe the 374 and 445 kev resonances due to their low yield. Our failure to observe the 307.8 kev resonance reported by Hancock and Verdaguer[12] in the $Na^{23}(p,\gamma)Mg^{24}$ reaction lends support to their assignment of $J^{\pi} = 2^{-}$ for this resonance. Hancock and Verdaguer, Wagner and Heitzman[13], and others report a resonance at 374 kev in the $Na^{23}(p,\gamma)Mg^{24}$ reaction, and Hancock and Verdaguer also report a resonance at 445 kev in this reaction although Wagner and Heitzman do not. The fact that gamma decay can compete with alpha decay at the 374 kev resonance is interesting, and tends to support our assignment $J^{\pi} = 4^{+}$ for this resonance since the alpha decay will be inhibited by the fact that the alpha particles must carry away 4 units of angular momentum. The situation at the 445 kev resonance is also interesting. The alpha yield from this resonance is about the same as the yield from the 374 kev resonance, both being a factor of 10 smaller

than the yields from the 286 and 338 kev resonances. We think it probable that the situation at the 445 kev resonance is analogous to the situation at the 374 kev resonance where the compound Mg^{24} state has a large value of J inhibiting alpha decay and permitting gamma decay to compete. We think, therefore, that Hancock and Verdaguer are probably correct in reporting the 445 kev resonance in the $Na^{23}(p,\gamma)Mg^{24}$ reaction, but the question can only be settled by a more careful study of this reaction.

The only previous spin and parity assignments for Mg^{24} states in the energy region we have covered come from the alpha scattering data of Goldberg.[14] Goldberg gives a 2^+ assignment to a Mg^{24} state at 11.960 Mev excitation energy. The excitation energy for the 286 kev resonance is 11.960 Mev, so the two states must be identical and our assignment $J^\pi = 2^+ (1^-)$ is in agreement with Goldberg's. (The parentheses indicate that the 1^- assignment is not definitely eliminated on the basis of our data, but the 2^+ assignment is the preferred one.) Goldberg fails to observe the Mg^{24} states corresponding to the 338, 374, and 445 kev resonances, probably due to the fact that these states are too narrow to be seen with his instrumental resolution of 2 kev.

In table 4 section V our values for P are compared with those used by Reeves and Salpeter in their analysis of a carbon-burning star. The fact that the two sets of values are almost identical is due to our failure to discover any new resonances which contribute significantly to P (the contributions of the 374 and 445 kev resonances are negligible). We have, however, considerably reduced the uncertainty in the values

of P by the careful study of the energy region below 270 kev. This uncertainty was previously as large as a factor of 20. The conclusions of Reeves and Salpeter which depend on the $Na^{23}(p, \alpha)Ne^{20}$ reaction rate are thus on much firmer ground than before.

APPENDIX I

Fitting of Thick Target Excitation Functions

In the following discussion we will deal specifically with the reaction $Na^{23}(p, \alpha)Ne^{20}$ so that we can keep most of the notation used in section III of the thesis. The results can easily be made more general.

The reaction yield from a thick target as a function of proton bombarding energy is given by:

$$Y(E) = \int_0^E \frac{\sigma(E')}{\epsilon(E')}\, dE' \qquad (1)$$

$Y(E)$ is the yield of alpha particles per incident proton and $\epsilon(E')$ is the stopping cross section of the target (NaCl). In a region where the cross section $\sigma(E')$ is dominated by a single isolated resonance, $\sigma(E')$ is given by the Breit-Wigner single level formula:

$$\sigma(E') = \pi\lambda^2\omega \frac{\Gamma_p\Gamma_\alpha}{(E'-E_R)^2+\frac{\Gamma^2}{4}} \qquad (2)$$

The quantities λ, Γ_p, Γ_α and Γ are themselves functions of the energy, but we assume that the resonance is narrow enough that these quantities, as well as ϵ, can be treated as constants. We have neglected the level shift parameter in equation 2 since in the case of a narrow resonance the inclusion of this parameter serves only to re-define the resonance width, Γ. We define the total yield, Y, from the resonance by:

$$Y = Y(E = \infty) = 2\pi^2\lambda^2\omega \frac{\Gamma_p\Gamma_\alpha}{\Gamma} \qquad (3)$$

and write equation 1 in the form:

$$Y(E) = \frac{Y}{\pi}\left[\tan^{-1}\frac{2(E - E_R)}{\Gamma} + \frac{\pi}{2}\right] \qquad (4)$$

We suppose that we have a set of experimental numbers $Y(E)$ which we want to fit by a least squares procedure in order to obtain the best values for the resonance parameters Y, Γ, and E_R. The discussion holds equally well if the normalized quantities $Y(E)$ and Y are replaced by the unnormalized quantities $N_R(E)$ and $N_R(\infty)$ defined in section III C. In practice, the fit was made to the unnormalized experimental numbers and the normalization carried out at the end.

We can obtain estimates of Y, Γ, and E_R, by drawing a smooth curve through the points of our excitation function. We estimate Y from the height of the step, E_R from the half-maximum point, and Γ from the difference in energy between the 3/4 and 1/4 maximum points, and call these estimates $\overline{Y}$, $\overline{E}_R$, and $\overline{\Gamma}$. We now let $Y = \overline{Y} + \Delta Y$, $E_R = \overline{E}_R + \Delta E_R$, and $\Gamma = \overline{\Gamma} + \Delta\Gamma$, and expand equation 4 to first order in ΔY, ΔE_R, and $\Delta\Gamma$:

$$Y(E) \approx \frac{\overline{Y}}{\pi}\left[\tan^{-1}\frac{2(E-\overline{E}_R)}{\overline{\Gamma}} + \frac{\pi}{2}\right] + \frac{\Delta Y}{\pi}\left[\tan^{-1}\frac{2(E-\overline{E}_R)}{\overline{\Gamma}} + \frac{\pi}{2}\right]$$

$$+ \frac{\overline{Y}}{\pi}\left[\frac{-\overline{\Gamma}/2}{(E-\overline{E}_R)^2 + \frac{\overline{\Gamma}^2}{4}}\right]\Delta E_R + \frac{\overline{Y}}{\pi}\left[\frac{-(E-\overline{E}_R)/2}{(E-\overline{E}_R)^2 + \frac{\overline{\Gamma}^2}{4}}\right]\Delta\Gamma \qquad (5)$$

Expression 5 can be fitted by least squares[20] to obtain the best values for ΔY, ΔE_R, and $\Delta\Gamma$. Equation 5 will be a good approximation to equation 4 if $\Delta Y/\overline{Y}$, $\Delta E_R/\overline{\Gamma}$, and $\Delta\Gamma/\overline{\Gamma}$, are all much less than 1, i. e. if our original estimates are good.

APPENDIX II

Stopping Cross Section for Sodium Chloride

The atomic stopping cross section per molecule of sodium chloride, ϵ_{NaCl}, is equal to the sum of the atomic stopping cross sections for sodium and chlorine, ϵ_{Na} and ϵ_{Cl}. No experimental data on ϵ_{Na} and ϵ_{Cl} are available, nor is there a satisfactory theory available for calculating ϵ_{Na} and ϵ_{Cl} accurately at the low energies (less than 600 kev) in which we are interested. We have therefore used the experimental data on the stopping cross sections of neon, aluminum, and argon,[19] and obtained ϵ_{Na} and ϵ_{Cl} by the following interpolation procedure:

$$\epsilon_{Na} = \epsilon_{Ne} + (\epsilon_{Al} - \epsilon_{Ne}) \frac{Z_{Na} - Z_{Ne}}{Z_{Al} - Z_{Ne}}$$

$$\epsilon_{Cl} = \epsilon_{Al} + (\epsilon_{A} - \epsilon_{Al}) \frac{Z_{Cl} - Z_{Al}}{Z_{A} - Z_{Al}} \qquad (1)$$

This interpolation is suggested by the fact that, if one neglects a term involving log Z in the theoretical expression for the stopping cross section, the expression is proportional to Z. It should be noted that interpolation is of doubtful validity. In the proton velocity region of this experiment, ϵ depends primarily on the binding of the valence electrons and may be expected to show shell structure.

Curves of ϵ_{Na} and ϵ_{Cl} obtained using equation 1 are shown in fig. 21. As a check on the method of interpolation, ϵ_{Al} was calculated by interpolation between argon and neon and the results agreed with the experimental values to within 10% over the proton energy range from

200 to 700 kev. We have therefore assigned an uncertainty of $\pm 10\%$ to the curves for ϵ_{Na} and ϵ_{Cl} in fig. 21, which implies a 15% uncertainty in ϵ_{NaCl}.

APPENDIX III

Derivation of Formulas for Reaction Rates

We give here the derivation of the expressions for the reaction rate of a nuclear reaction taking place in a stellar gas at temperature T. We designate the two initial particles by the subscripts 1 and 2 and let N_1 and N_2 be the number of particles of each type per unit volume. The number of reactions taking place per unit volume per unit time where the relative velocity of the two particles lies in the range v to v + dv is:

$$dN = 4\pi N_1 N_2 \left(\frac{m}{2\pi kT}\right)^{3/2} \exp\left(-\frac{mv^2}{2kT}\right) v^2 dv\, \sigma(v)\, v \qquad (1)$$

where m is the reduced mass, k is Boltzman's constant, and $\sigma(v)$ is the cross section for the reaction. When written in terms of E, the center of mass energy, equation 1 becomes:

$$dN = \frac{4N_1N_2}{(2\pi)^{1/2} m^{1/2} (kT)^{3/2}}\, \sigma(E) E e^{-E/kT} dE \qquad (2)$$

The total number of reactions taking place per unit volume per unit time is obtained by integrating expression 2 over all energies:

$$N = \frac{4N_1N_2}{(2\pi)^{1/2} m^{1/2} (kT)^{3/2}} \int_0^\infty \sigma(E) E e^{-E/kT} dE \qquad (3)$$

In a region dominated by a single resonance, the appropriate form for $\sigma(E)$ is the Breit-Wigner single-level formula:

$$\sigma(E) = \pi \lambda^2 \omega \frac{\Gamma_{in}\Gamma_{out}}{(E-E_R)^2 + \frac{\Gamma^2}{4}} \qquad (4)$$

Here $\omega = (2j+1)/(2j_1+1)(2j_2+1)$ where j_1 and j_2 are the spins of particles 1 and 2 and j is the spin of the compound nucleus; other quantities have their usual significance. With this form for $\sigma(E)$, the integral in 3 cannot be evaluated in terms of elementary functions, but the following approximation can be made in order to obtain a simple expression for N. It is assumed that the quantity $Ee^{-E/kT}$ does not vary much over the resonance, as will be the case if the resonance is sufficiently narrow, and expression 4 is approximated by a δ-function having the same area:

$$\sigma(E) = 2\pi^2\lambda\!\!\!^{-2}\omega \frac{\Gamma_{in}\Gamma_{out}}{\Gamma} \delta(E - E_R) \qquad (5)$$

With this approximation, equation 3 gives:

$$N_R = \frac{(2\pi)^{3/2}\hbar^2 N_1 N_2}{m^{3/2}(kT)^{3/2}} \omega \frac{\Gamma_{in}\Gamma_{out}}{\Gamma} e^{-E_R/kT} \qquad (6)$$

The quantity $(\omega\Gamma_{in}\Gamma_{out})/\Gamma$ is often called the resonance strength, and is determined experimentally. We have attached the subscript R to N in expression 6 to indicate that we are talking about the contribution of a single resonance to the reaction rate. Reeves and Salpeter give equation 6 in a different form in terms of a quantity $P_R = N_R/N_1N_2$. Their expression, which can be obtained from equation 6 by inserting numerical values for $\hbar$, k and π, is:

$$\log P_R = -11.09 - \frac{3}{2}\log m - \frac{3}{2}\log T + \log \frac{\omega\Gamma_{in}\Gamma_{out}}{\Gamma} - 50.4\, E_R/T \qquad (7)$$

In expression 7, m is in a. m. u., T in units of 10^8 °K, and energies are in Mev.

When the cross section is non-resonant, it is convenient to write $\sigma(E)$ in the form:

$$\sigma(E) = \frac{S}{E} e^{-2\pi\eta} \tag{8}$$

η is the coulomb parameter $Z_1 Z_2 e^2/\hbar v$ and S is almost energy-independent. Inserting this expression for $\sigma(E)$ into 3 gives:

$$N_{N.R.} = \frac{4N_1N_2S}{(2\pi)^{1/2}m^{1/2}(kT)^{3/2}} \int_0^\infty \exp\left[-\frac{E}{kT} - \frac{2\pi Z_1 Z_2 e^2 m^{1/2}}{\hbar(2E)^{1/2}} \right] dE \tag{9}$$

In equation 9, the subscript N. R. is attached to N to indicate that we are talking about the contribution of the non-resonant cross section to the reaction rate. The integral in 9 cannot be evaluated in terms of elementary functions, and the following approximation is used to obtain a simple expression for $N_{N.R.}$. The quantity $(-E/kT) - \frac{2\pi Z_1 Z_2 e^2 m^{1/2}}{\hbar(2E)^{1/2}}$ has a maximum value $-\tau$ at the point E_0 where:

$$E_0 = \left[\frac{\pi Z_1 Z_2 e^2 kT m^{1/2}}{2^{1/2}\hbar} \right]^{2/3}$$

$$\tau = 3\left[\frac{\pi Z_1 Z_2 e^2 m^{1/2}}{(2kT)^{1/2}\hbar} \right]^{2/3} \tag{10}$$

We expand this quantity about E_0 retaining only terms up to $(E-E_0)^2$ and this reduces the integrand in equation 9 to a gaussian:

$$\int_0^\infty \exp\left[-\frac{E}{kT} - \frac{2\pi Z_1 Z_2 e^2 m^{1/2}}{\hbar(2E)^{1/2}} \right] dE \approx e^{-\tau} \int_0^\infty \exp\left[-\frac{(E-E_0)^2}{4E_0^2/\tau} \right] dE \tag{11}$$

Expression 9 for $N_{N.R.}$ becomes:

$$N_{N.R.} = \frac{4N_1N_2S}{(2\pi)^{1/2}m^{1/2}(kT)^{3/2}} e^{-\tau} \left[\frac{4\pi E_0^2}{\tau} \right]^{1/2} \tag{12}$$

Reeves and Salpeter give equation 12 in terms of $P_{N.R.} = N_{N.R.}/N_1N_2$ with the numerical constants inserted. Their expression is:

$$\log P_{N.R.} = -15.15 - \log Z_1Z_2m + \log S + 2\log\tau - 0.434\tau \tag{13}$$

where S is in Mev barns and m is in a.m.u. The total reaction rate is obtained by summing the non-resonant contribution and the contributions of all resonances:

$$N = N_{N.R.} + \sum_R N_R$$
$$P = P_{N.R.} + \sum_R P_R \tag{14}$$

REFERENCES

(1) F. C. Flack, J. G. Rutherglen, and P. J. Grant, Proc. Phys. Soc. (London) 67A, 974 (1954).

(2) N. P. Baumann and F. Prosser, Phys. Rev. 104, 376 (1956).

(3) P. H. Stelson and W. M. Preston, Phys. Rev. 95, 974 (1954).

(4) P. H. Stelson, Phys. Rev. 96, 1584 (1954).

(5) H. Reeves and E. E. Salpeter, Phys. Rev. 116, 1505 (1959).

(6) A. G. W. Cameron, Astrophysical Journal 130, 429 (1959).

(7) P. M. Endt and C. M. Braams, Revs. Mod. Phys. 29, 683 (1957).

(8) W. A. Wenzel, Ph. D. Thesis, California Institute of Technology, (1952).

(9) F. Ajzenberg-Selove and T. Lauritsen, Nucl. Phys. 11, 1 (1959).

(10) O. Beckman, T. Huus, and C. Zupancic, Phys. Rev. 91, 607 (1953).

(11) G. Dearnaley, G. A. Dissanaike, A. P. French, and G. L. Jones, Phys. Rev. 108, 743 (1957).

(12) D. A. Hancock and F. Verdauguer, Proc. Phys. Soc. (London) 68A, 1080 (1955).

(13) S. Wagner and M. Heitzmann, Zeit fur Naturforschung 15A, 74 (1960).

(14) E. Goldberg, W. Haberli, A. I. Galonsky, and R. A. Douglas, Phys. Rev. 93, 799 (1954).

(15) J. M. Blatt and L. C. Biedenharn, Revs. Mod. Phys. 24, 258 (1952).

(16) W. T. Sharp, J. M. Kennedy, B. J. Sears, and M. G. Hoyle, Tables of Coefficients for Angular Distribution Analysis, Chalk River, Ontario (1954).

(17) Nuclear Spectroscopy, Part A, edited by F. Ajzenberg Selove, Academic Press, (1960), p. 126.

(18) M. E. Rose, Phys. Rev. 91, 610 (1953).

(19) W. Whaling, Hand. der Physik 34, 193 (1958).

(20) Treatment of Experimental Data, A. G. Worthing and Joseph Geffner, Wiley and Sons, New York, (1943)

Figure 1. This figure shows a vertical cross section view of the target chamber. The cross section is in a plane perpendicular to the beam direction, and the axis of the target rod lies in this plane. The alpha counter is shown at 90 degrees. The number code has the following interpretation: (1) 1/2" stainless steel target rod, (2) 3" diameter lucite plug, (3) target chamber wall (the target chamber was made by boring a 2-1/2" diameter hole in a 3" square piece of brass), (4) cold trap (copper), (5) thin piece of stainless steel to serve as an insulator between cold trap and rest of target chamber, (6) target backing (copper or silver), (7) stupakoff insulator, (8) gold foil window in front of alpha counter, (9) solid state alpha particle counter, (10) supporting frame for foil window (20 mil tantalum), (11) shield for top and back of counter (brass), (12) brass plug supporting cold trap and alpha counter (plug can be rotated on its O-ring seal to change the counter angle), (13) O-ring grooves, (14) wire leading from counter to pre-amp, (15) hollow brass tube supporting counter assembly, (16) an enlargement of this section is shown in fig. 2. Fig. 1 is drawn approximately to scale. (See page 4.)

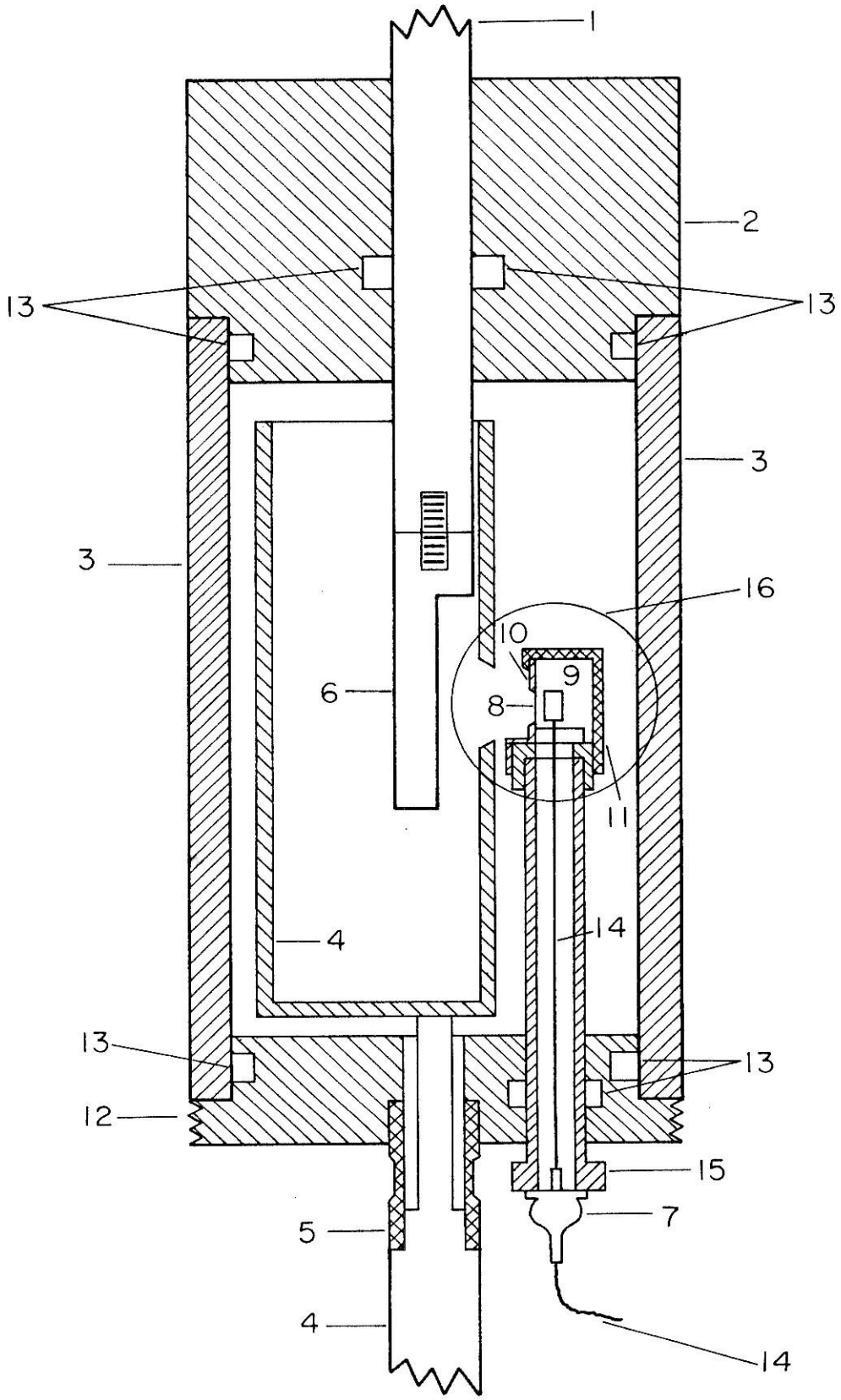
1
2
13
13
3
3
16
10
9
8
6
11
4
14
13
13
12
15
7
5
4
14

Figure 2. The top portion of this figure shows a horizontal cross section of the target chamber. The plane of the cross section is perpendicular to the target rod axis, and the proton beam lies in this plane. The angles indicate the manner in which the target and counter were positioned in taking an angular distribution. The bottom portion of the figure shows an enlargement of the counter assembly and the dimensions of the foil window. The number code has the following interpretation: (1) target chamber wall, (2) quartz window for viewing beam, (3) brass piece supporting target chamber, (4) suppressor ring (brass), (5) cold trap, (6) target backing, (7) support for foil window, (8) frame of counter holder (aluminum), (9) counter, (10) arrow indicates beam direction, (11) proton beam (the beam cross section in a plane perpendicular to the plane of the paper is 1/8" square), (12) shield for top and back of counter, (13) counter base, (14) tube supporting counter assembly, (15) wire leading to pre amp (this wire also supports the counter itself), (16) foil window. The top portion of fig. 2 is drawn approximately to scale. (See pages 4, 7, 13, and 35.)

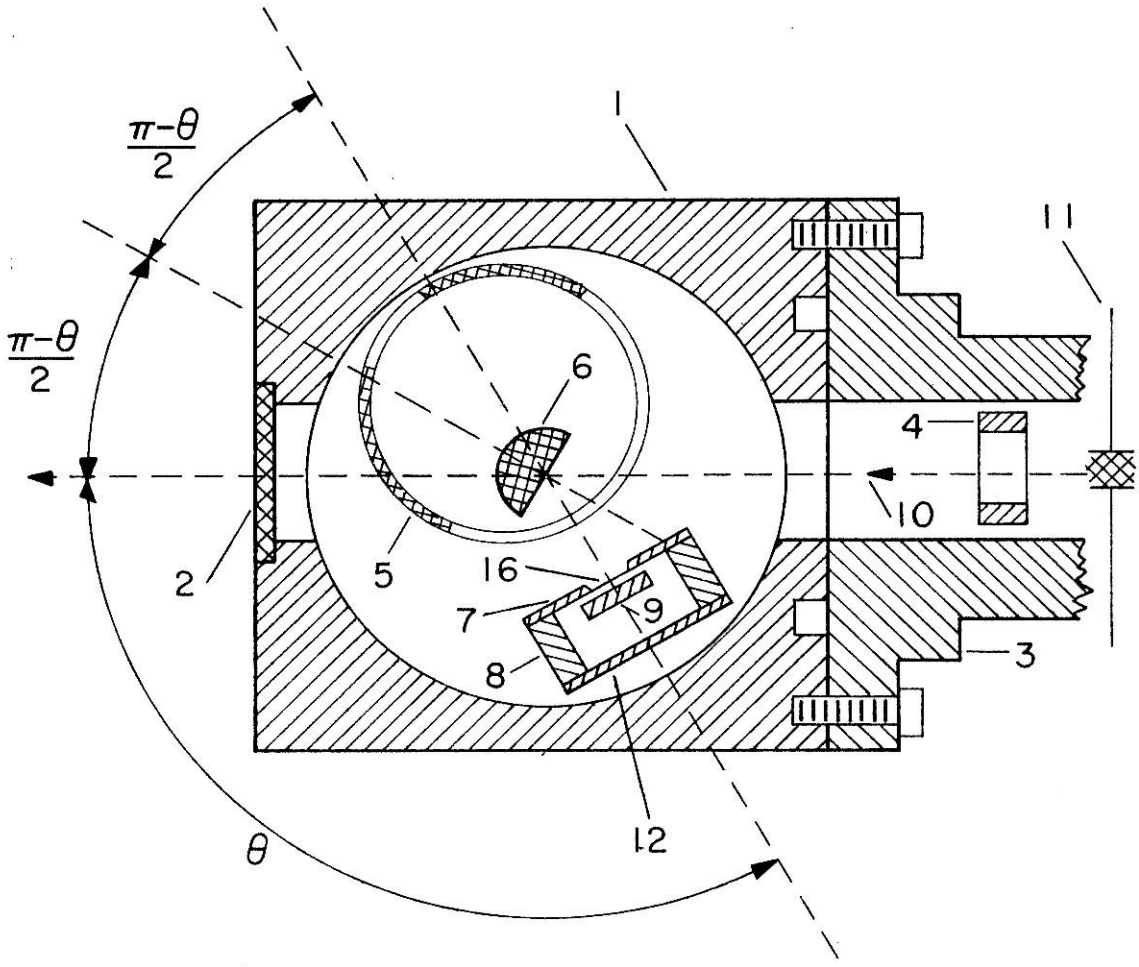

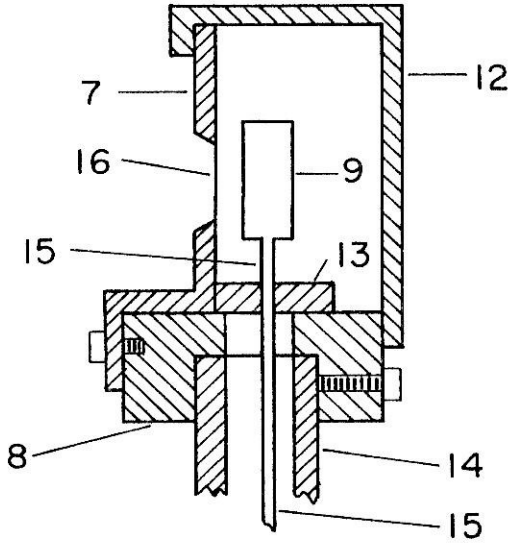

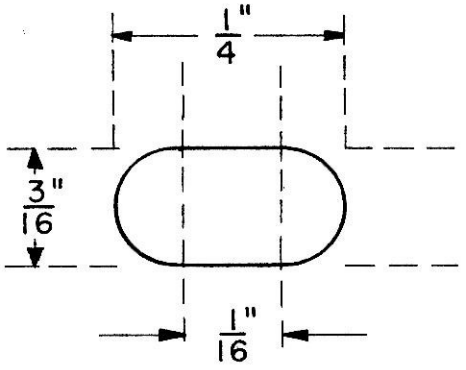

DIMENSIONS
OF FOIL WINDOW

Figure 3. This figure shows the number of counts per fixed amount of charge from the $Na^{23}(p, \alpha)Ne^{20}$ reaction as a function of the amount of charge already deposited on the target spot. The top part of the figure was taken with a pure sodium target; the bottom part was taken with a sodium chloride target. In both cases the proton energy was held constant slightly above the 286 kev resonance. A decrease in counts as more charge is deposited is apparent in the case of the pure sodium target but not in the case of the sodium chloride target. (See page 5.)

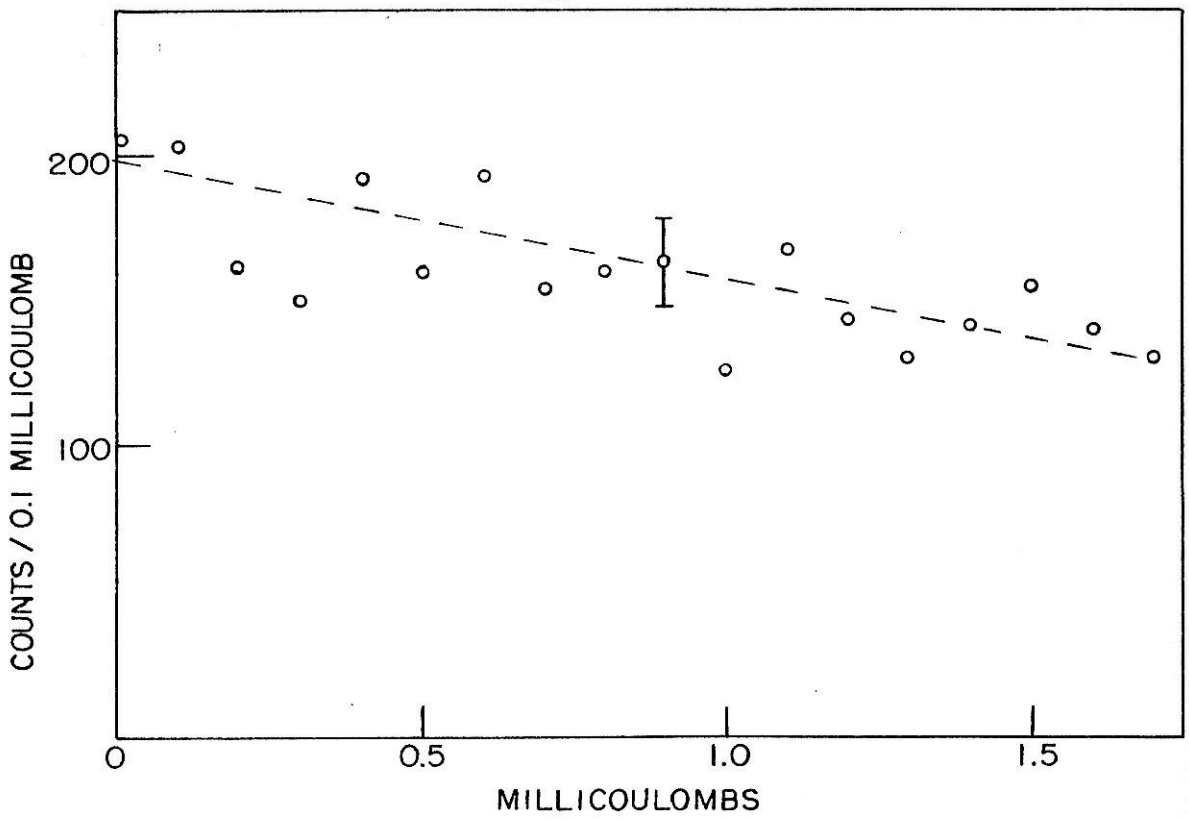
200
100
COUNTS / 0.1 MILLICOULOMB
0
0.5
1.0
1.5
MILLICOULOMBS

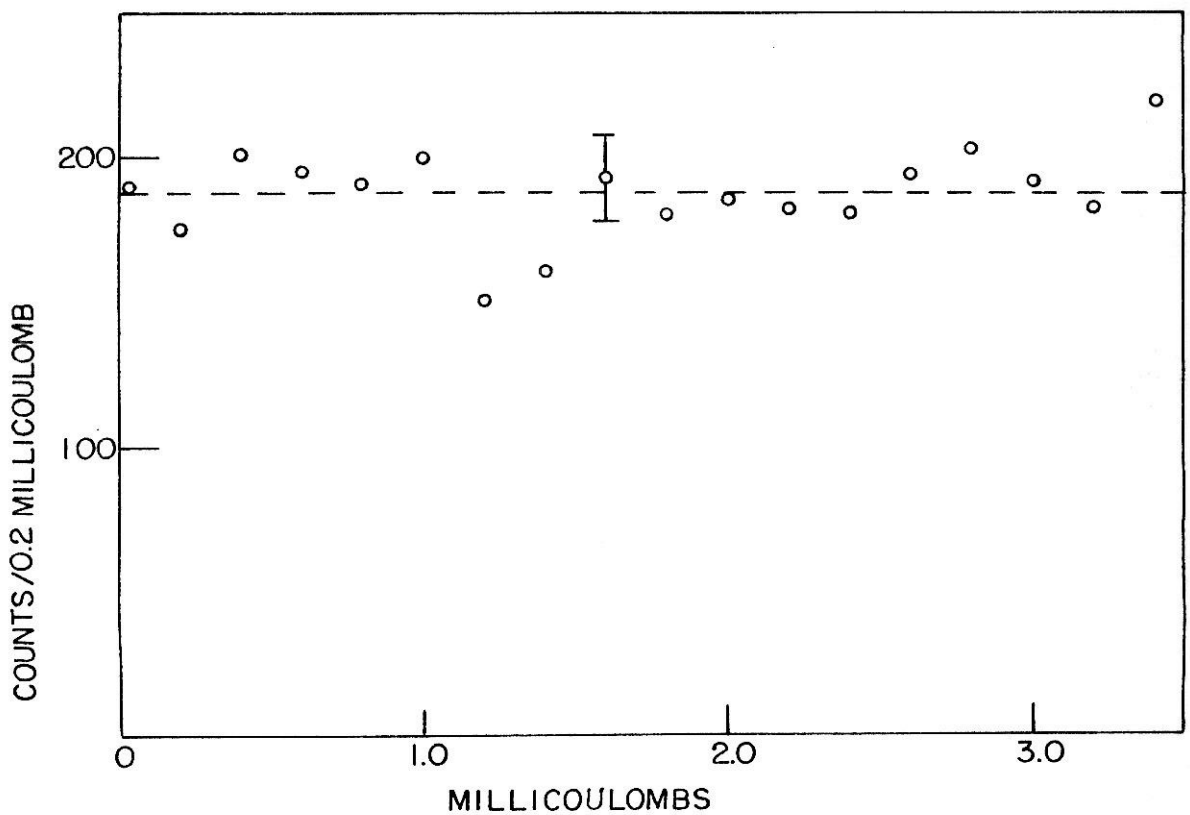
200
100
COUNTS/0.2 MILLICOULOMB
0
1.0
2.0
3.0
MILLICOULOMBS

Figure 4. This figure shows a comparison between two excitation functions taken at the 286 kev resonance in the $Na^{23}(p, \alpha)Ne^{20}$ reaction. The top one was taken with a pure sodium target; the bottom one was taken with a sodium chloride target. The trailing edge of the excitation function is much sharper in the case of the sodium chloride target, and the approximate target thickness is indicated. (See page 5.)

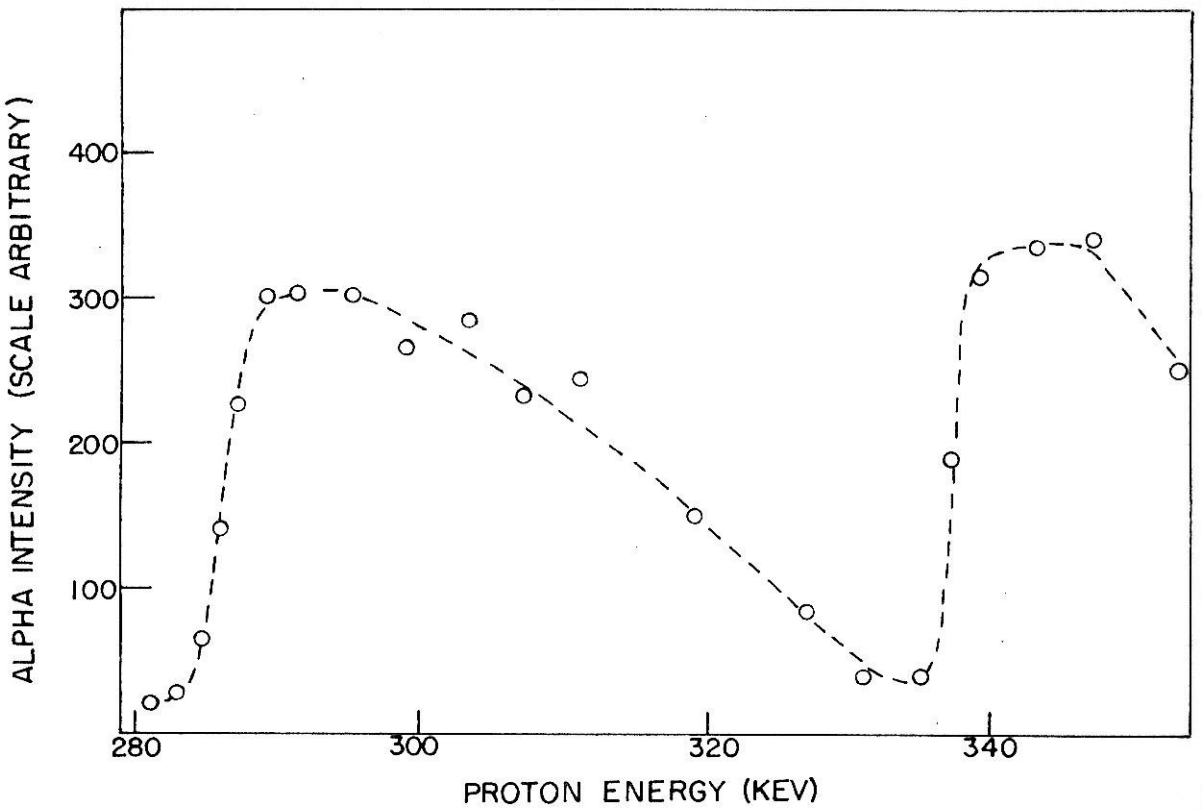
ALPHA INTENSITY (SCALE ARBITRARY)
400
300
200
100
280
300
320
340
PROTON ENERGY (KEV)

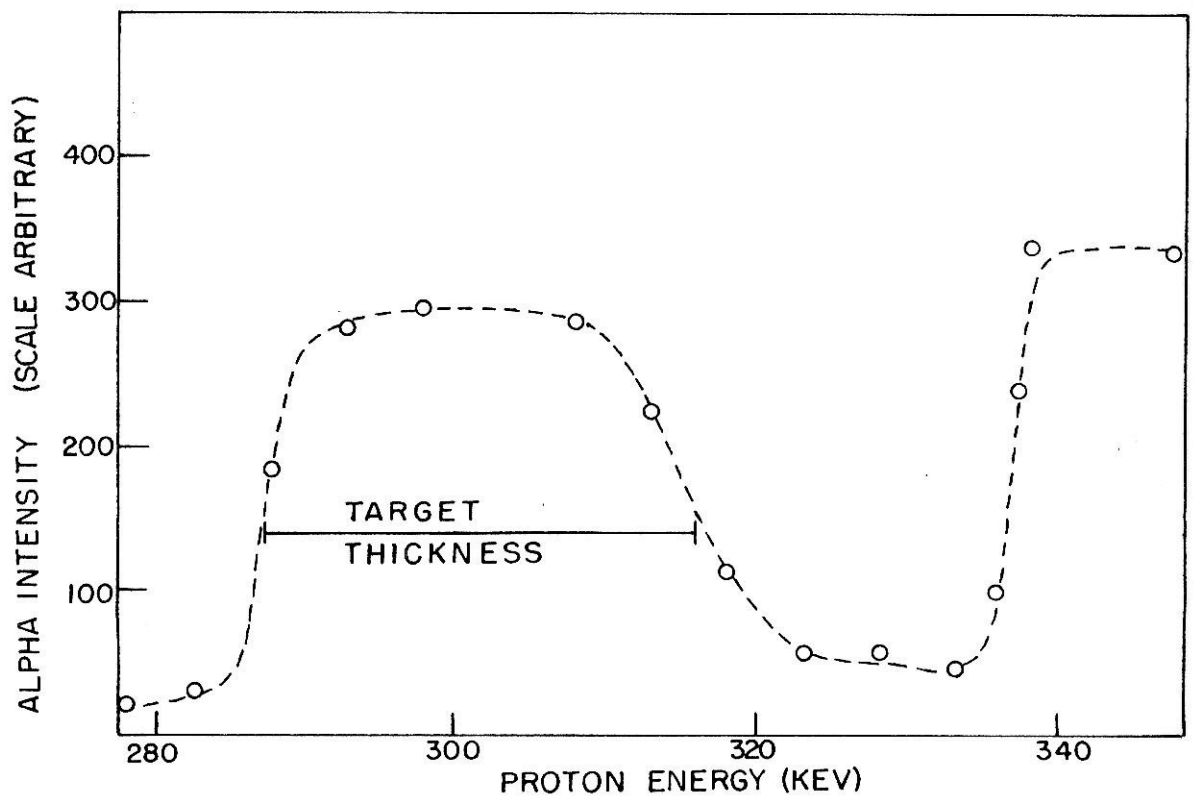
ALPHA INTENSITY (SCALE ARBITRARY)
400
300
200
100
TARGET
THICKNESS
280
300
320
340
PROTON ENERGY (KEV)

Figure 5. Excitation function for the 4 Mev alpha group observed when sodium chloride targets were bombarded by protons. The 160 kev resonance in the $B^{11}(p, \alpha)Be^{8*}(2\alpha)$ reaction is clearly indicated.

(See page 6.)

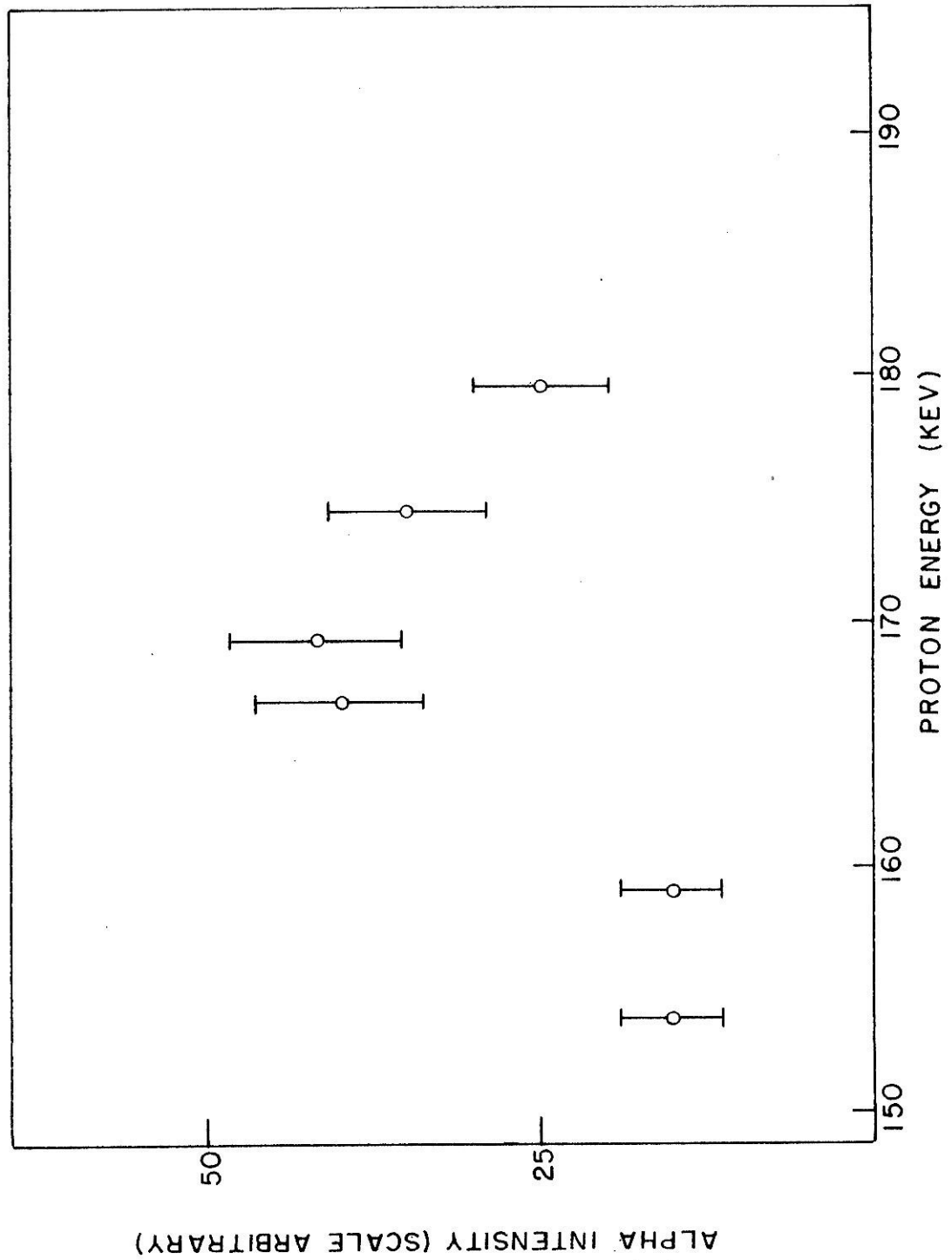
ALPHA INTENSITY (SCALE ARBITRARY)
50
25
150
160
170
180
190
PROTON ENERGY (KEV)

Figure 6. Energy spectrum of alpha particles from the $B^{11}(p, \alpha)Be^{8*}(2\alpha)$ reaction. The solid curve is the one given by Beckman et al. for an angle of 97 degrees and a proton energy of 700 kev. The dotted curve is the one given by Dearnaley et al. for an angle of 90 degrees and a proton energy of 530 kev. The quantities E_L, E_U, A_U, and A are included for the purpose of clarifying the discussion in section III B of part I. (See pages 6 and 14ff.)

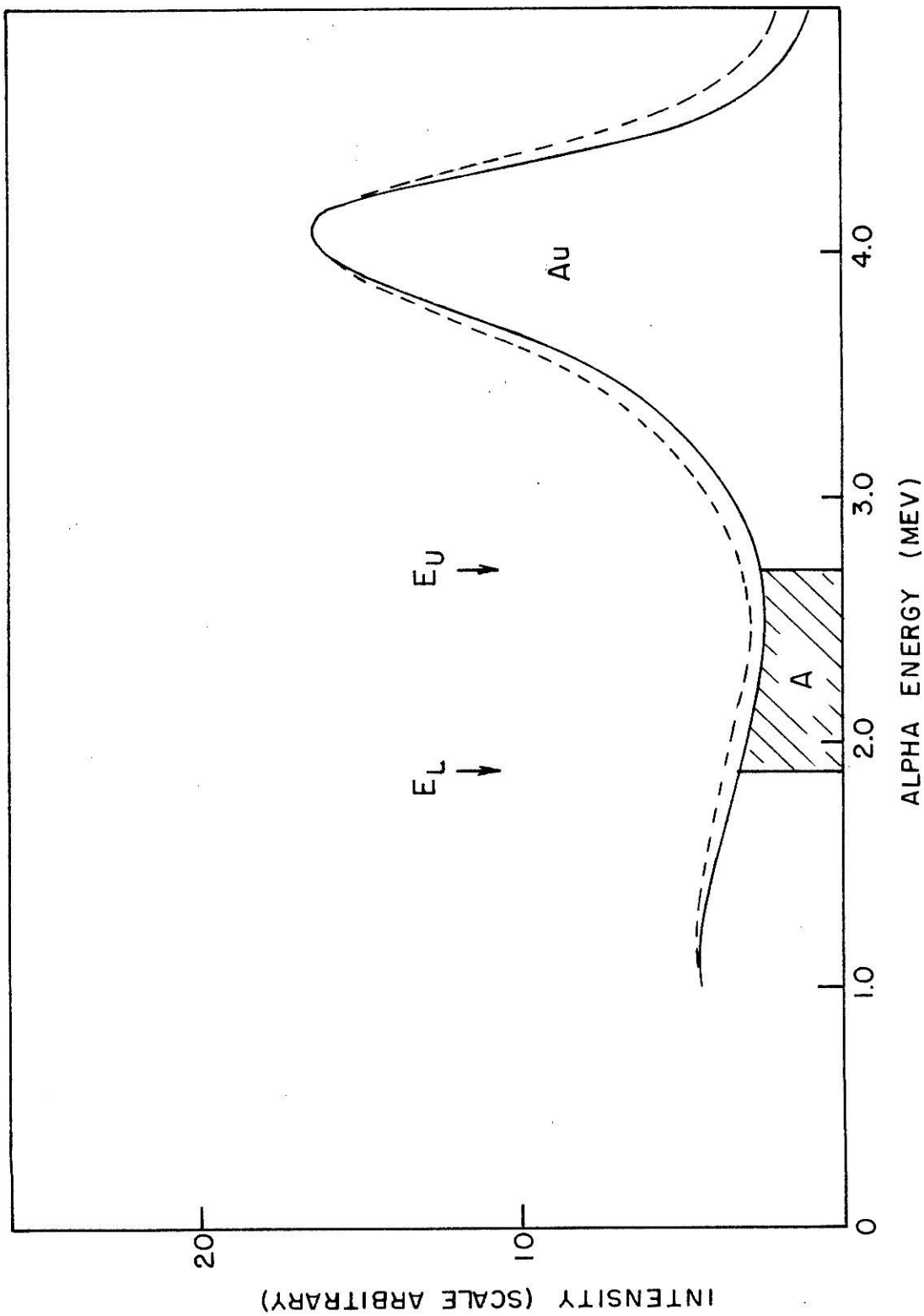
INTENSITY (SCALE ARBITRARY)
20
10
0
1.0
2.0
3.0
4.0
ALPHA ENERGY (MEV)
Au
A
E_U
E_L

Figure 7. Pulse height spectrum of alpha particles obtained when NaCl target is bombarded by protons. The spectrum has been divided into two parts. The top part, which covers channels 0 to 140, shows the peak from the reaction $Na^{23}(p, \alpha)Ne^{20}$. The proton energy is 345 kev, just above the 338 kev resonance in this reaction. The width of the peak is not due to the energy spread of the alpha particles, but to the resolution of the counter and straggling in the gold foil. The edge below channel 20 is due to elastically scattered protons and to counter noise. The bottom part of this figure, covering channels 140 to 400, shows the peak from the reaction $B^{11}(p, \alpha)Be^{8*}$ due to a small boron contaminant in the target. Note the difference in the ordinate scale, which is counts/4 channels rather than counts/channel. The width of this peak is mainly due to the width of the 2.9 Mev excited state of Be^{8} which is 1.5 Mev. V_U and V_L show the upper and lower discriminator bias settings. (See pages 7, 8, 12, and 14.)

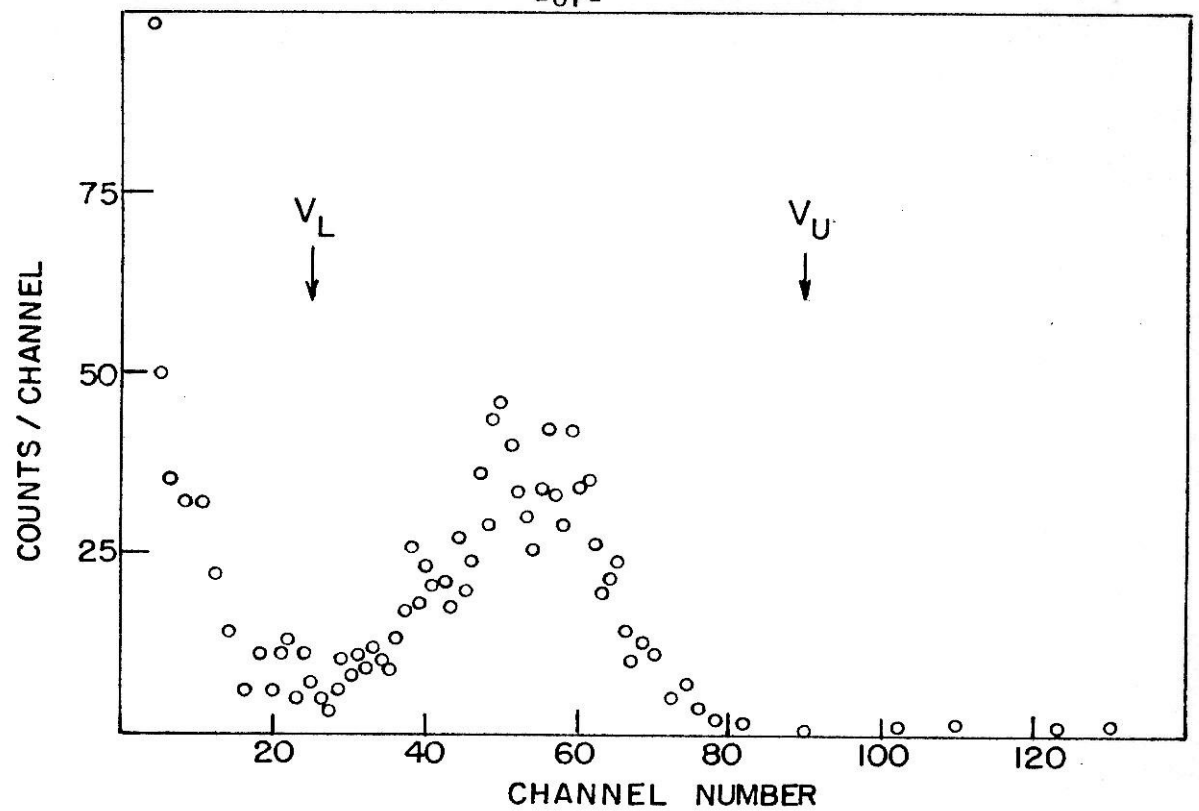
75
50
25
V_L
V_U
COUNTS / CHANNEL
20
40
60
80
100
120
CHANNEL NUMBER

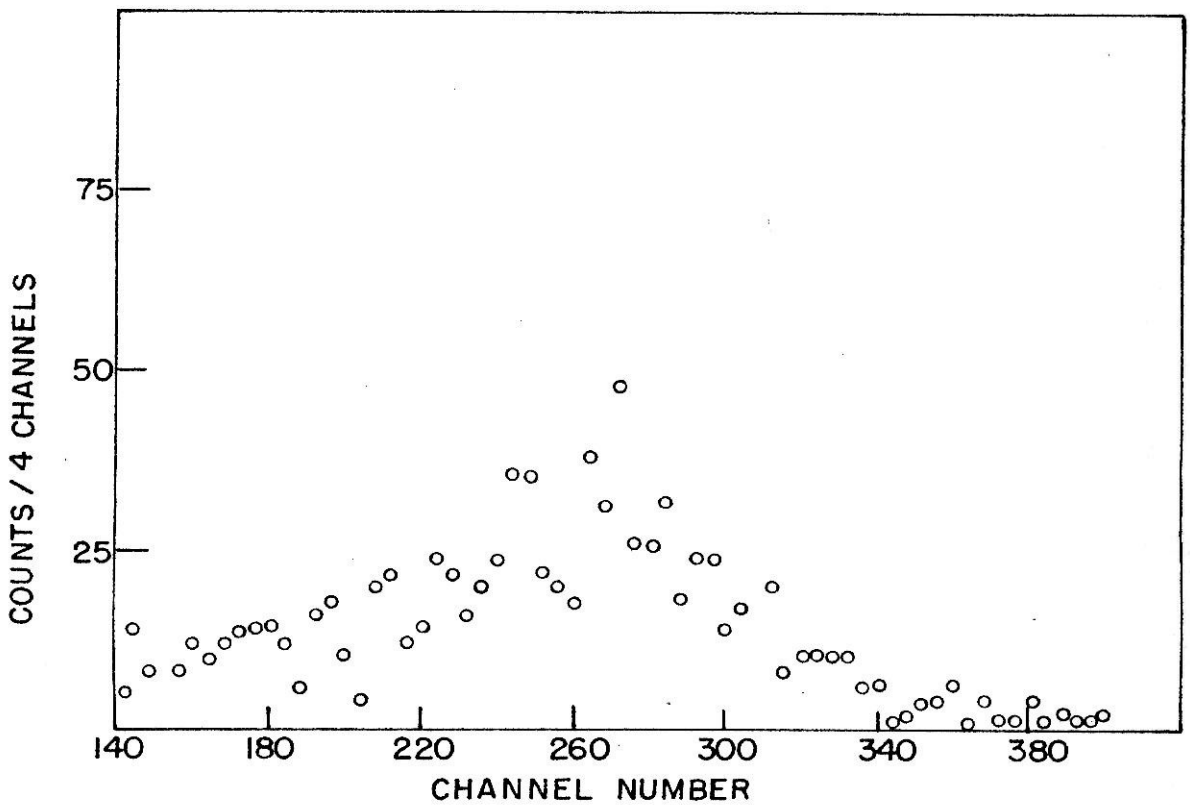
75
50
25
COUNTS / 4 CHANNELS
140
180
220
260
300
340
380
CHANNEL NUMBER

Figure 8. Pulse height spectrum of alpha particles from ThC' obtained with solid state counter. (See page 7.)

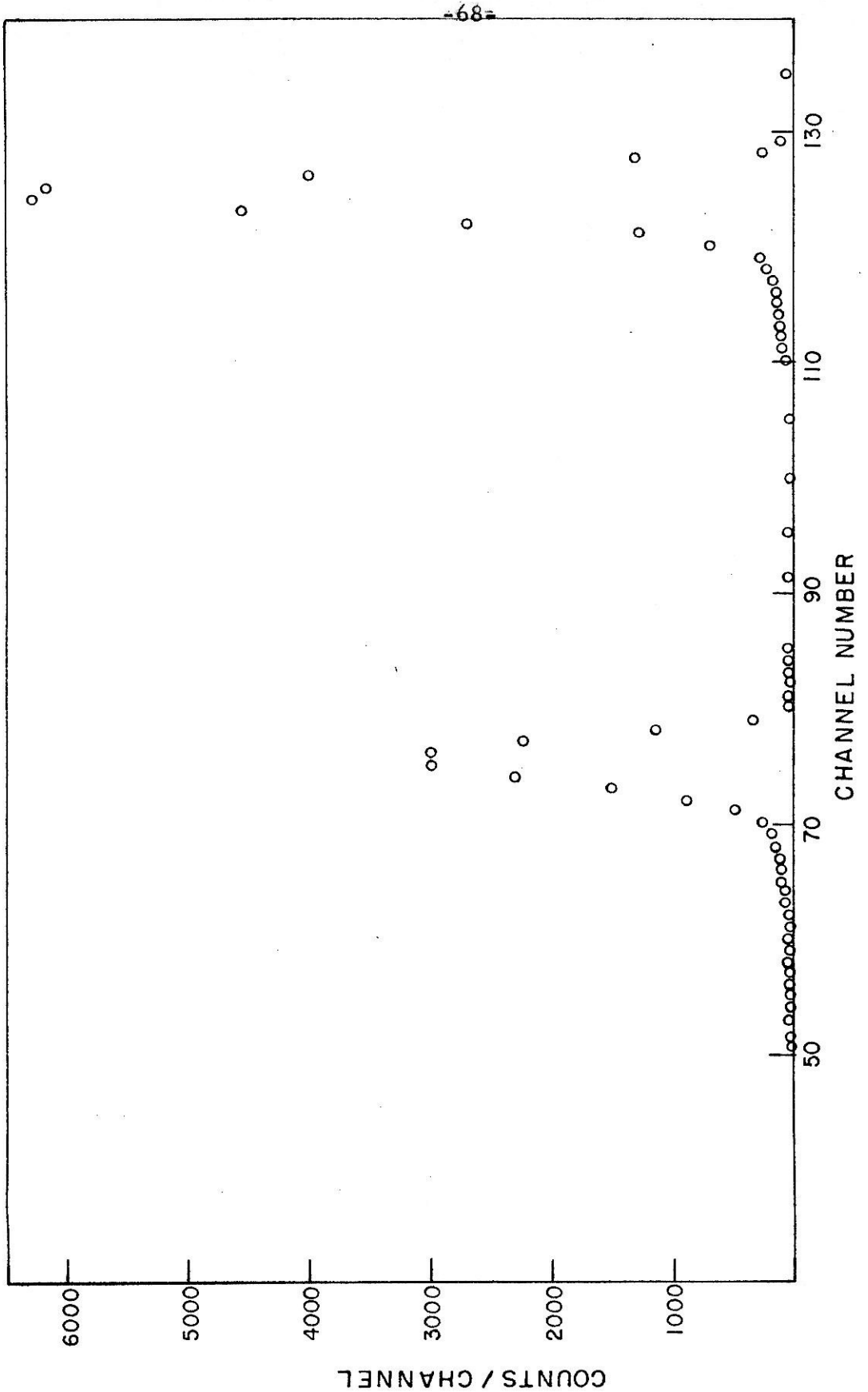
COUNTS / CHANNEL
6000
5000
4000
3000
2000
1000
50
70
90
110
130
CHANNEL NUMBER

Figure 9. Current integrator and calibration apparatus. The calibration apparatus is enclosed by a dotted line. The complete circuit of the current integrator is not shown, but only that part relevant to the discussion of the calibration procedure in section II D of part I. (See page 9 ff.)

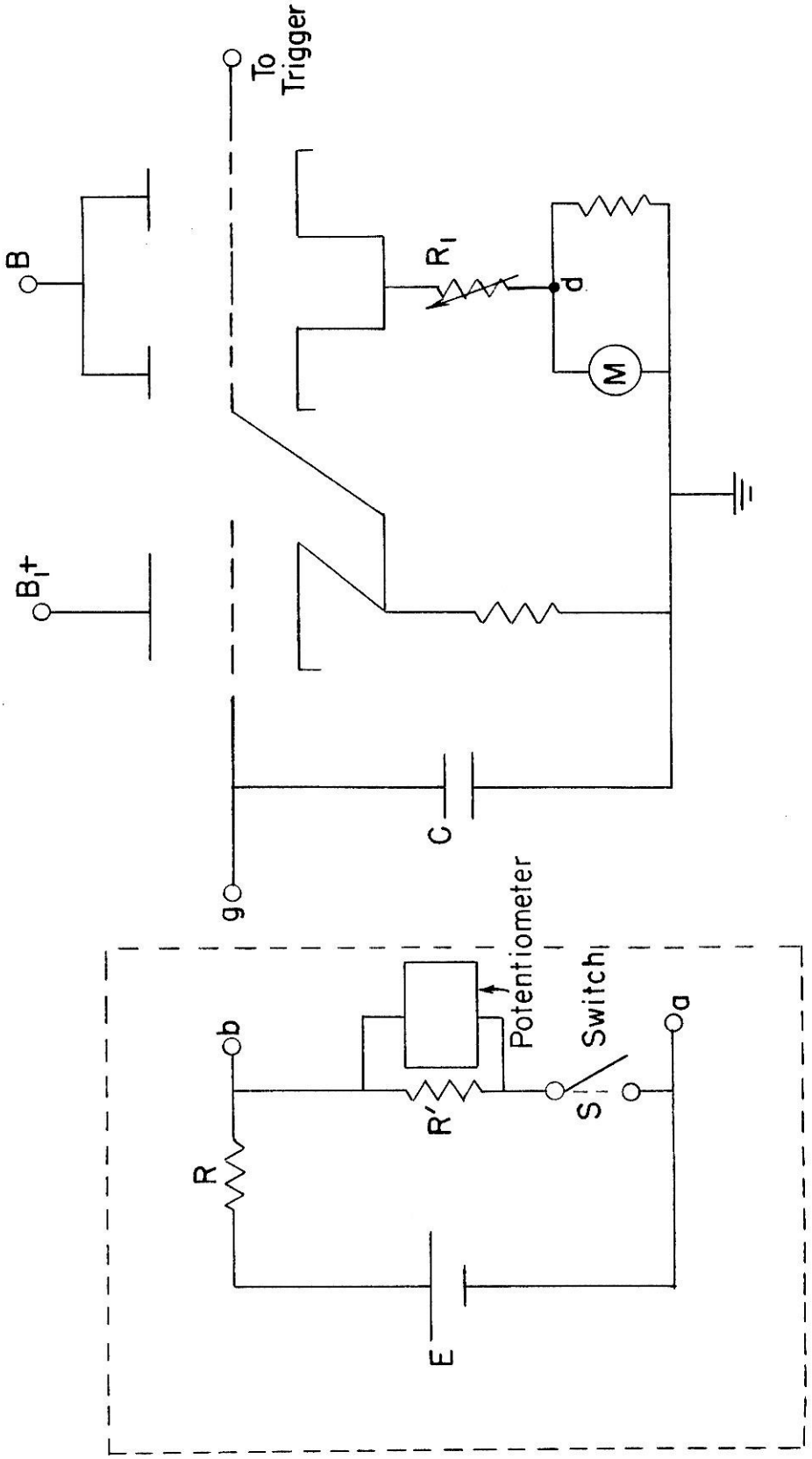
To Trigger
B
R_1
d
M
B_1+
C
g
Potentiometer
Switch
b
a
R'
S
R
E

Figure 10. Excitation function at 90° for the 286 kev resonance in the $Na^{23}(p, \alpha)Ne^{20}$ reaction. The ordinate scale is unnormalized and gives the number of alpha counts recorded for 8 integrators using a 1 μfarad capacitor. The charge per integrator is 95.2 μcoulombs. (See page 16.)

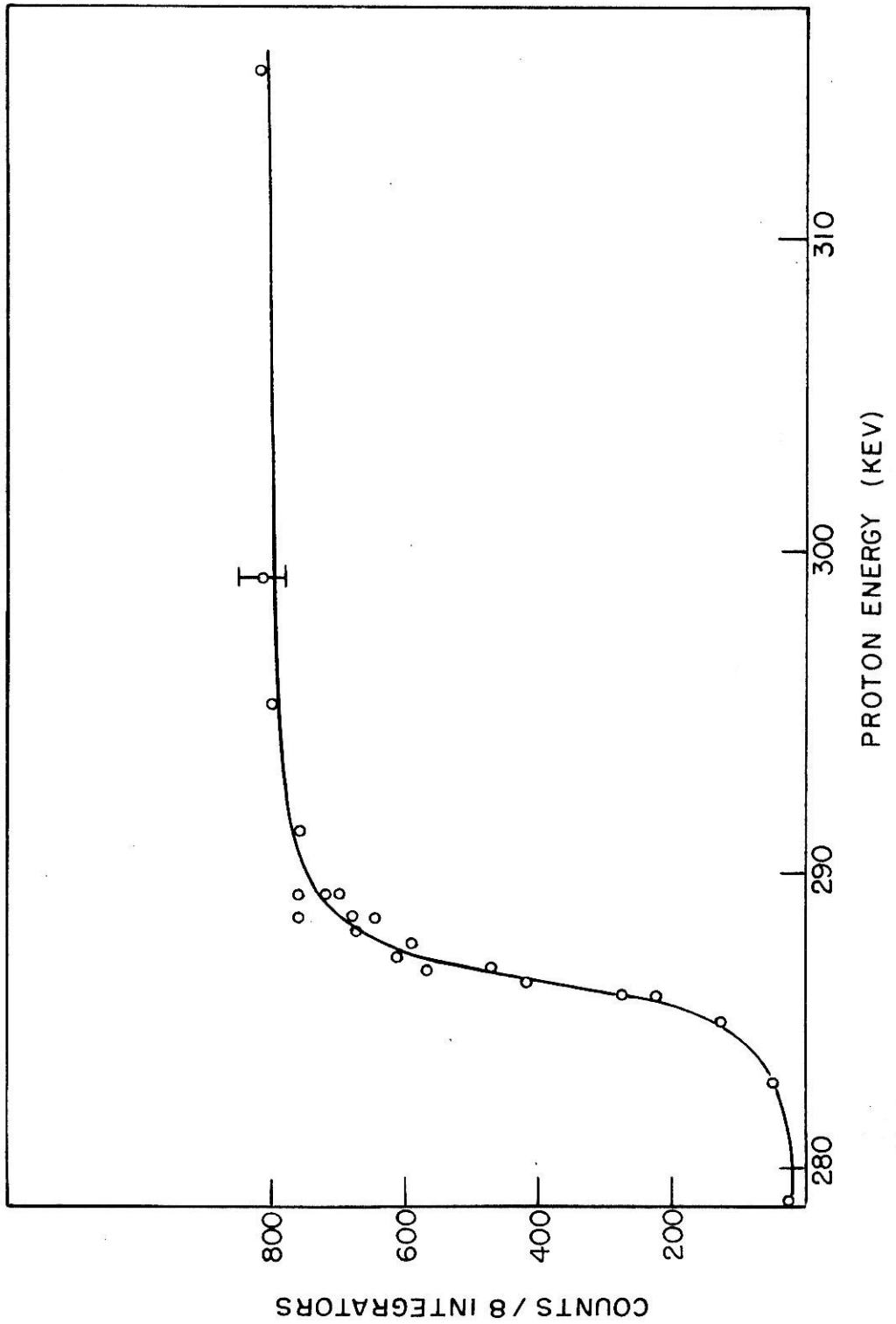
COUNTS / 8 INTEGRATORS
800
600
400
200
280
290
300
310
PROTON ENERGY (KEV)

Figure 11. Excitation function at 90° for the 338 kev resonance in the reaction $Na^{23}(p, \alpha)Ne^{20}$. The ordinate scale is unnormalized and gives alpha counts/8 integrators using a 1 μfarad capacitor. The charge per integrator is 95.2 μcoulombs. (See page 17.)

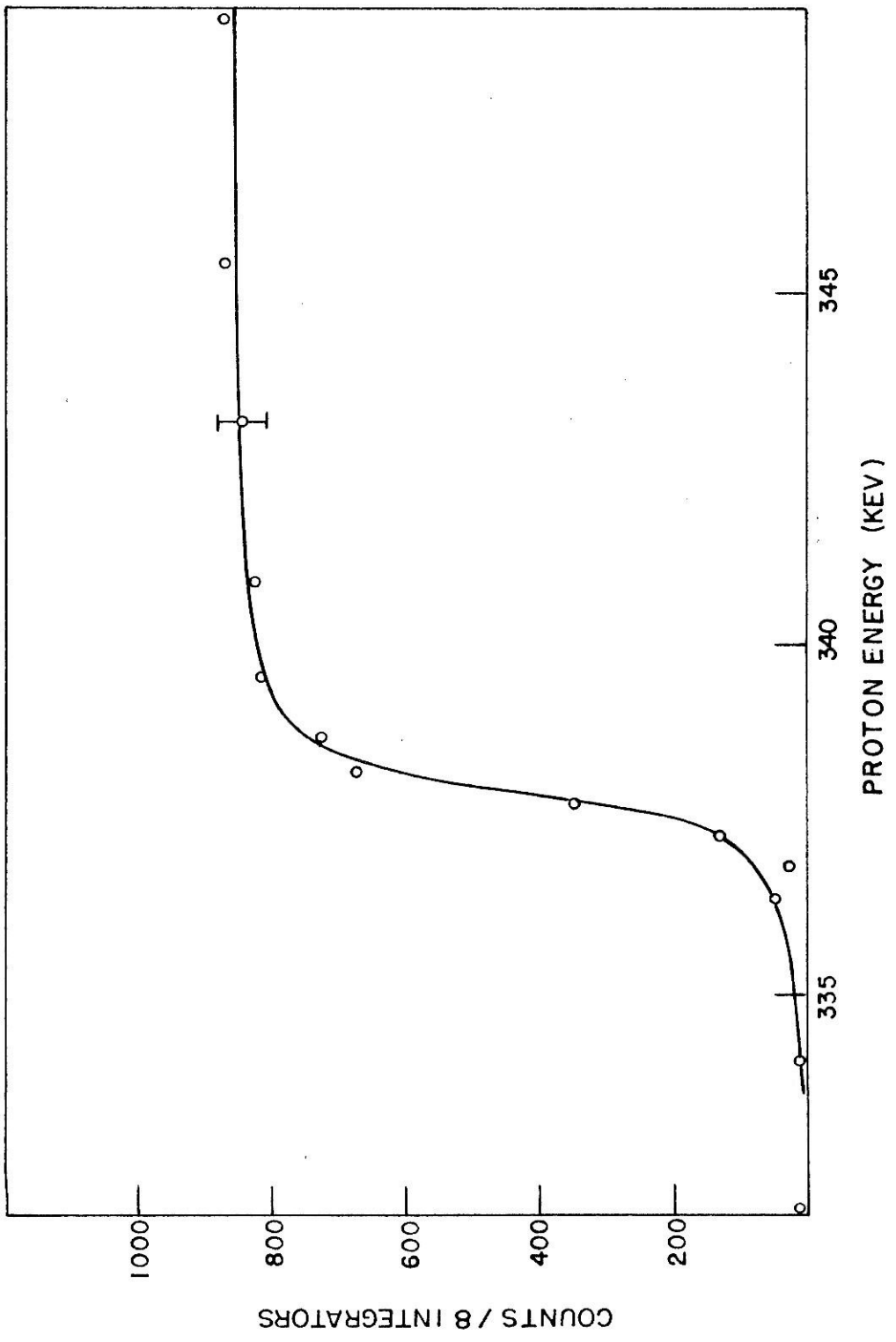
COUNTS / 8 INTEGRATORS
1000
800
600
400
200
335
340
345
PROTON ENERGY (KEV)

Figure 12. Excitation function at 90° for the 374 kev resonance in the reaction $Na^{23}(p, \alpha)Ne^{20}$. The ordinate scale is unnormalized and gives counts/24 integrators obtained with a 1 μfarad capacitor. The charge/integrator is 95.2 μcoulombs. The three curves represent three different assumptions for the resonance width Γ with E_R chosen to give the best fit in each case. They have been computed for a target thickness of 10 kev, as explained in section III C of part I. (See pages 17, 18.)

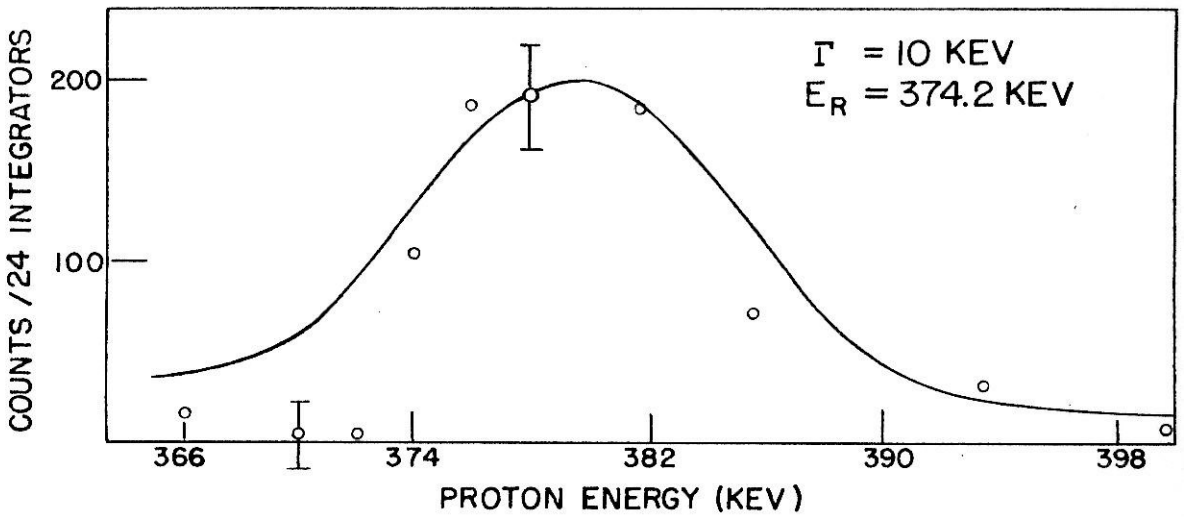
Γ = 10 KEV
E_R = 374.2 KEV
COUNTS /24 INTEGRATORS
200
100
366
374
382
390
398
PROTON ENERGY (KEV)

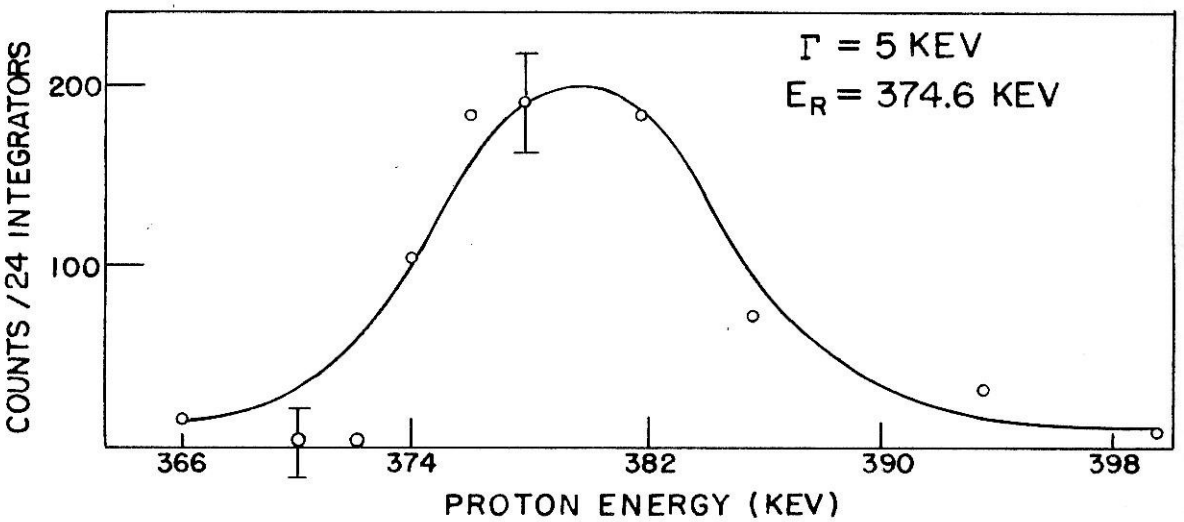
Γ = 5 KEV
E_R = 374.6 KEV
COUNTS /24 INTEGRATORS
200
100
366
374
382
390
398
PROTON ENERGY (KEV)

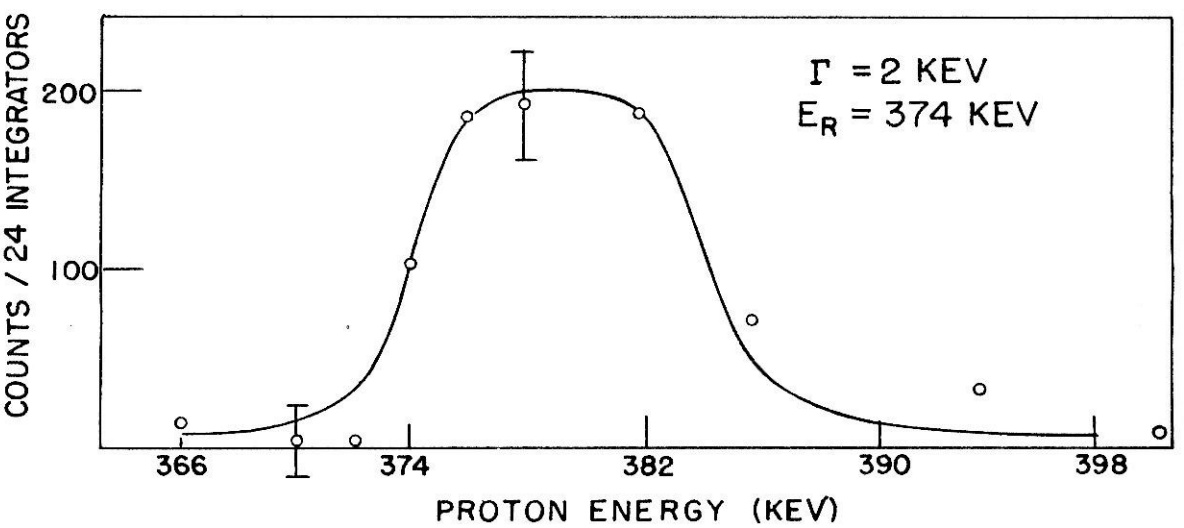
Γ = 2 KEV
E_R = 374 KEV
COUNTS / 24 INTEGRATORS
200
100
366
374
382
390
398
PROTON ENERGY (KEV)

Figure 13. This figure is the same as figure 12, but the curves have been computed for different assumptions for the resonance energy E_R with Γ chosen to give the best fit. (See page 18.)

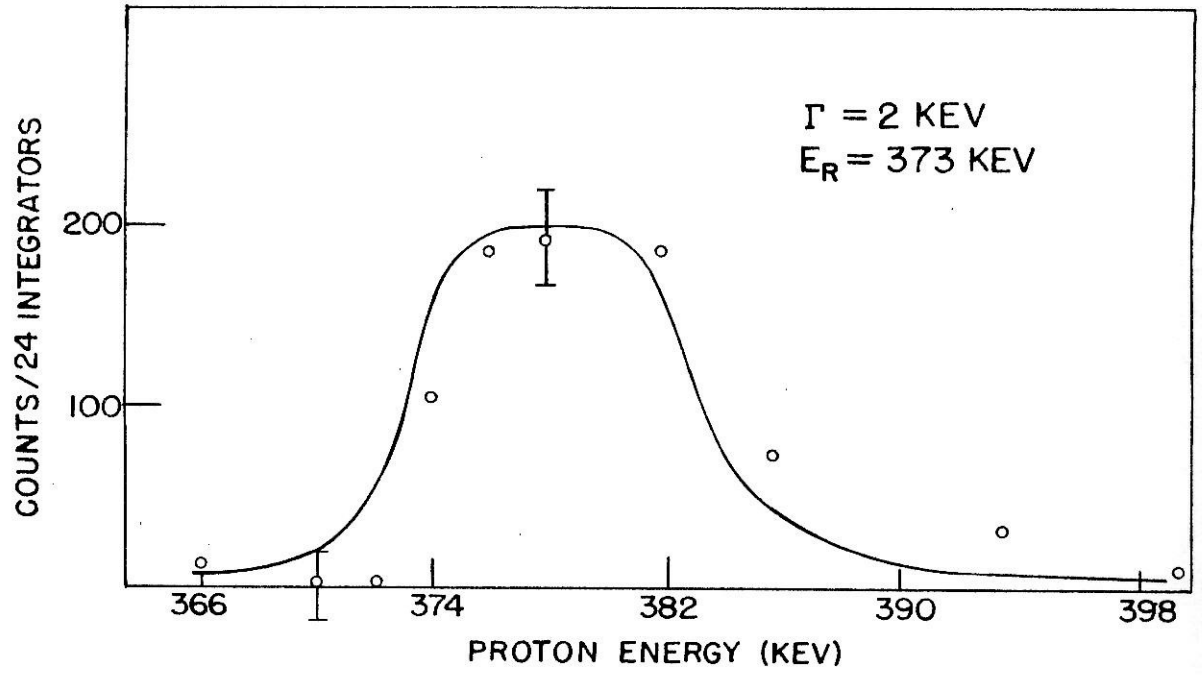
Γ = 2 KEV
E_R = 373 KEV
COUNTS/24 INTEGRATORS
200
100
366
374
382
390
398
PROTON ENERGY (KEV)

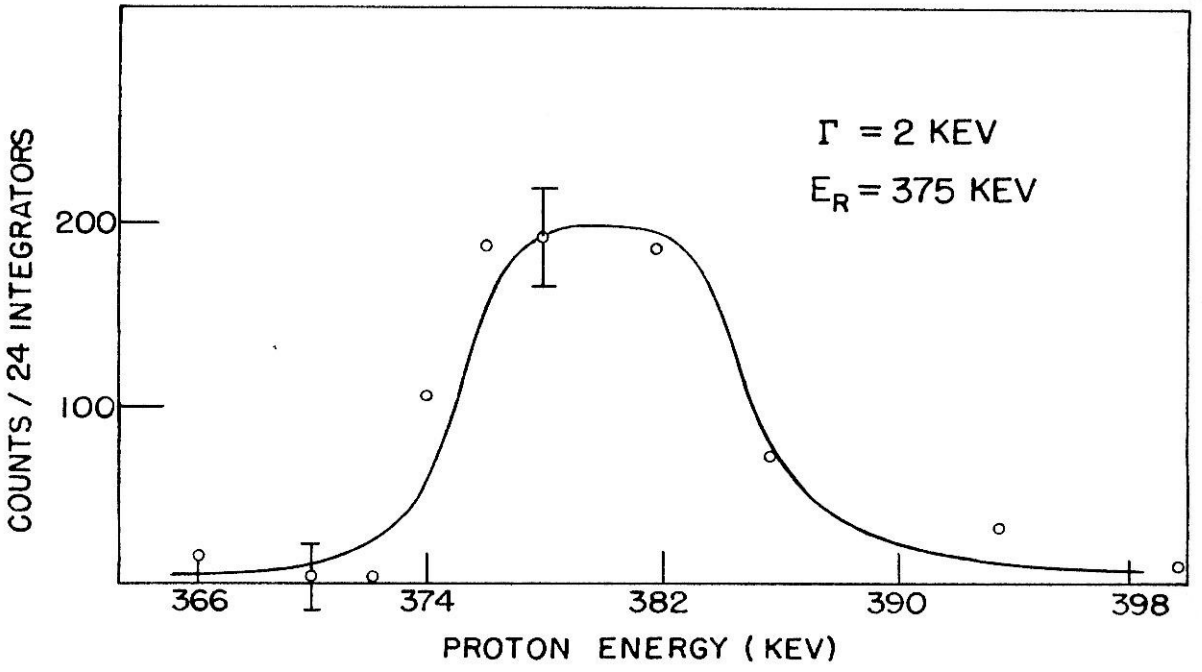
Γ = 2 KEV
E_R = 375 KEV
COUNTS / 24 INTEGRATORS
200
100
366
374
382
390
398
PROTON ENERGY (KEV)

Figure 14. Pulse height spectra of alpha particles from the reaction $Na^{23}(p, \alpha)Ne^{20}$ in the region of the 445 kev resonance. The arrow indicates the expected position of the alpha peak on the basis of the position of the peak at the 338 kev resonance. The counter angle is 140°. (See page 20.)

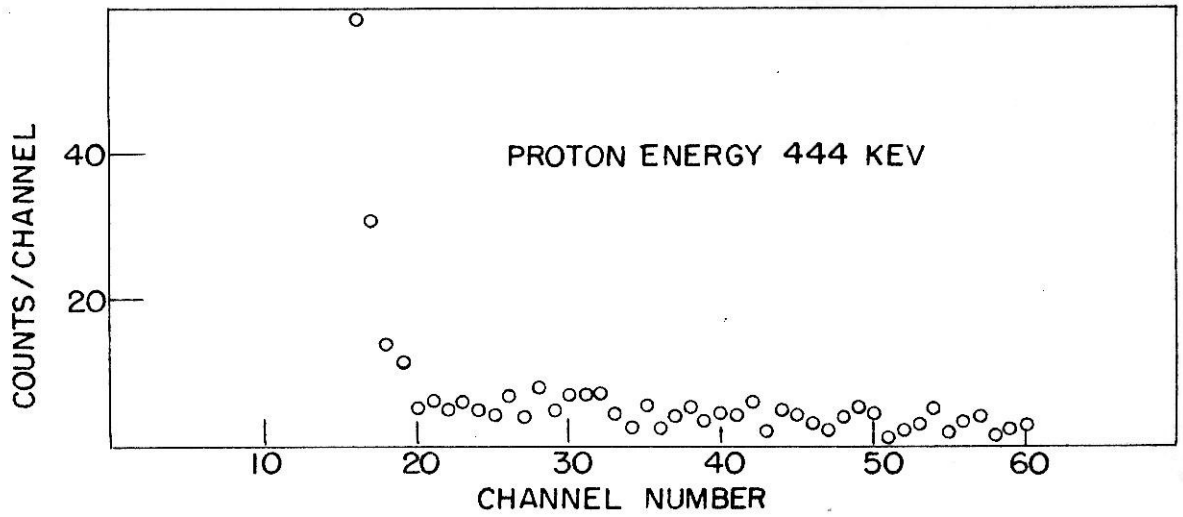
PROTON ENERGY 444 KEV
COUNTS / CHANNEL
40
20
10
20
30
40
50
60
CHANNEL NUMBER

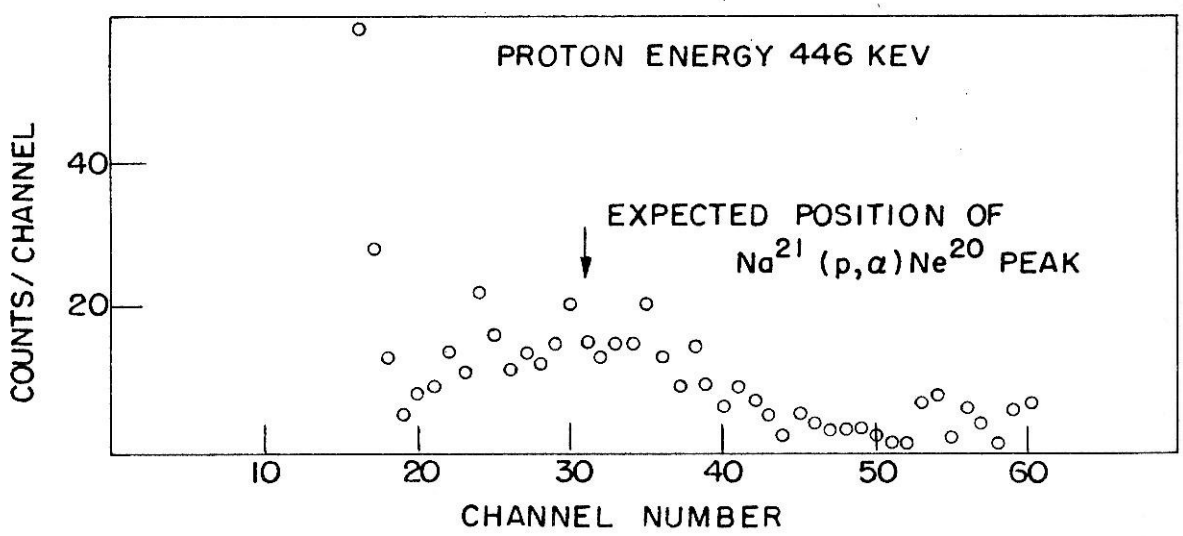
PROTON ENERGY 446 KEV
EXPECTED POSITION OF
Na21 (p,α) Ne20 PEAK
COUNTS / CHANNEL
40
20
10
20
30
40
50
60
CHANNEL NUMBER

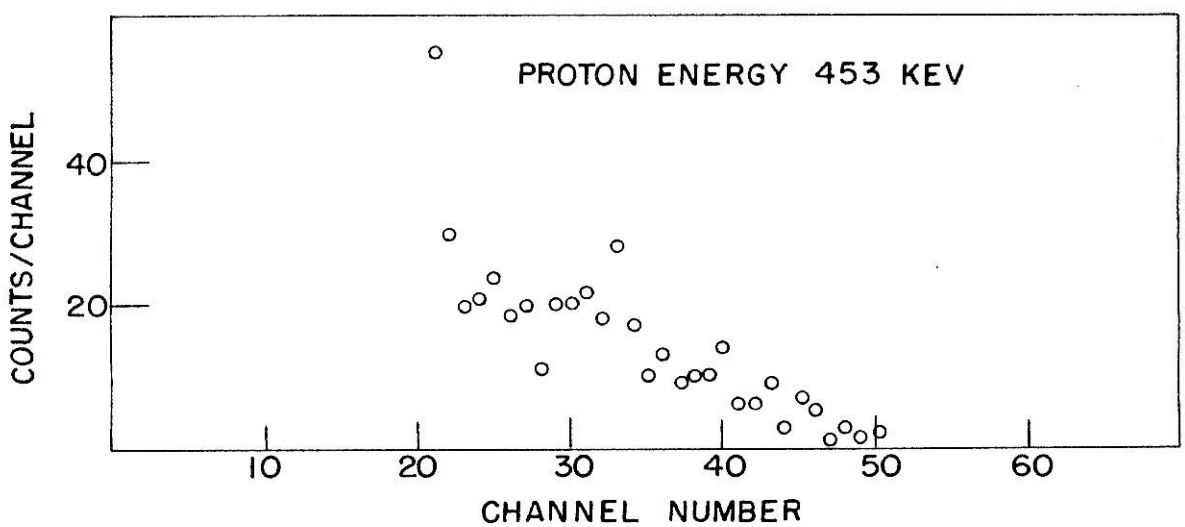
PROTON ENERGY 453 KEV
COUNTS/CHANNEL
40
20
10
20
30
40
50
60
CHANNEL NUMBER

Figure 15. Excitation function at 140° for the 445 kev resonance in the reaction $Na^{23}(p, \alpha)Ne^{20}$. The ordinate scale is unnormalized and gives alpha counts/16 integrators with a 1 μfarad capacitor. The charge/integrator is 95.2 μcoulombs. (See page 20.)

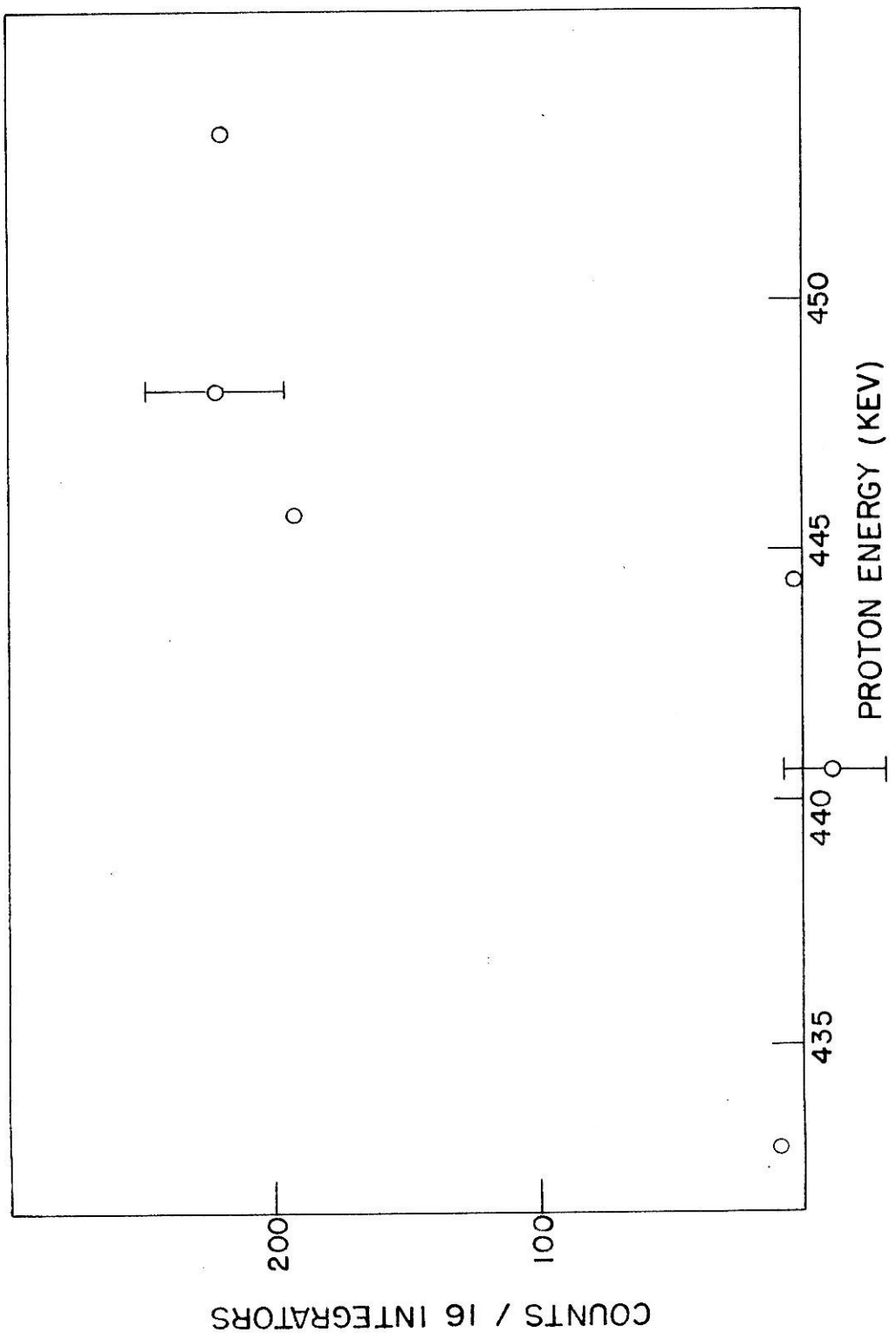
COUNTS / 16 INTEGRATORS
200
100
435
440
445
450
PROTON ENERGY (KEV)

Figure 16. Non-resonant differential cross section at 90° for the reaction $Na^{23}(p, \alpha)Ne^{20}$. Because of the large uncertainties in the points, they can be used only to establish an upper limit for the cross section factor S as discussed in section III D of part I. The solid curve in the figure represents S = 100 Mev barns, if the non-resonant cross section is assumed isotropic. (See page 23.)

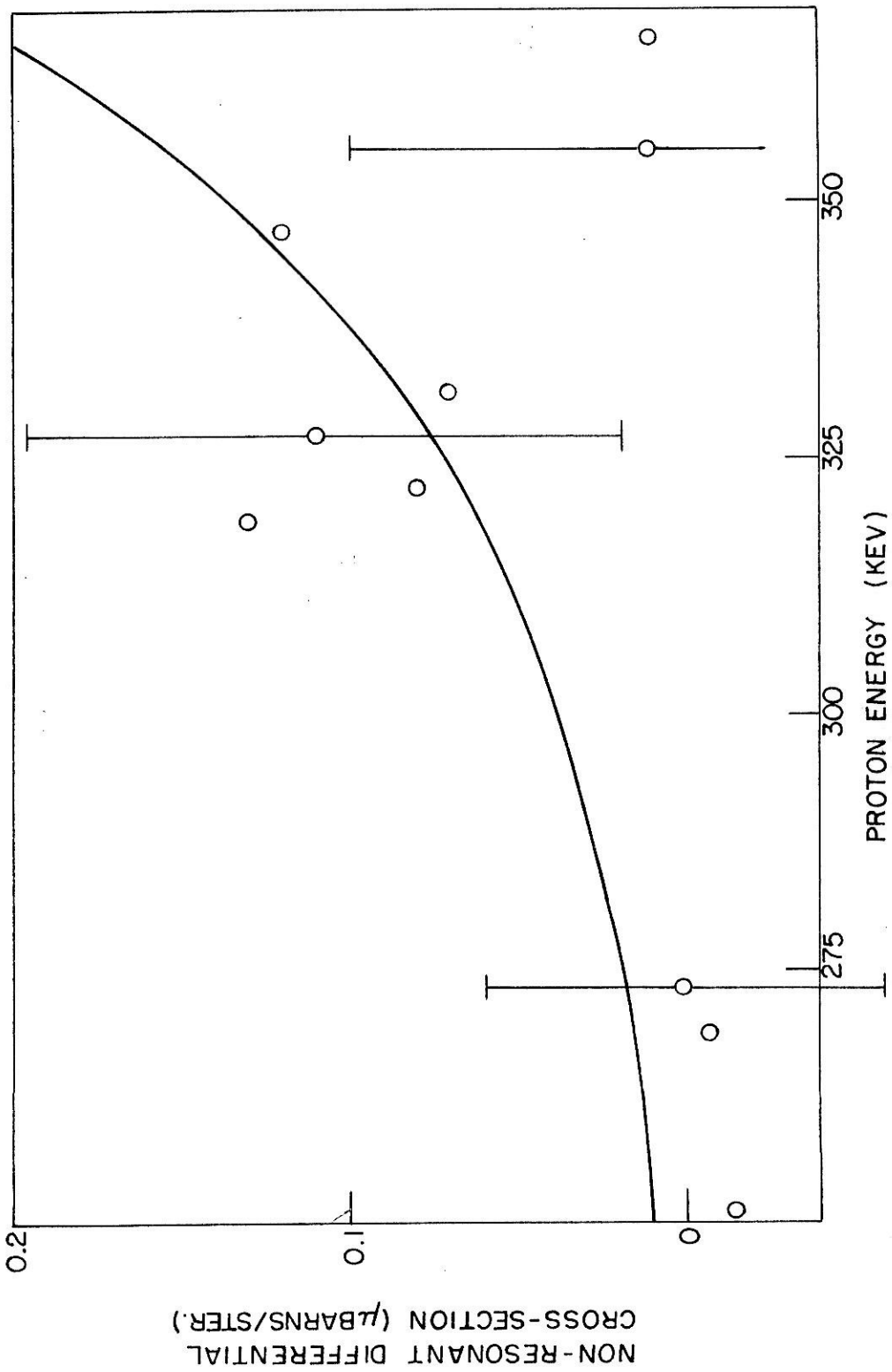
NON-RESONANT DIFFERENTIAL
CROSS-SECTION (μBARNS/STER.)
0.2
0.1
0
275
300
325
350
PROTON ENERGY (KEV)

Figure 17. Excitation function at 90° for the reaction $Na^{23}(p, \alpha)Ne^{20}$ covering the energy region from 120 to 215 kev. There is some indication of a resonance at about 170 kev. The ordinate scale gives counts/24 integrators with a 1 μfarad capacitor. The charge/integrator is 95.2 μcoulombs. (See page 24.)

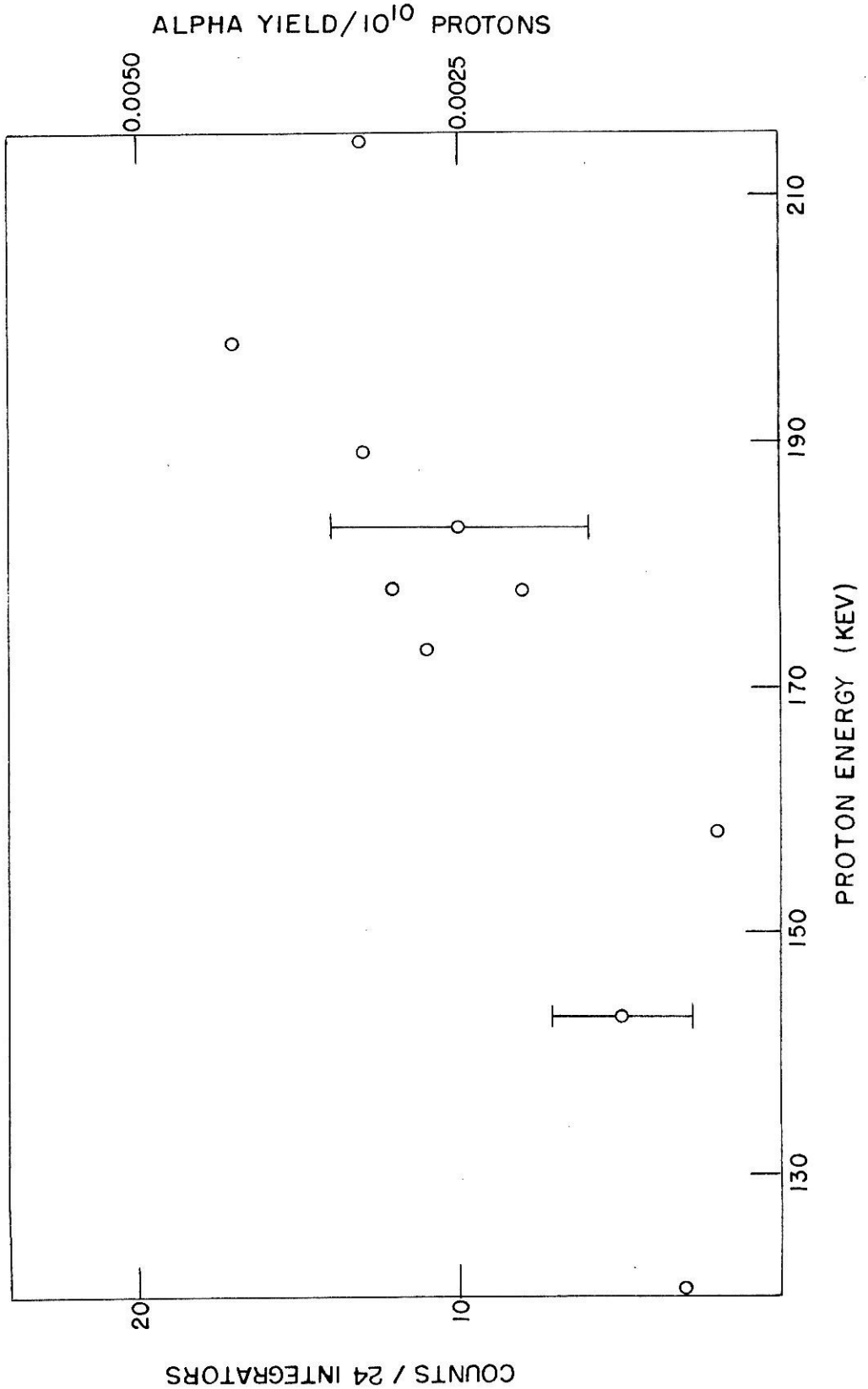
ALPHA YIELD/10^10 PROTONS
0.0050
0.0025
210
190
170
150
130
PROTON ENERGY (KEV)
20
10
COUNTS / 24 INTEGRATORS

Figure 18. Angular distribution of alpha particles from 286 kev resonance in the $Na^{23}(p, \alpha)Ne^{20}$ reaction. Center of mass corrections have been made. The solid curve is a least squares fit. The corresponding values of B_2/B_0 and B_4/B_0 are given. (See page 36.)

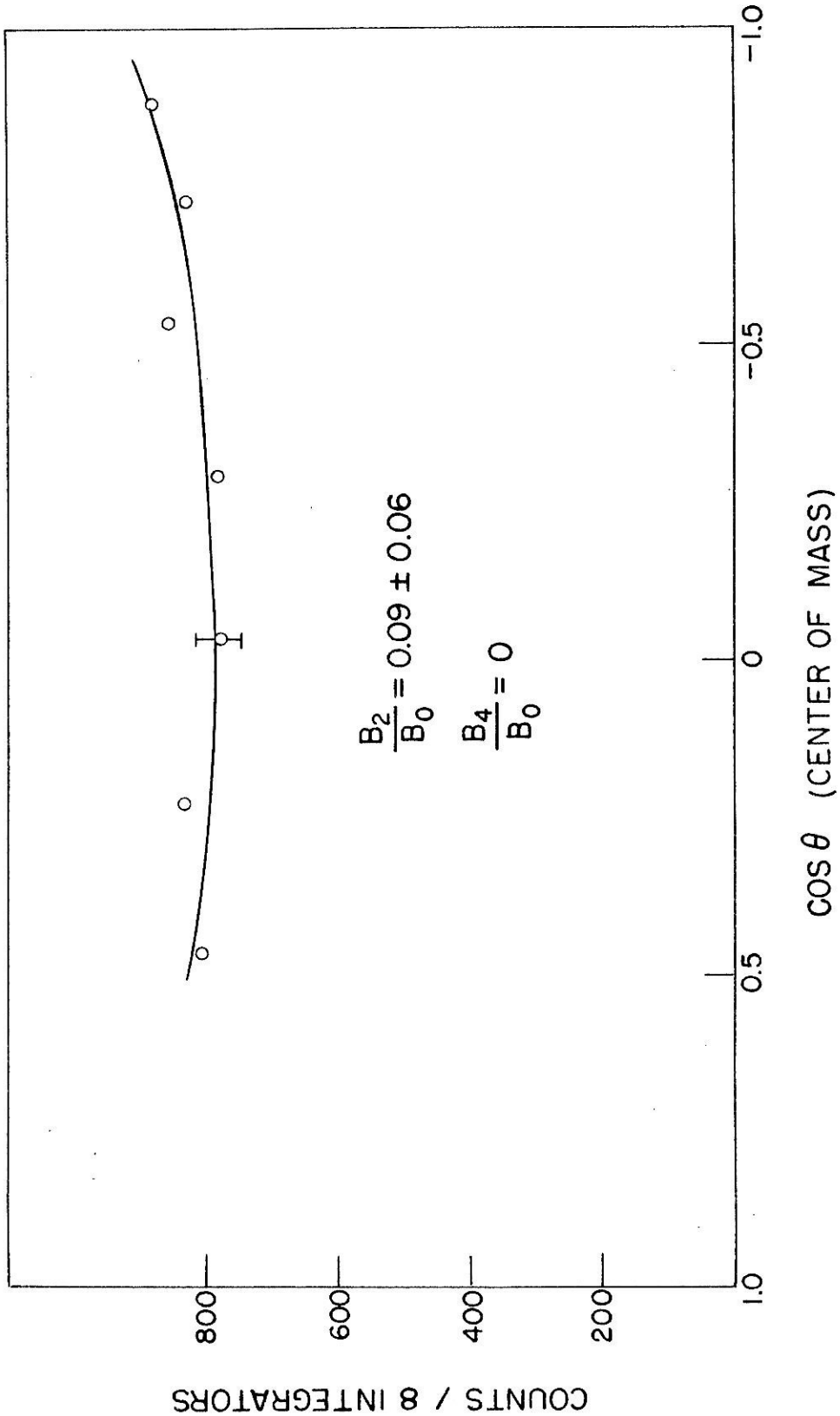
COUNTS / 8 INTEGRATORS
800
600
400
200
1.0
0.5
0
-0.5
-1.0
COS θ (CENTER OF MASS)
$\frac{B_2}{B_0} = 0.09 \pm 0.06$
$\frac{B_4}{B_0} = 0$

Figure 19. Angular distribution of alpha particles from the 338 kev resonance in the reaction $Na^{23}(p, \alpha)Ne^{20}$. Center of mass corrections have been made. The solid curve is a least squares fit, and the values of B_2/B_0 and B_4/B_0 are shown. (See page 37.)

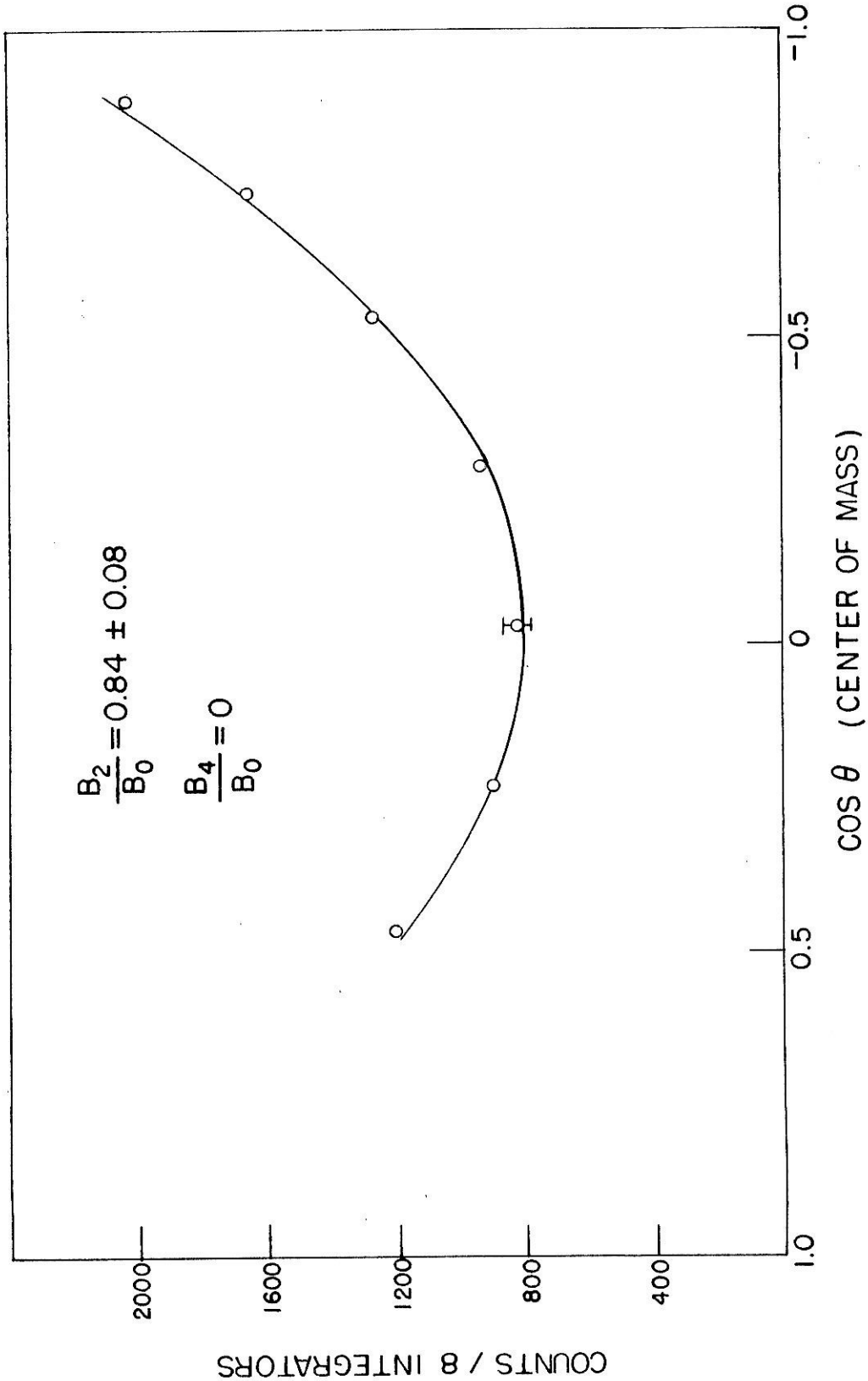
$\frac{B_2}{B_0} = 0.84 \pm 0.08$
$\frac{B_4}{B_0} = 0$
COUNTS / 8 INTEGRATORS
2000
1600
1200
800
400
1.0
0.5
0
-0.5
-1.0
COS θ (CENTER OF MASS)

Figure 20. Angular distribution of alpha particles from 374 kev resonance in the reaction $Na^{23}(p, \alpha)Ne^{20}$. Center of mass corrections have been made. The solid curve is a least squares fit, and the values of B_2/B_0 and B_4/B_0 are shown. The dotted curve shows the predicted distribution if the state has $J^{\pi} = 5^-$ and is included as the most convenient means of eliminating this assignment. (See page 38.)

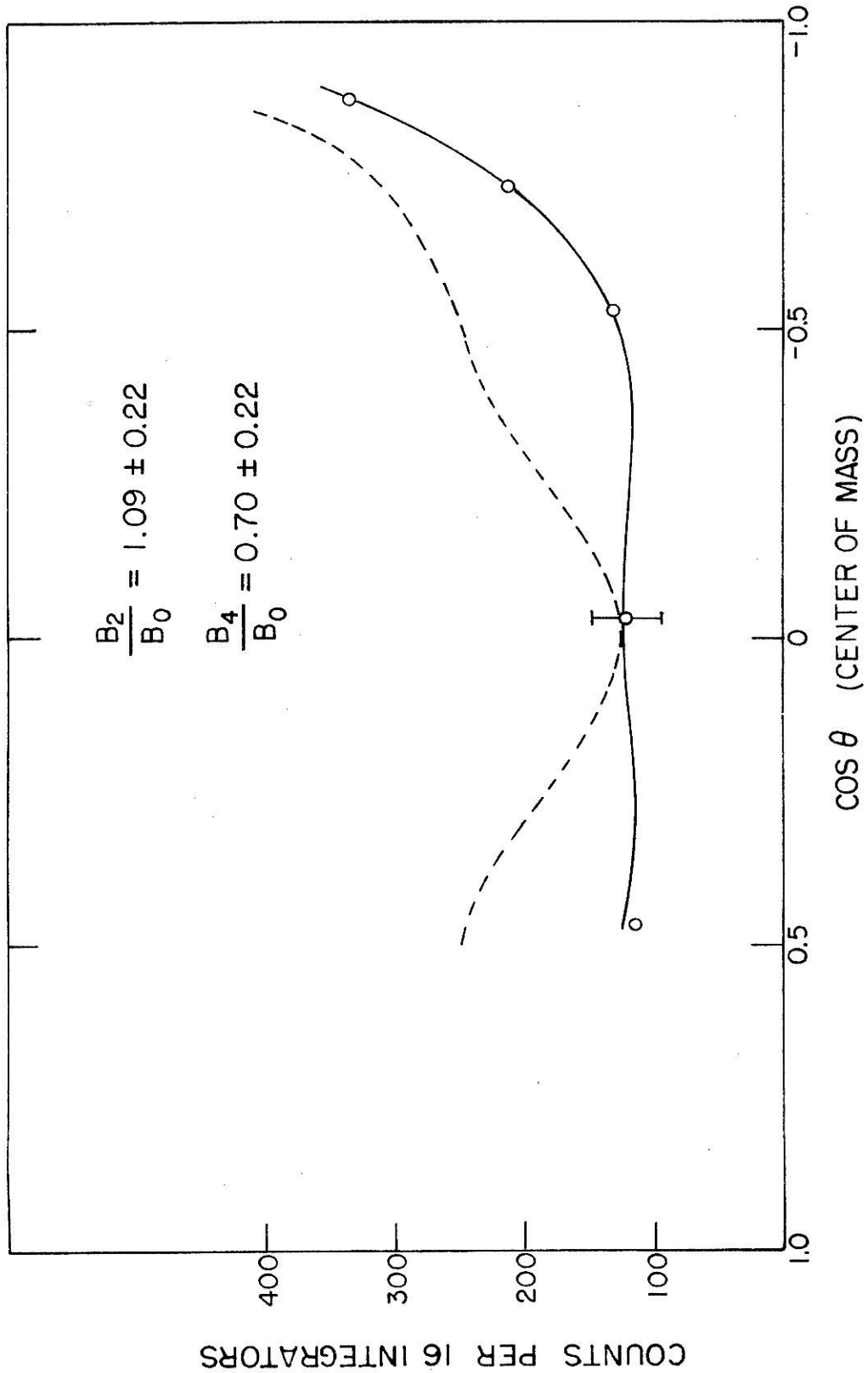
$\frac{B_2}{B_0} = 1.09 \pm 0.22$
$\frac{B_4}{B_0} = 0.70 \pm 0.22$
COUNTS PER 16 INTEGRATORS
400
300
200
100
1.0
0.5
0
-0.5
-1.0
COS θ (CENTER OF MASS)

Figure 21. Stopping cross sections of argon, chlorine, aluminum, sodium, and neon. The curves for argon, aluminum, and neon have been taken from the data of Whaling. The curves for chlorine and sodium have been obtained by the interpolation procedure described in Appendix II. The dotted curve for aluminum was also obtained by this interpolation procedure, and is shown to indicate its closeness to the actual experimental curve. (See page 53.)

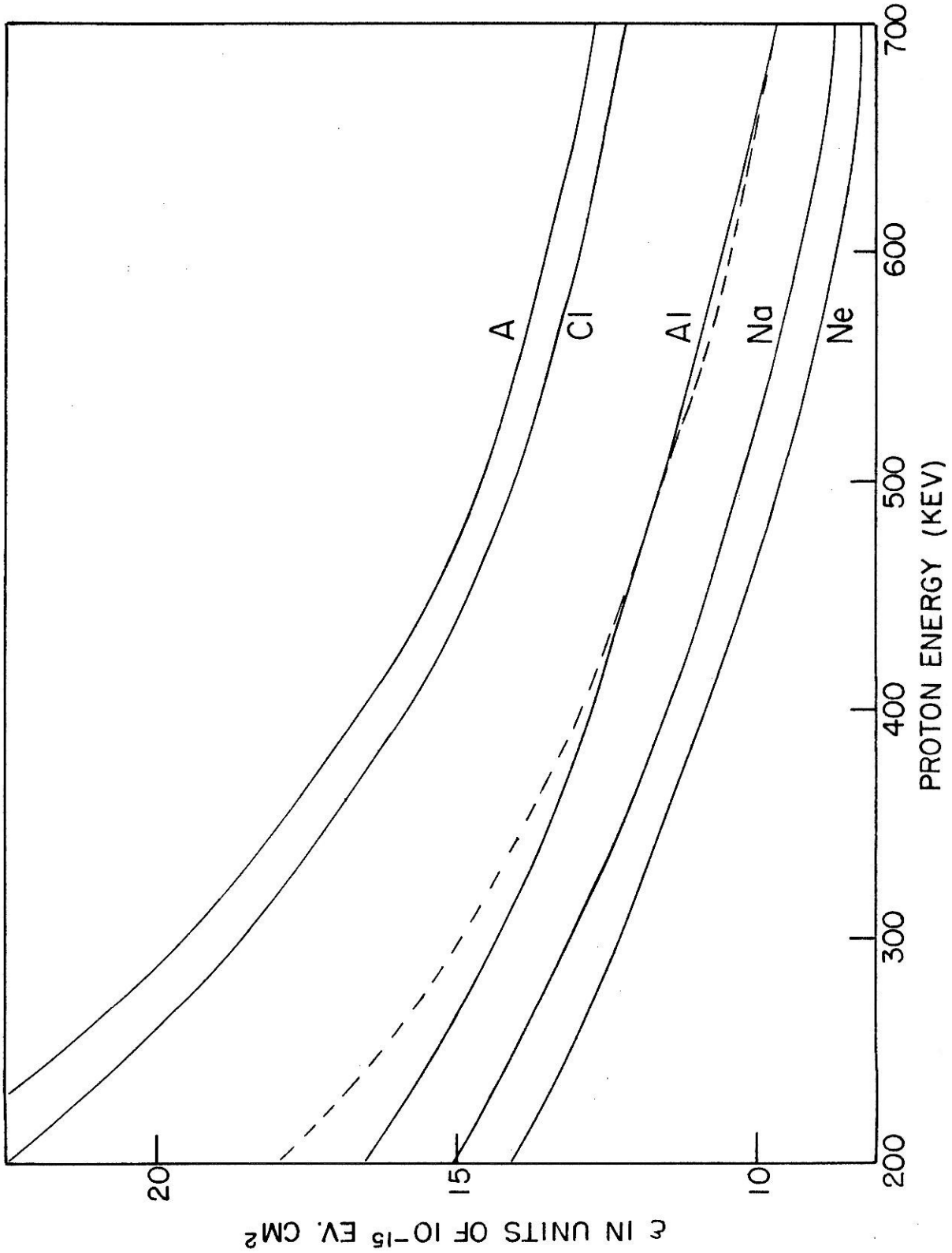
A
Cl
Al
Na
Ne
20
15
10
200
300
400
500
600
700
PROTON ENERGY (KEV)
ε IN UNITS OF 10⁻¹⁵ EV. CM²

PART II

A MEASUREMENT OF THE N^{12} AND B^{12} HALF-LIVES

I. INTRODUCTION

Several previous measurements of the B^{12} and N^{12} half-lives have been made, and these are listed in table 1. At the time the present experiment was undertaken, the most recent measurement by Peterson and Glass[7] had not been completed. At this time, then, only two published measurements of the N^{12} half-life existed and these were not in very good agreement. Although there were six published measurements of the B^{12} half-life there was some discrepancy among them, as can be seen from table 1. The discrepancy is reduced considerably if the measurement of Jelly and Paul[2] is disregarded.

The decays of B^{12} and N^{12} to the ground state and first two excited states of C^{12} are allowed Gamow-Teller transitions with $\Delta J = 1$, $\Delta T = 1$, $\Delta\pi$ no. For such decays, the ft value depends on the allowed Gamow-Teller matrix element $|\int \sigma|^2$. An uncertain knowledge of the nuclear wave functions prevents an exact calculation of this matrix element. Since N^{12} and B^{12} are mirror nuclei, however, we can say that the matrix elements and hence the ft values for the two decays will be identical if isotopic spin is conserved. Conservation of isotopic spin is expected to hold very well in the light nuclei, and an accurate comparison of the ft values for the N^{12} and B^{12} decays is an interesting experimental test of this hypothesis. We have undertaken the present experiment in order to obtain more reliable values for the half-lives of the two decays and thus make possible an accurate comparison of the ft values.

Table 1

Previous Measurements of B^{12} and N^{12} Half-lives

	$t_{1/2}$ in Milliseconds	Reference
B^{12}	22 ± 2	(1)
	27 ± 2	(2)
	22 ± 1	(3)
	$18^{+1.5}_{-1.3}$	(4)
	18.5 ± 1	(5)
	20.4 ± 0.4	(6)
	20.2 ± 0.2	(7)
N^{12}	12.5 ± 1	(8)
	11.2 ± 0.4	(6)
	11.0 ± 0.1	(7)

II. THEORY

The ft value for an allowed beta decay is given by:[9]

$$ft = \frac{B}{(1-x)\left|\int 1\right|^2 + x\left|\int \sigma\right|^2} \tag{1}$$

where B is a constant equal to 2620 seconds and x is equal to $C_A^2/(C_V^2+C_A^2)$. C_V and C_A are the Fermi and Gamow-Teller coupling constants. The experimental value of the ratio C_A/C_V is 1.2, so x = 0.6. t is the half-life, and the quantity $f = f(z, E_o)$ is given by:

$$f(z, E_o) = \frac{c^3}{(mc^2)^5} \int_0^{P_o} P^2(E_o - E)^2 F(z, E)dP \tag{2}$$

Here P and E represent the beta particle momentum and kinetic energy, P_o and E_o are the maximum values of these quantities, and m is the electron rest mass. F(z, E) is the Fermi function defined by:

$$F(z, E) = 2(1+\gamma)(2PR)^{2\gamma-2}(e^{\pi\eta}) \frac{\left|\Gamma(\gamma+i\eta)\right|^2}{\left|\Gamma(2\gamma+1)\right|^2} \tag{3}$$

All quantities in the above equation have their usual significance (see Reference 10). The quantities $\left|\int 1\right|^2$ and $\left|\int \sigma\right|^2$ appearing in equation 1 are standard abbreviations for the reduced Fermi and Gamow-Teller matrix elements $\left|<\Psi_{J_f}|| \sum_{i=1}^{A} \frac{1}{2^{1/2}}\tau_i^+ || \Psi_{J_i}>\right|^2$ and

$\left|<\Psi_{J_f}|| \sum_{i=1}^{A} \frac{1}{2^{1/2}}\tau_i^+ g_i || \Psi_{J_i}>\right|^2$. τ_i^+ is the raising operator for the z component of isotopic spin of the ith nucleon and g_i is the Dirac matrix operating on the spin wave function of the ith nucleon. In the

case of the B^{12} and N^{12} decays, the selections rules $\Delta J = 0$ $\Delta T = 0$ cause the Fermi matrix element to vanish so the decays are pure Gamow-Teller transitions and equation 1 becomes:

$$ft = \frac{\text{const}}{|\int \sigma|^2} \tag{4}$$

Equation 4 is actually an approximate expression good to zeroth order in the quantities (kR) and (v/c) where k is the beta particle wave number, R is the nuclear radius, and v is the average velocity of the nucleon in the nucleus. A small correction factor is introduced when terms of second order in these quantities are taken into account. Terms of first order vanish for an allowed decay because they involve a nuclear parity change. The second order terms are called second forbidden terms and involve the nuclear matrix elements $|\int \sigma r^2|^2$, $|\int \sigma \cdot \mathbf{r}\, \mathbf{r}|^2$, $|\int \gamma_5 \mathbf{r}|^2$, and $|\int \sigma \times \mathbf{r}|^2$. The effect of these second forbidden terms has been worked out by Morita[11]. To use his results, we must replace f in equation 4 by $f_{corr.}$ where $f_{corr.}$ is given by:

$$f_{corr.} = \frac{c^3}{(mc^2)^5} \int_0^{P_o} P^2 (E-E_o)^2 F(z, E) C(z, E)\, dP \tag{5}$$

and C(z, E) is the function defined by Morita. C(z, E) is close to unity, the difference 1 - C(z, E) being of the order of 0.01, and in the case of the N^{12} and B^{12} decays the values of $f_{corr.}$ calculated from equation 5 differ by only a per cent or so from the uncorrected f values calculated from equation 2. Therefore, although Morita points out that the quantity 1 - C(z, E) may be in error by a few tens of per cent due to approximations used in evaluating the nuclear matrix elements, this fact

need cause us no concern.

Internal bremsstrahlung corrections to allowed beta spectra have been worked out by Schwarzchild[12] and by Gell-Mann and Berman[13]. The magnitude of this correction to the allowed spectrum shape function $S(E, E_o)$ depends on the beta particle energy E and the end point energy E_o. We can write the corrected shape function as $S(E, E_o)\ (1-C(E, E_o))$ and the function $C(E, E_o)$ has been tabulated by Schwarzchild[12]. Using his table, we have estimated by numerical integration that the ft values for N^{12} and B^{12} are changed by less than 1% and that the ratio $ft(N^{12})/ft(B^{12})$ is changed by less than 0.5% if the internal bremsstrahlung correction is included. We will therefore neglect this correction in calculating ft values.

III. EXPERIMENTAL PROCEDURE

The procedure followed in measuring the half-lives of N^{12} and B^{12} was to create a certain initial amount of activity and to measure the beta particle counts from this activity as a function of time elapsed. Because of the short half-lives of N^{12} and B^{12}, this procedure had to be repeated many times in order to obtain sufficient statistical precision for the points on the decay curve. This was accomplished by producing the N^{12} or B^{12} activity in a nuclear reaction, and using a pulsed beam. A certain amount of activity was produced by each beam pulse, and in the interval between beam pulses beta particle counts were recorded as a function of time.

We can summarize the necessary pieces of experimental equipment as follows: (1) a target in which the N^{12} or B^{12} activity is produced by bombardment with a beam of charged particles, (2) a counter to detect the beta particles, (3) a device for chopping the beam to produce equally spaced beam pulses of a fixed duration, (4) an accurate and stable electronic "clock," (5) a multi-channel device controlled by this "clock" which records beta particle counts as a function of time elapsed since the end of a beam pulse. The various parts of the experimental arrangement will now be discussed in more detail.

A. Targets

The B^{12} and N^{12} activities were made in the reactions $B^{11}(d,p)B^{12}$ and $B^{10}(He^3,n)N^{12}$. The D^2 and He^3 beams were furnished by the 3 Mev electrostatic accelerator at the Kellogg Radiation

Laboratory. To single out the desired mass component at a particular energy, the beam was passed through a cross-field magnet and a 90° magnetic analyzer. For the measurement of the N^{12} half-life, thick targets of natural boron (81% B^{11}, 19% B^{10}) and enriched B^{10} (4% B^{11}, 96% B^{10}) were used. These targets were prepared by thermally cracking diborane onto 3/4 in. diameter tungsten blanks. This procedure has been described in detail by Overley[14]. The thickness of these targets was estimated to be 0.5 milligrams/cm^2 on the basis of the residual hydrogen pressure left after the completion of the cracking process. A thin target, 0.05 milligrams/cm^2, was used in the measurement of the B^{12} half-life since the yield from the $B^{11}(d, p)B^{12}$ reaction is much greater than the yield from the $B^{10}(He^3, n)N^{12}$ reaction. This target was made by vacuum evaporation of natural boron onto a tantalum backing and was obtained from R. W. Kavanagh.

B. Beta Particle Counter and Target Chamber

The beta particles from the decay of B^{12} and N^{12} were detected in a 1-1/2 in. diameter x 3/8 in. thick anthracene crystal mounted on the face of a photomultiplier tube. The crystal was mounted outside the target chamber at a distance of 3/4 in. from the target as shown in fig. 1. An aluminum wall 0.15 in. thick separated it from the target and stopped beta particles with energies less than 2 Mev from reaching the crystal. This reduced considerably the number of background counts from other beta emitting nuclei produced in the target along with the N^{12} or B^{12} (particularly C^{11} and N^{13} for which the beta end

point energies are less than 2 Mev). The walls of the target chamber were kept thin in order to minimize scattering and bremsstrahlung effects which would impair the sharpness of the beta peak.

The end point energies for the N^{12} and B^{12} decays to the C^{12} ground state are 16.43 Mev[15] and 13.369 Mev[16]. The anthracene crystal was 2 Mev thick for high velocity beta particles, and since the majority of the beta particles from N^{12} and B^{12} have energies well above 2 Mev, the pulse height spectra obtained with the anthracene crystal showed a well-defined peak. A typical spectrum is illustrated in fig. 2.

C. Beam Chopper

Since the half-lives of N^{12} and B^{12} are about 10 and 20 milliseconds, a pulsed beam technique must be used to measure them. Beam pulses of 10 to 20 milliseconds duration spaced at least 200 milliseconds apart were needed so that the half-life measurements could be extended over several half-lives.

Several methods of chopping the beam were considered. In order to avoid the extra background which might result if the beam were chopped by merely defocusing it or placing an obstacle in its path, we decided to chop the beam by turning off the R.F. ion source. This can be accomplished by applying a negative voltage of several hundred volts to the grid of the R.F. oscillator. A 60 cycle chopper operating on this principle had already been installed in the dome of the 3 Mev electrostatic accelerator, and has been described by Michel[17]. This chopper applies the 60 cycle voltage from the pancake generator directly to the

R. F. grid and produces beam pulses of 8 milliseconds duration spaced 8 milliseconds apart.

For the present experiment, a chopper was installed which makes use of a cam driven by a 300 rpm motor to open and close a micro-switch. The cam is designed so that the switch is closed for 20 milliseconds and open for 180 milliseconds. The open position of the switch connects the R. F. oscillator grid to a 340 volt negative power supply, and the closed position of the switch connects it to a 20 volt positive supply. It was found that turning on the ion source by switching to a point slightly positive rather than to ground sharpened the front edge of the beam pulse. The beam chopper just described will be referred to subsequently as the 5 cycle chopper to distinguish it from the 60 cycle chopper which was also used in our experiment.

At the base of the column of the 3 Mev electrostatic accelerator, the beam passes through an aperture in a plate which is insulated from the rest of the column. When the accelerator is operated with a pulsed beam, this plate picks up a signal which can be used to synchronize the operation of gating and control circuits with the beam pulses. The signal consists of rectangular pulses whose duration corresponds to the duration of a beam pulse (see figs. 4 and 6).

D. Timer

An essential piece of equipment for a half-life measurement is an accurate and very stable "clock." A block diagram of the electronic timer used in our experiment is shown in fig. 3. The circuit has four main parts: a crystal controlled oscillator with an output frequency of

100.000 kc (manufacturer's specification), a frequency dividing circuit designed to reduce this frequency by a factor of 10, a series of six scales of ten, and a simple pulse shaping circuit. A crystal controlled oscillator is used because of the characteristic frequency stability of such oscillators. The frequency dividing circuit reduces the frequency of the oscillator to 10 kc so that it can be handled by the scalers. The scalers are Dekatron glow transfer tubes (Baird-Atomic Inc.), which have a complete scale of ten built into a single tube. They are connected in series and a multi-position switch makes it possible to take the output from any one of the six Dekatrons. The output from one of the Dekatrons is a series of evenly spaced pulses 100 volts positive in magnitude and 100 microseconds in duration. The spacing of the pulses can be varied from 1 millisecond to 100 seconds in powers of 10 by changing the position of the switch and taking the output from different Dekatrons in the series. The pulse shaping circuit is included because the original pulses from a Dekatron are not suitable for operation of the RIDL 400 channel analyzer in the time analyzer mode. This requires negative pulses 20 volts in magnitude and 2 microseconds in duration. The pulse shaping circuit differentiates the Dekatron pulse, producing a negative signal and a positive signal, each of 2 μseconds duration. The negative pulse is clipped and the positive pulse, corresponding to the front edge of the original Dekatron pulse, is then inverted and attenuated to 20 volts.

E. Operation of RIDL 400 Channel Analyzer in Time Mode.

The RIDL 400 channel analyzer, in the time mode, operates as

a multi-channel scaler which records counts as a function of time. It thus combines the functions of a time to pulse height converter and a conventional pulse height analyzer, and is ideal for use in radioactive decay studies. The analyzer has three inputs relevant to operation in the time mode: the detector input, the detector gate input, and the oscillator input. The pulses to be counted, which must be negative pulses 20 volts in magnitude and 2 microseconds in duration, are fed into the detector input. The detector gate input gates the detector input "on" when it is open or at ground potential and "off" when it is at -20 volts. The timing pulses, which must also be 20 volts negative in magnitude and 2 microseconds in duration, are fed into the oscillator input and serve to calibrate the base line of the analyzer in terms of time elapsed per channel. With a source of pulses to be counted connected to the detector input, the detector gate input gated "on," and a source of timing pulses connected to the oscillator input, the operation of the analyzer proceeds as follows. The analyzer stores the counts from pulses fed into the detector input in one channel until it receives a pulse from the oscillator input which advances the address one channel. Counts from pulses occurring in the next time interval are then stored in this channel until another pulse is received from the oscillator input, etc.

Unfortunately, one feature is not provided in the present design of the analyzer which was needed for our experiment. This is an input into which a pulse can be fed to reset the address of the analyzer to channel zero. To provide this, an additional input was connected to the same point as the manual "reset address" button on the front apron

of the analyzer. The address could be reset to channel zero by application of a 20 volt negative pulse to this input.

F. Circuitry and Procedure for Taking Data

The first step in making a half-life measurement was to obtain the spectrum produced by the beta particles from N^{12} or B^{12} in the anthracene crystal. The circuit arrangement for obtaining this spectrum is shown in fig. 4. The 60 cycle chopper was used to produce beam pulses of 8 milliseconds duration spaced 8 milliseconds apart. The beam signal taken off the plate at the bottom of the accelerator column (see section C) was fed into an amplifier and gate generator designed by R. W. Kavanagh. This gate generator was set to give a gate signal occurring 1 millisecond after the end of a beam pulse and lasting for 6 milliseconds or until 1 millisecond before the start of the next beam pulse. The gate signal was amplified to + 300 volts and used to gate the phototube "on." (See fig. 5 for circuitry associated with phototube gate.) The output from the phototube and pre-amplifier was fed into a 10-T-2 amplifier and then into the RIDL 400 channel analyzer operated in the pulse height analyzer mode. A typical beta spectrum is shown in fig. 2.

Fig. 6 shows the circuitry used in making the actual half-life measurements. The 400 channel analyzer was operated in the time mode as described in section E. The output from the 10-T-2 was fed into an integral discriminator biased to correspond to about channel 60 in the spectrum of fig. 2. The negative pulses from this discriminator were fed into the detector input of the 400 channel analyzer. The

timer described in section D was set to produce pulses at 1 millisecond intervals and these were applied to the oscillator input of the analyzer. The beam was chopped with the 5 cycle chopper, and the beam signal again fed into the amplifier and gate generator described previously. The gate signal, occurring 1 millisecond after the end of a beam pulse and lasting for six milliseconds, was used in this case to generate an address reset signal to reset the address of the analyzer to channel zero. The box labeled "address reset" in fig. 6 differentiated the front edge of the gate signal to produce a negative pulse 1 millisecond after the end of each beam pulse. A diagram of this circuit is included in fig. 7. The box marked "D.C. gate" in fig. 6 is a bi-stable circuit. It was connected to the address reset output by a switch which enabled the output to be applied to either half of the bi-stable. Changing the switch from one position to another turned the gate "on" or "off" in coincidence with the next address reset pulse which occurred. A diagram of the D. C. gate circuit is shown in fig. 7.

We now describe the sequence of operations followed in making a half-life measurement. We start with the timer on, the beam on, and the D. C. gate "off," so that the address is being advanced every millisecond and reset about every 200 milliseconds but no counts are being recorded. We then turn the switch on the D. C. gate to the "on" position. One millisecond after the next beam pulse ends, the address is reset to channel zero and the D. C. gate is simultaneously turned "on." The 400 channel analyzer begins to record counts as a function of time, tracing out the exponential decay curve on its oscilloscope

screen. At about channel 180, the next beam pulse occurs and the next 20 channels record counts with the beam on. At about channel 200, this beam pulse ends; one millisecond later, the address is reset to channel zero and the cycle repeats. To end the measurement, after the desired statistical accuracy has been obtained for the decay curve, we turn the D.C. gate switch to the "off" position, disconnect the address reset signal, and turn off the timer. A typical curve of counts vs. time plotted in cartesian coordinates is shown in fig. 8.

It was necessary to take some care to avoid saturation in the first few channels due to high counting rates. The counting rates were controlled by varying the beam intensity and energy. For the N^{12} measurement, with the thick enriched B^{10} target described in section A, a beam energy of 2.5 Mev, and an average beam current of 0.1 to 0.2 microamperes the counting rate in channel 1 was 2000 counts/sec. For the B^{12} measurement, with the thin natural boron target, a beam energy of 1 Mev, and an average beam current of 0.02 microamperes, the counting rate in channel 1 was about 4000 counts/sec. Since the approximate duration of a pulse was 2 microseconds, the dead time was estimated to be 0.8% in channel 1 for the B^{12} measurement and 0.4% in channel 1 for the N^{12} measurement. The effect of a small amount of dead time on a half-life measurement is considered in more detail in the next section.

The effectiveness of the 5 cycle beam chopper was checked by bombarding a F^{19} target with a chopped proton beam of 900 kev and observing the prompt gamma rays. The beam on the target fell from its maximum value to less than 0.0025% of its maximum value in a time less than one millisecond.

IV. DATA ANALYSIS

A. B^{12} Half-life

Since the considerations involved in the analysis of the B^{12} and N^{12} data are somewhat different, we will consider each separately. We start with a set of experimental numbers n_i, $i = 0, 1, \ldots, m$, where n_i = number of counts recorded in the time interval $t_i \leq t \leq t_{i+1}$ and $t_{i+1} - t_i = 1$ msec. The expression for the number of decays $n(t)\Delta t$ occurring in the time interval t to $t + \Delta t$ is given by:

$$n(t)\Delta t = n(t_o)\Delta t \exp[-\lambda(t-t_o)] \tag{1}$$

$$\ln(n(t)\Delta t) = \ln(n(t_o)\Delta t) - \lambda(t-t_o) \tag{2}$$

where $n(t_o)\Delta t$ is the number of decays which occurred in the time interval t_o to $t_o + \Delta t$. In equation 1, λ is a constant and the half-life for the decay, $t_{1/2}$, is related to λ by $t_{1/2} = \ln 2/\lambda$.

The standard procedure for determining λ, or equivalently $t_{1/2}$, from the set of experimental points n_i, is to fit this set of points by least squares to the expression given in equation 2. This procedure involves finding the values of λ and $(n(t_o)\Delta t)$ which minimize the value of the sum $\sum_{i=0}^{m} \dfrac{[\ln n_i - (\ln n(t_o)\Delta t - \lambda(t_i - t_o))]^2}{\sigma^2_{\ln n_i}}$, and is discussed in any standard text on statistical methods. The Burroughs 220 Computer was programed to perform the least squares analyses. Since the standard deviation in n_i is $(n_i)^{1/2}$, the standard deviation in $\ln n_i$, which we have designated by $\sigma_{\ln n_i}$ above, is approximately

given by $\sigma_{\ln n_i} = \ln (n_i + n_i^{1/2}) - \ln n_i \approx \frac{1}{n_i^{1/2}}$. This approximation was used in the program, and is good for $n_i >> 1$.

Equation 2 predicts that a plot of $\ln n_i$ vs. t should appear as a straight line. Such a plot for the B^{12} decay is shown in fig. 9. In practice, experimental factors can cause the plot to deviate from a straight line and change its apparent slope, $-\lambda$, from the true value introducing error into the half-life measurement. The possible sources of error relevant to the B^{12} measurement are:

(1) Background counts due to events other than the decay of the nucleus being studied. These arise from the presence of other radioactive nuclei and from the constant background level from the crystal and phototube.

(2) Loss of counts due to dead time.

(3) Variation in phototube gain with counting rate. At high counting rates additional currents are drawn between the phototube dynodes which change their biases, causing a change in the phototube gain.

In the discussion which follows, the above sources of error will often be referred to by the numbers (1), (2), and (3).

The linearity of the plot in fig. 9 is a good test of whether the above sources of error are small or not. A good test for linearity is to fit different sections by least squares and see if the same value for the slope, $-\lambda$, is obtained for the different sections. Qualitatively, we may expect the presence of a constant background per channel, n_b, to flatten out the last portion of the plot in fig. 9. Loss of counts due

to dead time will tend to flatten out the first portion of the plot. A change in phototube gain with counting rate will also affect most seriously the first portion of the plot where the counting rates are high. Gain change may make this region either flatter or steeper depending on the manner in which the gain changes. In other words, we may expect the slope of the central portion of the plot in fig. 9 to be closest to the true slope with the sources of experimental error (1), (2), and (3), showing up at the extreme ends.

We have divided fig. 9 up into three sections, (a), (b), and (c), as indicated in the figure. Section (a) includes channels 1 to 20, section (b) includes channels 20 to 130, and section (c) includes channels 130 to 150. The three values for the half-life obtained by making least squares fits to the three sections are $t_{1/2}(a) = 20.30 \pm 0.1$ msec, $t_{1/2}(b) = 20.40 \pm 0.03$ msec, and $t_{1/2}(c) = 20.70 \pm 1.0$ msec. The closeness of these three values, which agree within their standard deviations, is a good indication that the experimental errors (1), (2), and (3) are small, and that $t_{1/2}(b)$ is a good approximation to the true value of the half-life, $t_{1/2}$. We will now discuss the corrections to $t_{1/2}(b)$ for errors (1), (2), and (3).

(1) Background Correction. Table 2 shows the half-lives and maximum beta particle energies for all beta emitters which can be produced by deuteron bombardment of the isotopes of boron and likely target contaminants. The contaminants considered are carbon, nitrogen, oxygen, and silicon. The table shows that it is not possible to produce any beta emitter with a half-life less than 200 times the half-life of B^{12}.

Table 2

Half-lives and Beta End Point Energies for Beta Emitters Which Can Be Produced By Deuteron Bombardment of the Isotopes of Boron, Carbon, Nitrogen, Oxygen, and Silicon

(Taken from the Compilations of Lauritsen and Ajzenberg-Selove[18] and Endt and Braams[19])

Nuclide	Reaction	Half-life	E_β(max)
B^{12}	$B^{11}(d, p)B^{12}$	20.3 msec	13.40 Mev
C^{11}	$B^{10}(d, n)C^{11}$	20 min	968 kev
C^{14}	$C^{13}(d, p)C^{14}$	5568 years	156 kev
N^{13}	$C^{12}(d, n)N^{13}$	10 min	1.2 Mev
O^{15}	$N^{14}(d, n)O^{15}$	123 sec	1.72 Mev
N^{16}	$N^{15}(d, p)N^{16}$	7.3 sec	10.3 Mev
F^{17}	$O^{16}(d, n)F^{17}$	66 sec	1.75 Mev
F^{18}	$O^{17}(d, n)F^{18}$	112 min	649 kev
O^{19}	$O^{18}(d, p)O^{19}$	29 sec	4.5 Mev
P^{29}	$Si^{28}(d, n)P^{29}$	4.6 sec	3.94 Mev
P^{30}	$Si^{29}(d, n)P^{30}$	2.5 min	3.24 Mev
Si^{31}	$Si^{30}(d, p)Si^{31}$	157 min	1.47 Mev

We can therefore treat any background present in fig. 9 as constant in time. We designate the number of background counts/channel in fig. 9 by n_b.

The most straightforward way to determine n_b would have been to extend the decay curve of fig. 9 for several more half-lives. The curve would eventually level off at a constant height equal to n_b when the B^{12} activity became negligible. It was not possible to do this without modifying the beam chopper to give a longer counting cycle (400 msec instead of 200 msec), and it was not deemed worthwhile to make such a major modification, since we will now show that the correction to $t_{1/2}(b)$ for n_b is small in any case.

In appendix I, formulas are derived which give the per cent change introduced in a half-life measurement by a constant background when the half-life is determined by making a least squares fit to the experimental points. The per cent change is just $[(t'_{1/2} - t_{1/2})/t^{1/2}] \times 100$ where $t_{1/2}$ is the true value of the half-life and $t'_{1/2}$ is the apparent value with a constant background n_b present. We can now use the value of $t_{1/2}(c)$ obtained by fitting the last 20 points of fig. 9 together with equation 16 of appendix I to estimate n_b (assuming $t_{1/2}(b)$ is close to the true value $t_{1/2}$). We have $[t_{1/2}(c) - t_{1/2}(b)]/t_{1/2}(b) = (0.3 \pm 1.0)/20.4$ hence $n_b = 8 \pm 26$ counts/channel. Since n_b cannot be negative, the actual limits on n_b are 0 to 34 counts/channel; we will therefore take the estimate $n_b = 17 \pm 17$ counts/channel.

The correction to $t_{1/2}(b)$ is accomplished by subtracting n_b from each of the points in region (b) of fig. 9 and repeating the least squares fit. This gives a correction of -0.08 ± 0.08 msec., con-

firming our previous statement that the effect of the background correction is small. Alternatively, we can determine the correction using equation 18 of appendix I, which gives the same result. A plot of fig. 9 corrected for background is not shown because the correction is too small to show up on the scale to which fig. 9 is drawn.

(2) Dead time correction. The fraction of counts $\Delta n_i/n_i$ lost due to dead time in channel i of fig. 9 is proportional to the number of counts in channel i, n_i. In the notation of appendix I, $\Delta n_i/n_i = c_d n_i$ where c_d is the same for all channels. If the counting rate in channel i is constant in time, which will be the case if the same amount of B^{12} activity is made by each beam pulse, we can write $\Delta n_i/n_i = rn_i/T$ where T is the total counting time/channel and r is the duration of a beta pulse. The total time for the measurement in fig. 9 was 3000 sec., so $T = 3000/200 = 15$ sec. The duration of a beta pulse, r, was 2 μsec., so for channel 1 $\Delta n_1/n_1 = 0.008$ and for channel 20 $\Delta n_{20}/n_{20} = c_d n_{20} = 0.004$. Using formula 19 of appendix I, the correction to $t_{1/2}(b)$ for dead time is - 0.02 msec.

It can easily be shown that if the counting rate in channel i is not constant, $\Delta n_i/n_i > rn_i/T$ in which case the dead time correction will be increased. Later on in this section, we will use the value of $t_{1/2}(a)$ (1st 20 channels of fig. 9) as a check on this possibility.

(3) Correction for gain change of phototube with counting rate. In fig. 10, the spectrum of beta particles from B^{12} is shown for three different counting rates: 5000 counts/sec., 750 counts/sec., and 100 counts/sec. The different counting rates were obtained by varying

the beam intensity and energy. There is no apparent change in the position or shape of the beta peak. We estimate that a 5% change in the position of the peak could easily be detected from fig. 10, and therefore assume that the phototube gain changes by less than 5% when the counting rate is varied from zero to 5000 counts/sec.

In appendix II, the effect of a gain change which is linear with counting rate on a decay curve such as fig. 9 is investigated. The gain in channel i is written as $G_i = G(1 + \epsilon n_i)$ where G is the gain at zero counting rate, n_i is the number of counts in channel i of fig. 9, and ϵ is a constant. Since the counting rate in channel 1 is 4000 counts/sec., the discussion in the preceding paragraph shows that $\epsilon n_1 = 0 \pm 0.04$. If we now use equation 1 of appendix II and equation 19 of appendix I, the correction to $t_{1/2}(b)$ for gain change of the phototube is 0 ± 0.03 msec.

We now recall that $t_{1/2}(b)$, our uncorrected experimental value for the half-life, is 20.40 ± 0.03 msec., and summarize corrections (1), (2), and (3):

(1) Background correction . . . . . - 0.08 ± 0.08 msec.

(2) Dead time correction . . . . . - 0.02 msec.

(3) Phototube gain change . . . . . 0 ± 0.03 msec.

We have also estimated the combined magnitude of corrections (2) and (3) by comparing $t_{1/2}(a)$ (1st 20 channels of fig. 9) with the value of $t_{1/2}(b)$ corrected only for background, and using equations 17 and 19 of appendix I. The result is (2) + (3) = 0.01 ± 0.04 msec., and serves as a check that our estimates of corrections (2) and (3) are reasonable.

We take as our final corrected value for the B^{12} half-life $t_{1/2}$ = 20.30 ± 0.1 msec.

B. The N^{12} Half-life

Fig. 11 shows a plot of $\ln n_i$ vs. t for the N^{12} decay. The same sources of experimental error must be considered in the analysis, and the treatment is the same as for B^{12} except for the background correction. An additional source of error must be considered, since nitrogen is normally a gas. It is necessary to show that N^{12} cannot escape from the target at a rate sufficient to affect a half-life measurement significantly. We will designate this additional source of error by (4), and continue to use the labels (1), (2), and (3) to refer to corrections for background, dead time, and gain change of the phototube.

(1) Background Correction. Table 3 shows the half-lives and maximum beta particle energies of the beta-unstable nuclides which can be made when the isotopes of boron and likely target contaminants are bombarded by He^3 ions. The table shows that any background from these may be treated as constant, since all have half-lives more than 150 times longer than N^{12}. We again designate the constant background/channel in fig. 11 by n_b. In this case, we can determine n_b by averaging the counts in the channels above 140 in fig. 11, since the N^{12} activity is almost negligible by this time. We obtain n_b = 20 ± 2 counts/channel after making allowance for the small amount of N^{12} activity remaining (4 counts/channel in channel 140).

An additional background source is present in fig. 11, however,

Table 3

Half-lives and Beta End Point Energies For Beta Emitters Which Can Be Made By He^3 Bombardment of the Isotopes of Boron, Carbon, Nitrogen, Oxygen, and Silicon

(Taken from the Compilations of Lauritsen and Ajzenberg-Selove[18] and Endt and Braams[19])

Nuclide	Reaction	Half-life	E_β(max)
N^{12}	$B^{10}(He^3, n)N^{12}$	11 msec	16.6 Mev
C^{11}	$B^{10}(He^3, d)C^{11}$	20 min	968 kev
N^{13}	$B^{11}(He^3, n)N^{13}$	10 min	1.2 Mev
O^{14}	$C^{12}(He^3, n)O^{14}$	72 sec	1.8 Mev
F^{17}	$N^{15}(He^3, n)F^{17}$	66 sec	1.75 Mev
Ne^{18}	$O^{16}(He^3, n)Ne^{18}$	1.6 sec	3.2 Mev
Ne^{19}	$O^{17}(He^3, n)Ne^{19}$	17.4 sec	2.18 Mev
Si^{27}	$Si^{28}(He^3, He^4)Si^{27}$	4.5 sec	3.5 Mev
P^{30}	$Si^{28}(He^3, p)P^{30}$	2.5 min	3.24 Mev
S^{31}	$Si^{29}(He^3, n)S^{31}$	2.6 sec	3.85 Mev

since the presence of a small HD contamination in the He^3 beam will produce B^{12} from the B^{11} in the target. A very small contamination of HD can still cause trouble since the cross section for the reaction $B^{11}(d,p)B^{12}$ is so much larger than the cross section for the reaction $B^{10}(He^3,n)N^{12}$.

The measurement in fig. 11 was made with an enriched B^{10} target (96% B^{10}, 4% B^{11}). Fig. 12 shows a similar measurement taken immediately following the one in fig. 11 in which a natural boron target (81% B^{11}, 19% B^{10}) was used. The only difference in the two measurements is that the ratio of B^{11} to B^{10} is increased by a factor of 87 when the natural boron target is used, and the initial ratio of B^{12} activity to N^{12} activity is therefore 87 times greater in fig. 12 than in fig. 11. Because of this fact, there is a noticeable curvature in fig. 12 after about 30 or 40 channels.

We now wish to determine the initial ratio of B^{12} activity to N^{12} activity for fig. 12 and use this information to correct fig. 11 for the presence of B^{12}. We assume that the only activities present in fig. 12 are B^{12} and N^{12}, and the shape of fig. 12 then depends on three things: the initial ratio B^{12}/N^{12} and the two half-lives $t_{1/2}(B^{12})$ and $t_{1/2}(N^{12})$. From section IV A we know $t_{1/2}(B^{12}) = 20.3$ msec. We take $t_{1/2}(N^{12})$ from a preliminary fit of points 11 to 90 of fig. 11, corrected for the constant background n_b which we already know. This gives $t_{1/2}(N^{12}) = 11$ msec., and is a good enough estimate for the present purpose.

We can now determine the initial ratio B^{12}/N^{12} for fig. 12 by

the following procedure. We assume some value for this ratio $(B^{12}/N^{12})_a$ and use the value of $t_{1/2}(N^{12})$ to subtract out from fig. 12 all the N^{12} activity. The remaining counts are then fitted by least squares to give a value for the B^{12} half-life, $t_{1/2}(B^{12})_a$. Using different assumptions for $(B^{12}/N^{12})_a$, we can plot a curve of $t_{1/2}(B^{12})_a$ vs. $(B^{12}/N^{12})_a$, and this has been done in fig. 13. We can then use the known value of 20.3 msec. for the B^{12} half-life to determine the true value of (B^{12}/N^{12}) from this curve. From fig. 13, $B^{12}/N^{12} = 0.50 \pm 0.07$ for fig. 12 and the corresponding value for the initial ratio B^{12}/N^{12} for fig. 11 is 0.0057 ± 0.0008. We can now correct fig. 11 for the presence of B^{12}. A plot of fig. 11, corrected for B^{12} background and the constant background n_b, is shown in fig. 14.

As we did in the case of fig. 9, we now divide fig. 14 into three sections: (a) channels 1 to 10, (b) channels 11 to 90, and (c) channels 90 to 110. The three values of $t_{1/2}$ obtained by fitting the three sections are $t_{1/2}(a) = 10.95 \pm 0.13$ msec, $t_{1/2}(b) = 10.95 \pm 0.02$ msec., and $t_{1/2}(c) = 11.82 \pm 1.1$ msec. Since fig. 14 is already corrected for background, we will use $t_{1/2}(c)$ not to determine the background correction as we did in the case of fig. 9 but as a consistency check on the correction we have already made. We take $t_{1/2}(b)$ as our experimental value for the N^{12} half-life corrected for background.

In addition to the statistical uncertainty in $t_{1/2}(b)$ an uncertainty of ± 0.015 msec. is introduced due to the uncertainty in n_b. (This can be calculated using equation 18 of appendix I.) The correction for B^{12} changes the value of $t_{1/2}(b)$ by 0.05 msec. (i.e., $t_{1/2}(b) = 11.0$ msec. without this correction). Assuming that this correction depends

linearly on the initial ratio B^{12}/N^{12}, an uncertainty of ±0.008 msec. is introduced in $t_{1/2}(b)$ due to the uncertainty in B^{12}/N^{12}. The total uncertainty introduced in $t_{1/2}(b)$ by the background correction is then ± 0.017 msec.

A comparison of $t_{1/2}(b)$ and $t_{1/2}(c)$ indicates that the above figure should probably be increased. Although $t_{1/2}(b)$ and $t_{1/2}(c)$ do agree with each other within their standard deviations, in order to bring them into exact agreement it is necessary to assume that either n_b should be increased by 5 counts/channel or that B^{12}/N^{12} should be increased by 0.03. The first would change the value of $t_{1/2}(b)$ by 0.04 msec., the second would change the value of $t_{1/2}(b)$ by 0.025 msec. We have therefore allowed an uncertainty of ±0.04 msec. due to the background correction, since the comparison of $t_{1/2}(b)$ and $t_{1/2}(c)$ indicates a good probability that our previous estimate of ± 0.017 msec. is too small.

(2) and (3). Dead time and phototube gain change corrections. The procedure for estimating these corrections is identical to that described in section IV A on the B^{12} half-life measurement. The counting rate in channel 1 of fig. 14 is 2000 counts/sec., which leads to a correction of - 0.005 msec. to $t_{1/2}(b)$ for (2) and a correction of 0 ± 0.007 msec. to $t_{1/2}(b)$ for (3). Both corrections should thus be negligible.

We have also estimated the combined effect of both (2) and (3) by comparing $t_{1/2}(a)$ with $t_{1/2}(b)$ as described in section A for the B^{12} case. Using equations 17 and 19 of appendix I gives (2) + (3) = 0 ± 0.04 msec., supporting the conclusion that corrections (2) and (3) are negli-

gible.

(4) Loss of nitrogen from the target. To check the rate at which nitrogen could escape from the target, the N^{13} half-life was measured under conditions identical to the N^{12} measurement. The N^{13} activity was made in the reaction $B^{11}(He^3, n)N^{13}$. The value obtained for the half-life was $t_{1/2} = 10 \pm 1$ min. as compared with the accepted value of 10.05 min.[18] Since loss of nitrogen from the target reduces the measured value of the N^{13} half-life by less than 10%, this source of error should be completely negligible in our measurement of the N^{12} half-life, which is 50,000 times shorter.

We recall that the value of $t_{1/2}(b)$, in which the background correction is already included, is 10.95 ± 0.02 msec., and summarize the results of the preceding discussion as follows:

(1) Uncertainty in background correction . . . . . ± 0.04 msec.

(2) Dead time correction . . . . . negligible

(3) Correction for change in phototube gain with counting rate . . . . . negligible

(4) Loss of nitrogen from target . . . . . negligible

We therefore take as our final experimental value for the N^{12} half-life, $t_{1/2} = 10.95 \pm 0.05$ msec.

C. Calculation of ft values

The calculated ft values for the decay of N^{12} and B^{12} to the C^{12} ground state are given in table 4. The table also shows the value and the reference for each experimental quantity used in the calculation. f values were calculated by numerical integration using the definition of f given by equation 2 and 3 of section II. The tables of the National

Bureau of Standards[10] were used for $F(z, E)$. We have checked our f values with an independent calculation by Michel[17], and our f values agree with his to better than 0.5%. We have also included the small effect of second forbidden terms, and calculated values of $f_{corr.}$ using equation 5 of section II. These are given in table 4. The difference between f and $f_{corr.}$ is almost negligible.

Table 4

Experimental Data Used in the Calculation of ft Values for the Decays of B^{12} and N^{12} to the C^{12} Ground State

			Reference
B^{12}	Half-life	20.30 ± 0.1 msec	Present Experiment
	E_β(max)	13.369 ± 0.001 Mev	(16)
	Branch to 4.4 Mev state of C^{12}	1.3 ± 0.1 %	(21)
	Branch to 7.65 Mev state of C^{12}	1.3 ± 0.4 %	(22)
	Branch to 10.1 Mev state of C^{12}	0.13 ± 0.04 %	(22)
N^{12}	Half-life	10.95 ± 0.05 msec	Present Experiment
	E_β(max)	16.43 ± 0.06 Mev	(15)
	Branch to 4.4 Mev state of C^{12}	2.4 ± 0.2 %	(21)
	Branch to 7.65 Mev state of C^{12}	3.0 ± 0.4 %	(17)
	Branch to 10.1 Mev state of C^{12}	Unknown	

For the ground state decays: $ft(N^{12}) = (1.33 \pm 0.027) \times 10^4$

$ft(B^{12}) = (1.17 \pm 0.012) \times 10^4$

$ft(N^{12})/ft(B^{12}) = 1.14 \pm 0.025$

$f_{corr.}\, t(N^{12})/f_{corr.}\, t(B^{12}) = 1.15 \pm 0.025$

V. DISCUSSION

Our final values for the half-lives of B^{12} and N^{12}, $t_{1/2}(B^{12}) = 20.3 \pm 0.1$ msec. and $t_{1/2}(N^{12}) = 10.95 \pm 0.05$ msec., are in very good agreement with the two most recent measurements by Farmer and Class[6] and by Peterson and Glass[7] which are given in table 1. In our opinion, these half-lives are now well-known.

From table 4, the ratio of ft values for the decays of N^{12} and B^{12} to the C^{12} ground state is $ft(N^{12})/ft(B^{12}) = 1.14 \pm 0.025$. (Inclusion of the second forbidden terms as discussed in section II gives 1.15 for this ratio.) This ratio has been calculated using the most recent available data, and it does not appear possible that the difference of 14% in the two ft values can be due to experimental errors. We must then explain a 14% difference in the nuclear matrix elements $|\int \sigma|^2(B^{12})/|\int \sigma|^2(N^{12}) = 1.14$.

If one believes in the mirror nucleus picture, a difference in these matrix elements can be due only to coulomb effects since aside from such effects the ground state wave functions of N^{12} and B^{12} must be identical. One would therefore hope to explain the 14% difference in the nuclear matrix elements by introducing coulomb effects. An attempt to do this is currently being made at this laboratory by Bahcall and Michel. The model upon which their calculation is based is simple, and accounts qualitatively for the fact that $|\int \sigma|^2(B^{12})$ is greater than $|\int \sigma|^2(N^{12})$. Quantitative results from the calculation are not yet available.

The model for the calculation is illustrated below:

B^{12} decay $\quad B^{11} + n \rightarrow B^{11} + p$

N^{12} decay $\quad C^{11} + p \rightarrow C^{11} + n$

It is assumed that in each case we have an inert core with an extra nucleon bound to it by some potential, and that it is this extra nucleon which undergoes the beta decay. For the B^{12} decay, the overlap integral between the initial and final states is $\int \Psi_p^*(B^{11})\Psi_n(B^{11})\, d\tau$ where $\Psi_n(B^{11})$ is the wave function of a neutron bound in the potential of the B^{11} core, $\Psi_p(B^{11})$ is the wave function of a proton bound in the potential of the B^{11} core, and $d\tau$ signifies an integration over the nucleon coordinates. Correspondingly, the overlap integral for the N^{12} decay is $\int \Psi_n^*(C^{11})\Psi_p(C^{11})\, d\tau$.

We can now see qualitatively why the overlap integral should be greater for the B^{12} decay than for the N^{12} decay. Due to the coulomb interaction, N^{12} is just barely bound with respect to $C^{11} + p$, the binding energy being 0.49 Mev. The binding energy for B^{12} with respect to $B^{11} + n$ is 3.37 Mev, which is much larger. This means that the wave function $\Psi_p(C^{11})$ will be more spread out in space than the wave function $\Psi_n(B^{11})$. Since C^{12} is tightly bound with respect to both $B^{11} + p$ and $C^{11} + n$, the binding energies being 15.956 Mev and 18.721 Mev respectively, both wave functions $\Psi_p(B^{11})$ and $\Psi_n(C^{11})$ will be very restricted in space. This means that $\int \Psi_p^*(B^{11})\Psi_n(B^{11})\, d\tau$ will be greater than $\int \Psi_n^*(C^{11})\Psi_p(C^{11})\, d\tau$ and explains qualitatively the fact that the matrix element for the B^{12} decay is greater than the matrix element for the N^{12} decay.

As has been mentioned, a calculation based on the above idea is now in progress. Hopefully, this calculation will be able to predict the value 1.14 for $|\int \sigma|^2(B^{12})/|\int \sigma|^2(N^{12})$ or at least show that a 14% difference in the two matrix elements is not unreasonably large.

It would be desirable, of course, to find examples of mirror decays in the light nuclei analogous to the B^{12}-N^{12} pair and to compare the ft values for these decays to see if a similar difference in the matrix elements exists. Unfortunately, there are no good possibilities available for comparison. The decays of Li^8 and B^8 to the 2.9 Mev state of Be^8 might appear to offer some chance for a comparison, but the width of the 2.9 Mev state in Be^8 (1.5 Mev) throws doubt on whether a comparison of the matrix elements for the Li^8 and B^8 decays would be meaningful. It is doubtful whether we are even justified in talking about a matrix element for these decays, since the concept is valid only when the final state is sharp.[20]

In conclusion, then, we may say that the mirror decays of B^{12} and N^{12} to the ground state of C^{12} offer a unique possibility for a meaningful comparison of two nuclear matrix elements. We feel that a difference of 14% in these two matrix elements is well established experimentally, and that a quantitative explanation of this difference is called for.

APPENDIX I

Effects of Background and Dead Time on a Half-life Measurement

Suppose that we have followed the experimental procedure outlined in section III of this thesis for making a half-life measurement and have obtained the set of numbers n_i, $i = 0, 1, \ldots, m$, where n_i = no. of counts recorded in the time interval $t_i \leq t \leq t_{i+1}$, $t_o = 0$, and the time intervals are all equal. We assume for the moment that no sources of experimental error such as background or dead time are present. To determine the half-life $t_{1/2}$, we make a least squares fit of the points n_i to the expression:

$$\ln n_i = A - \lambda t_i \tag{1}$$

and determine λ. The half-life is given by $t_{1/2} = \ln 2/\lambda$.

We now consider the possibility that sources of error are present in the experimental measurement. The set of numbers which we will obtain differs from the true set n_i and we will call this set n_i'. If we fit this set by least squares to the expression:

$$\ln n_i' = A' - \lambda' t_i \tag{2}$$

we will obtain some value of λ' which is not equal to the true value λ for the decay. We now ask ourselves this question: can we derive an expression for $\left(\frac{\lambda-\lambda'}{\lambda}\right)$ as a function of the relevant quantities describing the sources of experimental error? The reason for doing this can best be understood from section IV of this thesis, where the formulas which we will derive are put to use in an actual case. We will consider

two sources of experimental error: the presence of a constant background and loss of counts due to dead time.

Case (1). Constant background. If a constant background per time interval, n_b, is present in the half-life measurement, we can write:

$$n_i' = n_i + n_b \tag{3}$$

Neglecting the statistical variations which would be present in an actual set of experimental numbers, we assume

$$n_i = n_o e^{-\lambda t_i} \quad ; \quad t_i = ai \tag{4}$$

The parameter a has the dimensions of time, and $t_{i+1} - t_i = a$. If we assume $(n_b/n_i) \ll 1$, we can write:

$$\ln n_i' = \ln n_i + \frac{n_b}{n_i} = \ln n_o - \lambda t_i + \frac{n_b}{n_i} \tag{5}$$

We now make a least squares fit of $\ln n_i'$ to expression 2. This is accomplished by minimizing the quantity:

$$\sum_{i=0}^{m} \frac{[\ln n_i' - A' + \lambda' t_i]^2}{\sigma^2_{\ln n_i'}} \tag{6}$$

and we define $\sigma_{\ln n_i'}$ by:

$$\sigma_{\ln n_i'} \approx \sigma_{\ln n_i} \approx \frac{1}{n_i^{1/2}} \tag{7}$$

Using equations 5 and 7, we can put expression 6 in the form:

$$\sum_{i=0}^{m} n_i [(\ln n_o - A') - (\lambda - \lambda')t_i + \frac{n_b}{n_i}]^2 \tag{8}$$

The procedure which follows is simplified if we define a quantity $\bar{t}$ such that:

$$\sum_{i=0}^{m} n_i(t_i - \bar{t}) = 0 \tag{9}$$

and write expression 8 as:

$$\sum_{i=0}^{m} n_i \left[A'' - (\lambda - \lambda')(t_i - \bar{t}) + \frac{n_b}{n_i} \right]^2 \tag{10}$$

To minimize expression 10 with respect to λ', we take the partial derivative with respect to λ' and set this equal to zero. This gives:

$$\left(\frac{\lambda-\lambda'}{\lambda}\right)_{\text{background}} = \frac{1}{\lambda} \frac{\sum_{i=0}^{m} \left(\frac{n_b}{n_i}\right) n_i(t_i - \bar{t})}{\sum_{i=0}^{m} n_i(t_i - \bar{t})^2} \tag{11}$$

If $\left(\frac{\lambda-\lambda'}{\lambda}\right) \ll 1$, we can replace this quantity by $\left(\frac{t_{1/2}' - t_{1/2}}{t_{1/2}}\right)$ in equation 11.

Case (2) Dead time. If counts are lost in each time interval due to dead time, we can write:

$$n_i' = n_i - c_d n_i^2 \tag{12}$$

analogous to equation 3. c_d is a constant. The equation corresponding to equation 5, if we assume $c_d n_i \ll 1$, is:

$$\ln n_i' = \ln n_i - c_d n_i = \ln n_o - \lambda t_i - c_d n_i \tag{13}$$

The equation analogous to equation 11, which can be derived by following the same procedure used to derive equation 11, is:

$$\left(\frac{\lambda-\lambda'}{\lambda}\right)_{\text{dead time}} = -\frac{1}{\lambda}\,\frac{\sum_{i=0}^{m}(c_d n_i)n_i(t_i-\bar{t})}{\sum_{i=0}^{m} n_i(t_i-\bar{t})^2} \tag{14}$$

To evaluate equations 11 and 14, we must compute the sums $\sum_{i=0}^{m}(t_i-\bar{t})$, $\sum_{i=0}^{m} n_i(t_i-\bar{t})^2$, and $\sum_{i=0}^{m} n_i^2(t_i-\bar{t})$, where n_i and t_i are given by equation 4 and $\bar{t}$ is given by equation 9. This involves computing sums of the form $\sum_{i=0}^{m} e^{-\lambda i}$, $\sum_{i=0}^{m} ie^{-\lambda i}$, and $\sum_{i=0}^{m} i^2 e^{-\lambda i}$. The procedure is straightforward, and we will give only the results:

$$\bar{t} = \frac{\sum_{i=0}^{m} n_i t_i}{\sum_{i=0}^{m} n_i} = \frac{ae^{-a\lambda}(1-(m+1)e^{-am\lambda}+me^{-a(m+1)\lambda})}{(1-e^{-a\lambda})(1-e^{-a(m+1)\lambda})}$$

$$\sum_{i=0}^{m}(t_i-\bar{t}) = (m+1)\left(\frac{am}{2}-\bar{t}\right)$$

$$\sum_{i=0}^{m} n_i(t_i-\bar{t})^2 = \frac{n_o a^2 e^{-a\lambda}[(1-e^{-a(m+1)\lambda})^2-(m+1)^2(1-e^{-a\lambda})^2 e^{-am\lambda}]}{(1-e^{-a\lambda})^3(1-e^{-a(m+1)\lambda})} \tag{15}$$

$$\sum_{i=0}^{m} n_i^2(t_i-\bar{t}) = \frac{n_o^2 a[(m+1)(1-e^{-2a\lambda})e^{-a(m+1)\lambda}-e^{-a\lambda}(1-e^{-2a(m+1)\lambda})]}{(1-e^{-2a\lambda})^2}$$

Formulas 11, 14, and 15 depend only on the assumptions $\frac{n_b}{n_i} \ll 1$ and $c_d n_i \ll 1$. If we make the additional restriction $\lambda a \ll 1$, i.e. $a \ll t_{1/2}$, we can reduce equations 11 and 14 to simple expressions in two special cases which are useful for the discussion in section IV of the thesis. In the case $\lambda am = \ln 2$, i.e. where the points cover exactly one half-life, equation 11 becomes

$$\left(\frac{\lambda - \lambda'}{\lambda}\right)_{\text{background}} \approx 1.4 \frac{n_b}{n_o} \tag{16}$$

and equation 14 becomes:

$$\left(\frac{\lambda - \lambda'}{\lambda}\right)_{\text{dead time}} \approx 0.5\, c_d n_o \tag{17}$$

In the case $\lambda am \gg 1$, equation 11 becomes:

$$\left(\frac{\lambda - \lambda'}{\lambda}\right)_{\text{background}} \approx \frac{n_b}{n_o}\left[\frac{m^2 a^2 \lambda^2}{2}\right] \tag{18}$$

and equation 14 becomes:

$$\left(\frac{\lambda - \lambda'}{\lambda}\right)_{\text{dead time}} \approx 0.25\, c_d n_o \tag{19}$$

APPENDIX II

The Effect of a Change in Phototube Gain with Counting Rate on a Half-life Measurement

The discussion in this appendix refers specifically to the present experiment, in particular to the experimental technique described in section III. We assume further that the total gain change is small over the range of counting rates in the experimental measurement. Referring to fig. 9 or fig. 14, we designate the gain at zero counting rate by G and assume the linear dependence $G_i = G(1 + \epsilon n_i)$, where G_i is the gain at the counting rate in channel i of fig. 9, and n_i is the number of counts in channel i. The shape of the beta spectrum is shown in fig. 2, and the effect of a gain change on this spectrum is illustrated in fig. 15. In fig. 15 the solid curve indicates the beta spectrum for gain G and the dotted curve indicates the beta spectrum for gain G_i. The points a and a_i show the location of the beta peak for the solid and the dotted curves respectively. We have $\frac{G_i - G}{G} = \frac{a_i - a}{a} = \epsilon n_i$. Point b corresponds to the discriminator bias, and b_i is chosen so that $\frac{b_i - b}{b} = \frac{a_i - a}{a}$. We designate the area under the solid curve above b by A, and the area under the solid curve from b to b_i by A'. The fraction by which the number of counts in channel i of fig. 9 is increased (or decreased) as a result of the gain change of the phototube can be written as

$$\frac{\Delta n_i}{n_i} = \frac{A'}{A} = \frac{\epsilon bh}{A} n_i = c_g n_i; \quad \Delta n_i = c_g n_i^2 \tag{1}$$

For the beta spectrum of fig. 2, $\frac{bh}{A} = 0.3$ so $c_g = 0.3\epsilon$. The gain

change results in a gain of counts in channel i if ϵ is positive and in a loss of counts if ϵ is negative. The further analysis of the per cent error introduced into the half-life measurement is identical to the discussion of dead time given in appendix I, since equation 1 is analogous to equation 12 of appendix I, and equations 14, 17, and 19 of appendix I are applicable if c_d is replaced by $-c_g$.

REFERENCES

(1) R. A. Becker and E. R. Gaerttner, Phys. Rev. 56, 854 (1939).

(2) J. V. Jelly and E. B. Paul, Proc. Cam. Phil. Soc. 44, 133 (1948).

(3) P. Bretonneau, Comptes Rendus 236, 913 (1953).

(4) B. C. Cook, Phys. Rev. 106, 300 (1957).

(5) E. Norbeck, Bull. Am. Phys. Soc. 1, 329 (1956).

(6) B. J. Farmer and C. M. Class, Bull. Am. Phys. Soc. 4, 278 (1959).

(7) R. W. Peterson and N. W. Glass, Los Alamos, Private Communication (1962).

(8) L. W. Alvarez, Phys. Rev. 75, 1815 (1949).

(9) H. Weidenmuller, Notes on Theoretical Nuclear Physics, California Institute of Technology, (1962).

(10) Tables for the Analysis of Beta Spectra, National Bureau of Standards Applied Mathematics Series, No. 13 (1952).

(11) M. Morita, Phys. Rev. 113, 1584 (1959).

(12) A. Schwarchild, Bull. Am. Phys. Soc. 4, 79 (1959).

(13) M. Gell-Mann and S. M. Berman, Phys. Rev. Letters 3, 99 (1959).

(14) J. Overley, Ph.D. Thesis, California Institute of Technology (1960).

(15) F. Everling, L. A. Konig, J. H. E. Mattauch, and A. H. Wapstra, Nucl. Phys. 15, 342 (1960).

(16) F. Ajzenberg-Selove, M. L. Bullock, and E. Almqvist, Phys. Rev. 108, 1284 (1957).

(17) F. C. Michel, Ph.D. Thesis, California Institute of Technology (1962).

(18) F. Ajzenberg-Selove and T. Lauritsen, Nucl. Phys. 11, 5 (1959).

(19) P. M. Endt and C. M. Braams, Revs. Mod. Phys. 29, 683 (1957).

(20) T. A. Griffy and L. C. Biedenharn, Nucl. Phys. 15, 636 (1960).

(21) N. W. Glass, R. W. Peterson, and R. K. Smith, Bull. Am. Phys. Soc. 6, 49 (1961).

(22) C. W. Cook, W. A. Fowler, C. C. Lauritsen, and T. Lauritsen, Phys. Rev. 107, 508 (1957).

Figure 1. Cross section of target chamber. The plane of the cross section is horizontal, and contains the beam. The number code has the following interpretation: (1) target chamber wall (steel), (2) lucite window, (3 and 4) 2" brass fitting connecting target chamber to rest of vacuum system, (5) target backing, (6) aluminum shield in front of crystal, (7) anthracene crystal, (8) phototube, (9) light shield for phototube, (10) arrow indicates beam direction, (11) O-ring grooves, (12) electron suppressor ring. Fig. 1 is drawn approximately to scale. (See page 89.)

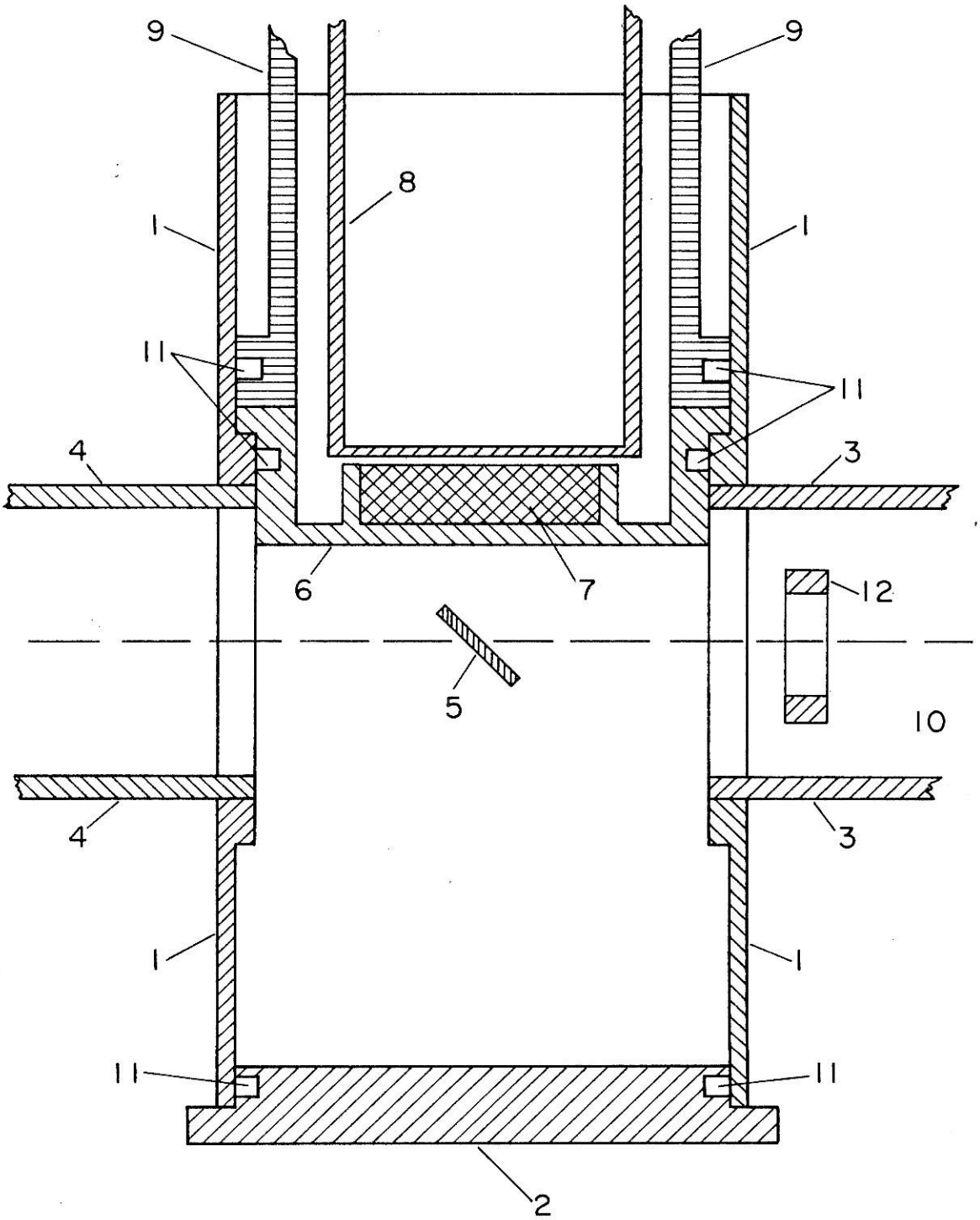
9
9
8
1
1
11
11
4
3
6
7
12
5
10
4
3
1
1
11
11
2

Figure 2. Pulse height spectrum of beta particles from the decay of B^{12}. The spectrum for the N^{12} decay has a similar shape. Since the anthracene crystal is 2 Mev thick to beta particles, the peak in the figure corresponds to an energy loss of 2 Mev in the crystal. The arrow indicates the position at which the integral discriminator bias was set in making a half-life measurement. (See pages 90, 94 and 120.)

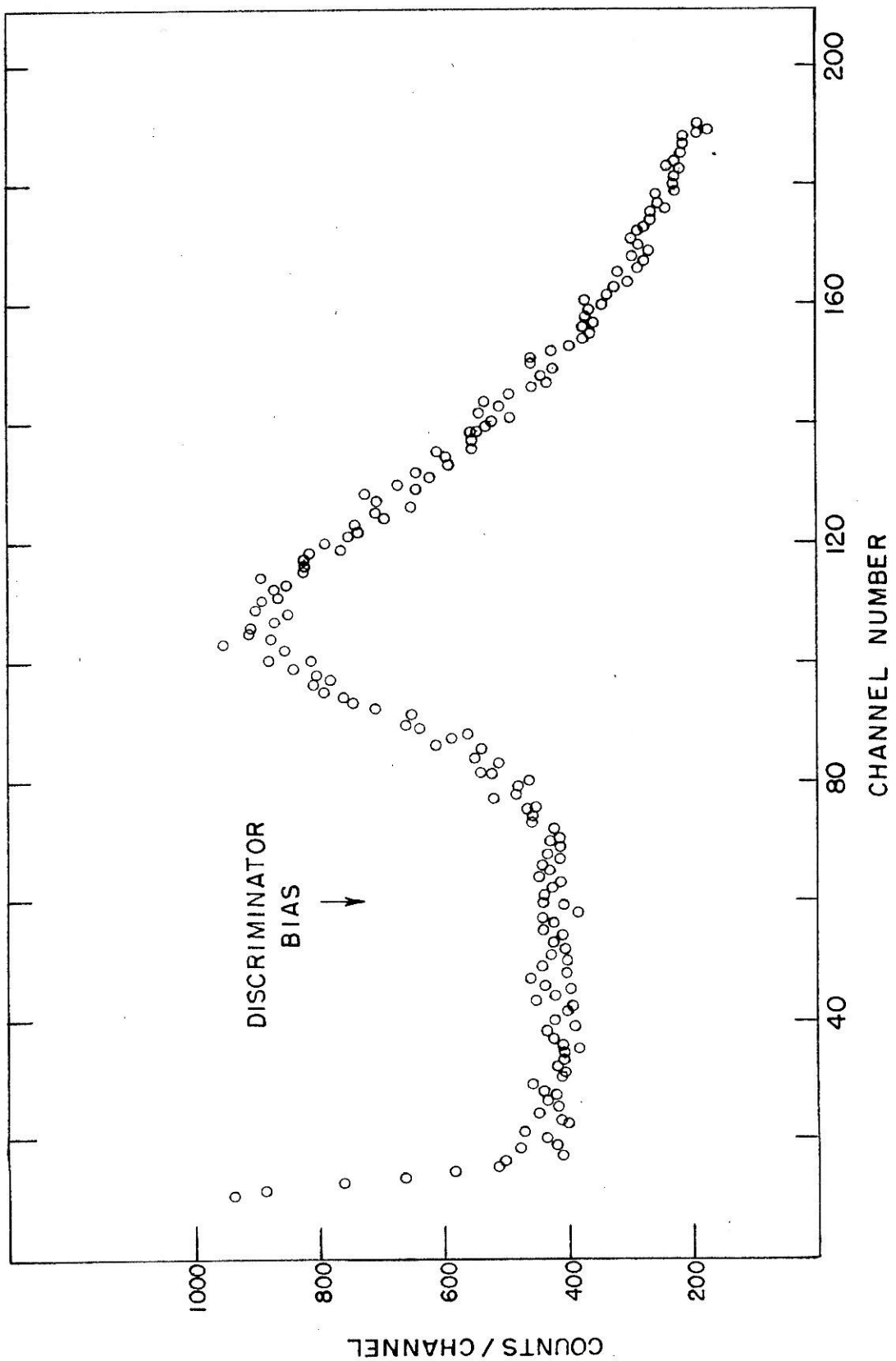
DISCRIMINATOR
BIAS
COUNTS / CHANNEL
1000
800
600
400
200
40
80
120
160
200
CHANNEL NUMBER

Figure 3. Block diagram of electronic timer. The wave forms at different points in the circuit have been designated by the numbers (1) through (4) and the time relationship between these wave forms is shown on the scale at the bottom of the figure. There are six scales of 10, and the six position switch makes it possible to take the output from any one of the six. A complete circuit diagram of this piece of equipment is included in the Kellogg file. (See page 91.)

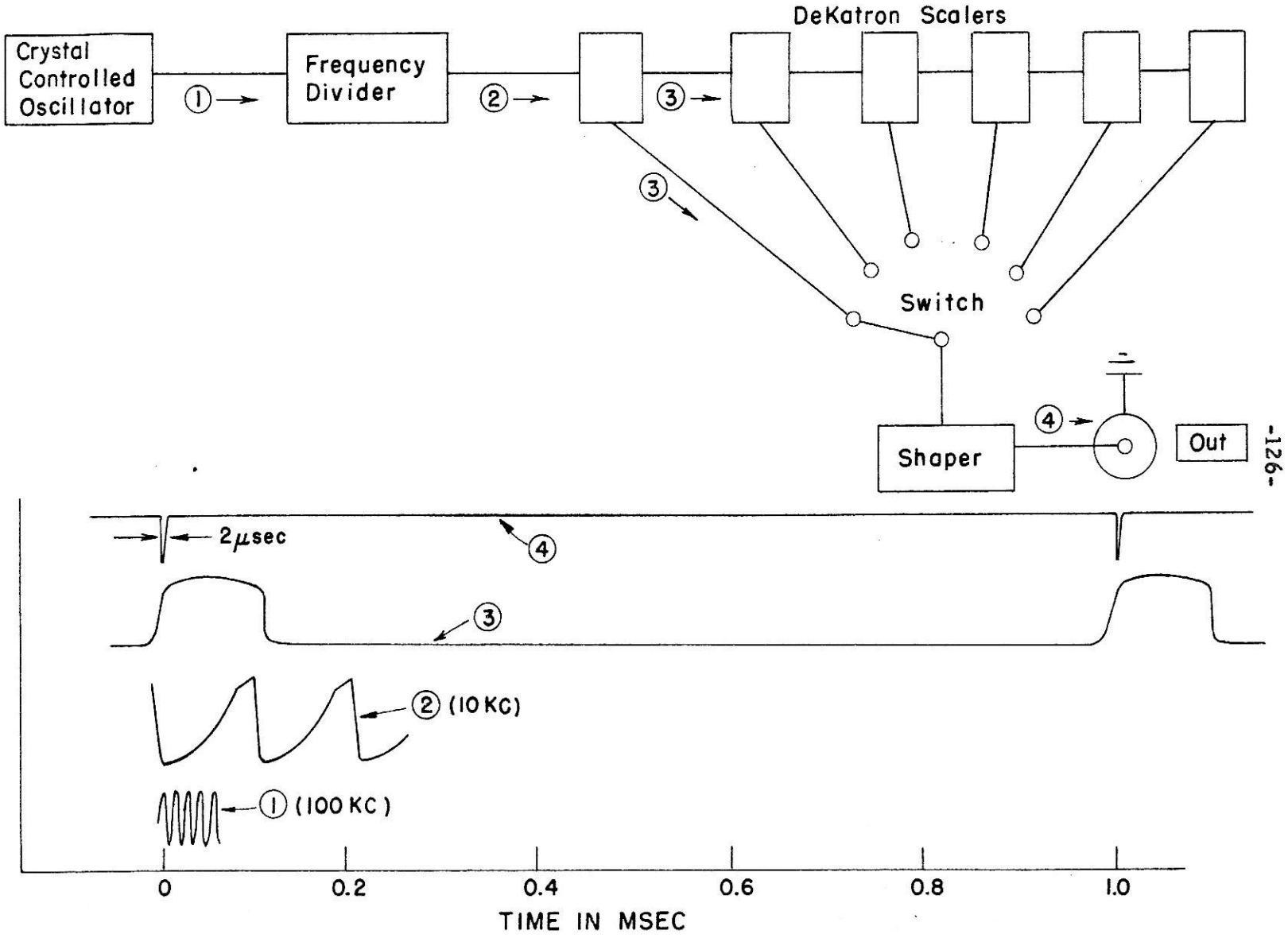
DeKatron Scalers
Crystal Controlled Oscillator
①
Frequency Divider
②
③
③
Switch
④
Shaper
Out
2μsec
④
③
② (10 KC)
① (100 KC)
0
0.2
0.4
0.6
0.8
1.0
TIME IN MSEC

Figure 4. Circuit arrangement for obtaining pulse height spectrum of beta particles. The beam is chopped with the 60 cycle chopper. The wave forms at different points in the circuit are designated by the numbers (1) through (3), and the time relationship of these wave forms is shown on the scale at the bottom of the figure. Figure 5 contains a complete diagram of the phototube chopper and phototube bias network. (See pages 91 and 94.)

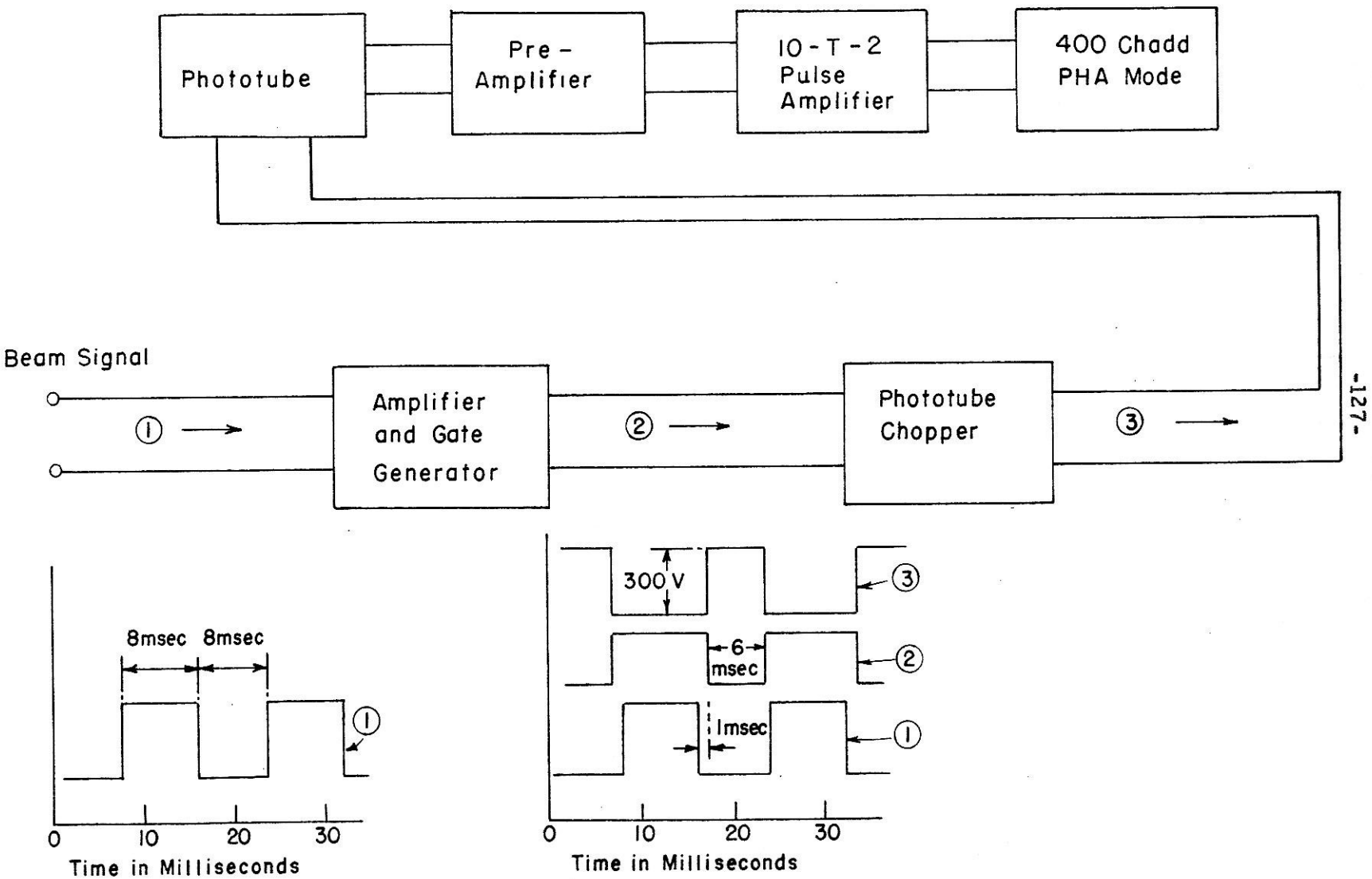
Phototube
Pre - Amplifier
10 - T - 2 Pulse Amplifier
400 Chadd PHA Mode
Beam Signal
①
Amplifier and Gate Generator
②
Phototube Chopper
③
8msec 8msec
①
0 10 20 30
Time in Milliseconds
300 V
③
6 msec
②
1msec
①
0 10 20 30
Time in Milliseconds

Figure 5. Circuit diagram of phototube chopper and phototube bias network. (See page 94.)

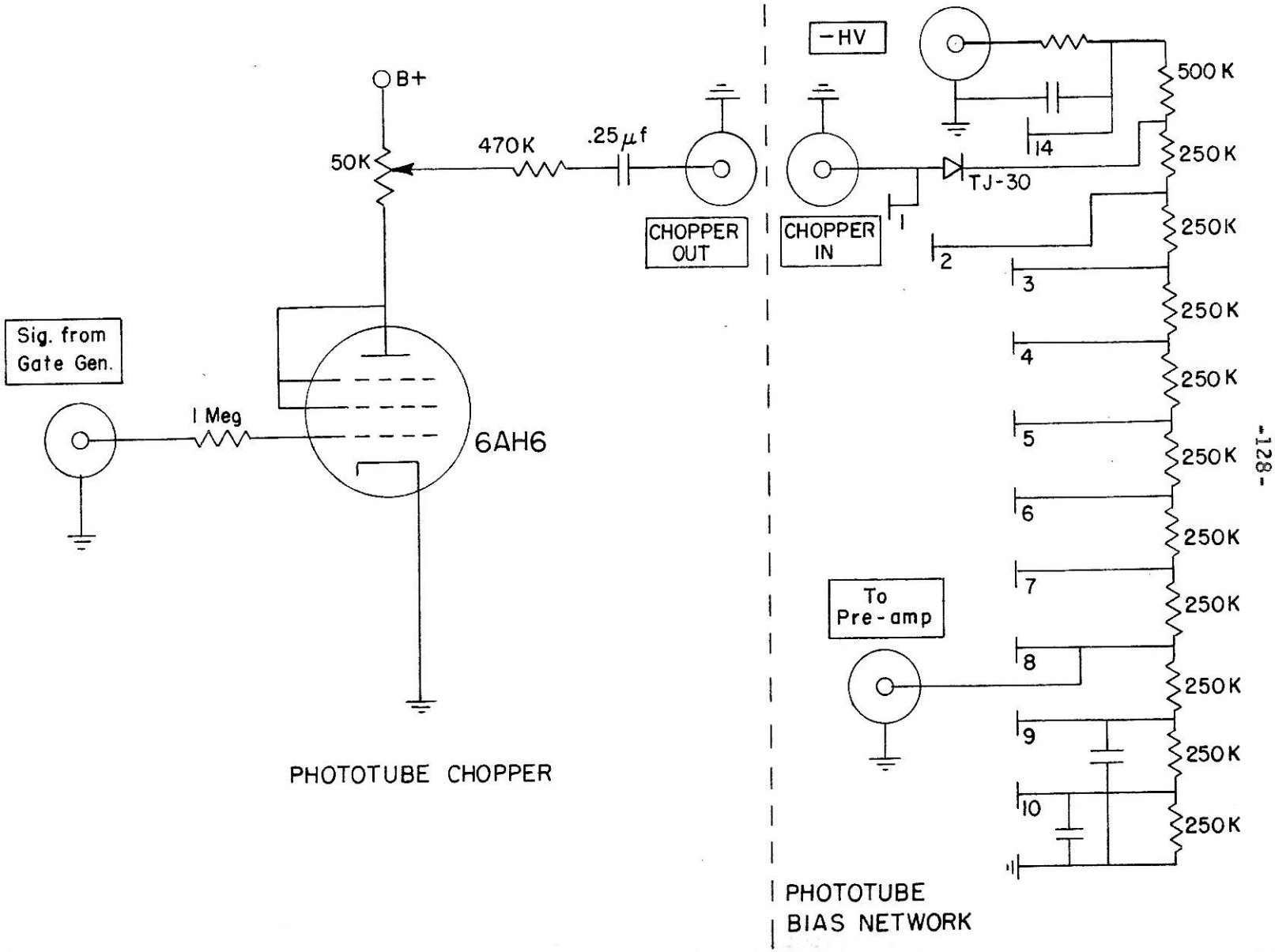
B+
50K
470K
.25μf
CHOPPER OUT
CHOPPER IN
-HV
500 K
250K
250K
250K
250K
250K
250K
250K
250K
250K
250K
TJ-30
14
1
2
3
4
5
6
7
8
9
10
11
Sig. from Gate Gen.
1 Meg
6AH6
To Pre-amp
PHOTOTUBE CHOPPER
PHOTOTUBE BIAS NETWORK

Figure 6. Circuit arrangement for making a half-life measurement. The wave forms at different points in the circuit are designated by the numbers (1) through (5) and shown at the bottom of the figure. Signal (5) from the timer is not synchronized with signals (1) through (4). The output from the D. C. Gate remains at 0 volts until the position of the switch is changed. It then returns to - 20 volts in coincidence with the next pulse from (3). A diagram of the Address Reset and D. C. Gate circuits is shown in fig. 7. (See pages 91, 94 ff.)

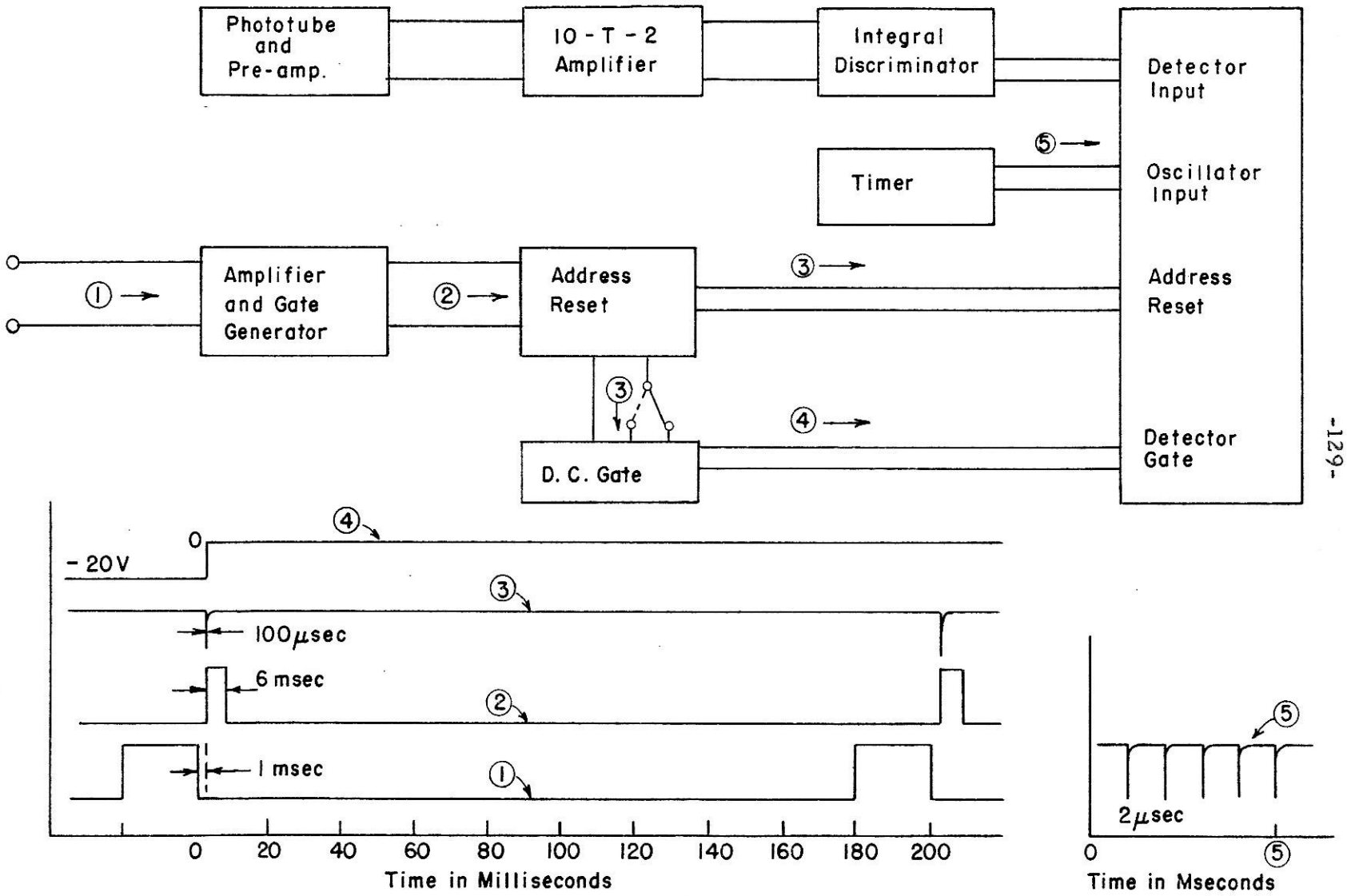
Phototube and Pre-amp.
10 - T - 2 Amplifier
Integral Discriminator
Detector Input
Timer
Oscillator Input
Amplifier and Gate Generator
Address Reset
Address Reset
D. C. Gate
Detector Gate
- 20V
0
100μsec
6 msec
1 msec
0 20 40 60 80 100 120 140 160 180 200
Time in Milliseconds
2μsec
0
Time in Mseconds

Figure 7. Circuit diagram of Address Reset and D. C. Gate circuits.

(See page 95.)

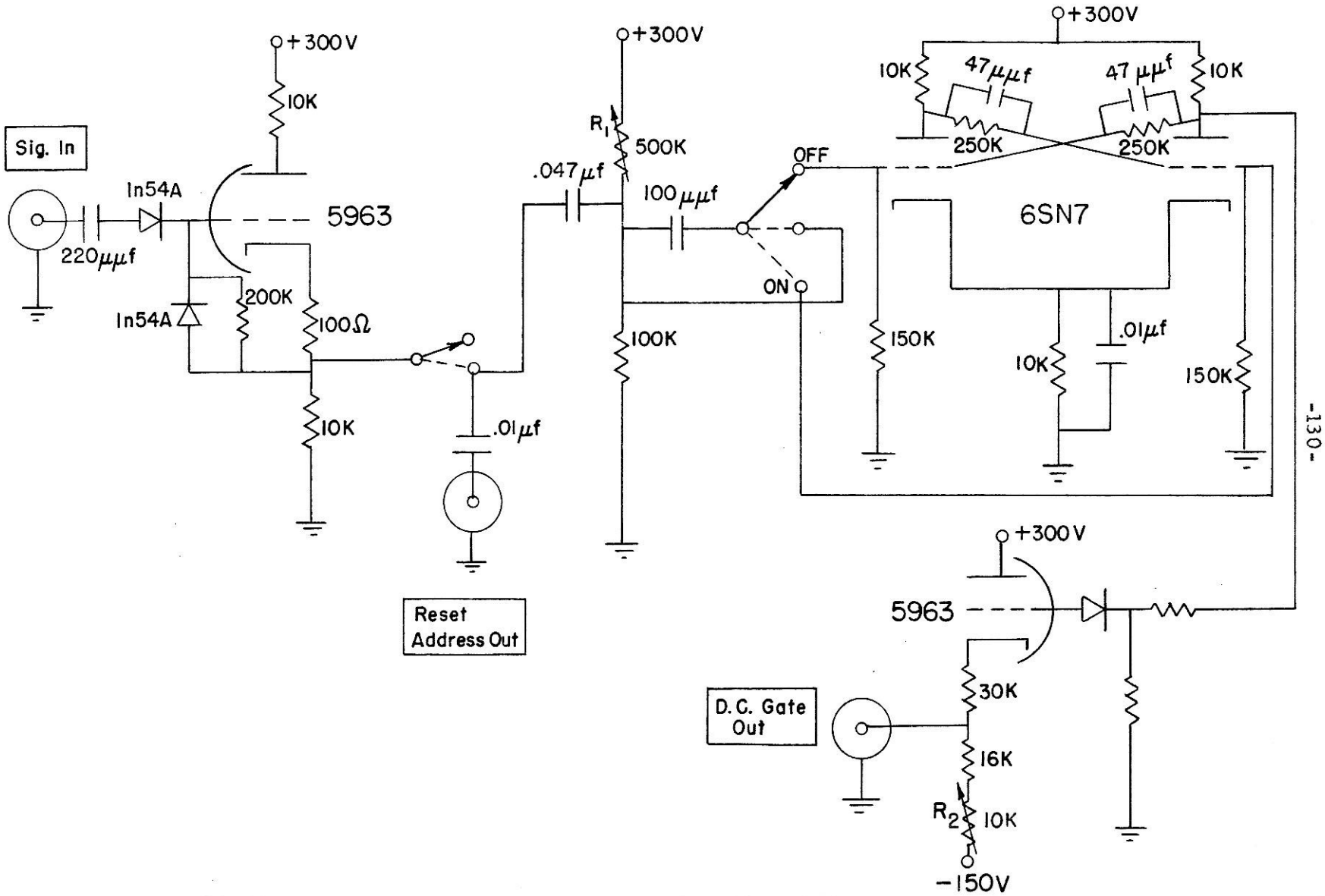
+300V
10K
Sig. In
In54A
5963
220μμf
In54A
200K
100Ω
10K
.01μf
Reset
Address Out
+300V
R1
500K
.047μf
100μμf
OFF
ON
100K
+300V
10K
47μμf
47μμf
10K
250K
250K
6SN7
150K
10K
.01μf
150K
+300V
5963
30K
D.C. Gate
Out
16K
R2
10K
-150V

Figure 8. Counts vs. time for the decay of B^{12} plotted in Cartesian coordinates. The rise beginning at channel 175 is due to the beam's coming on. (See page 96.)

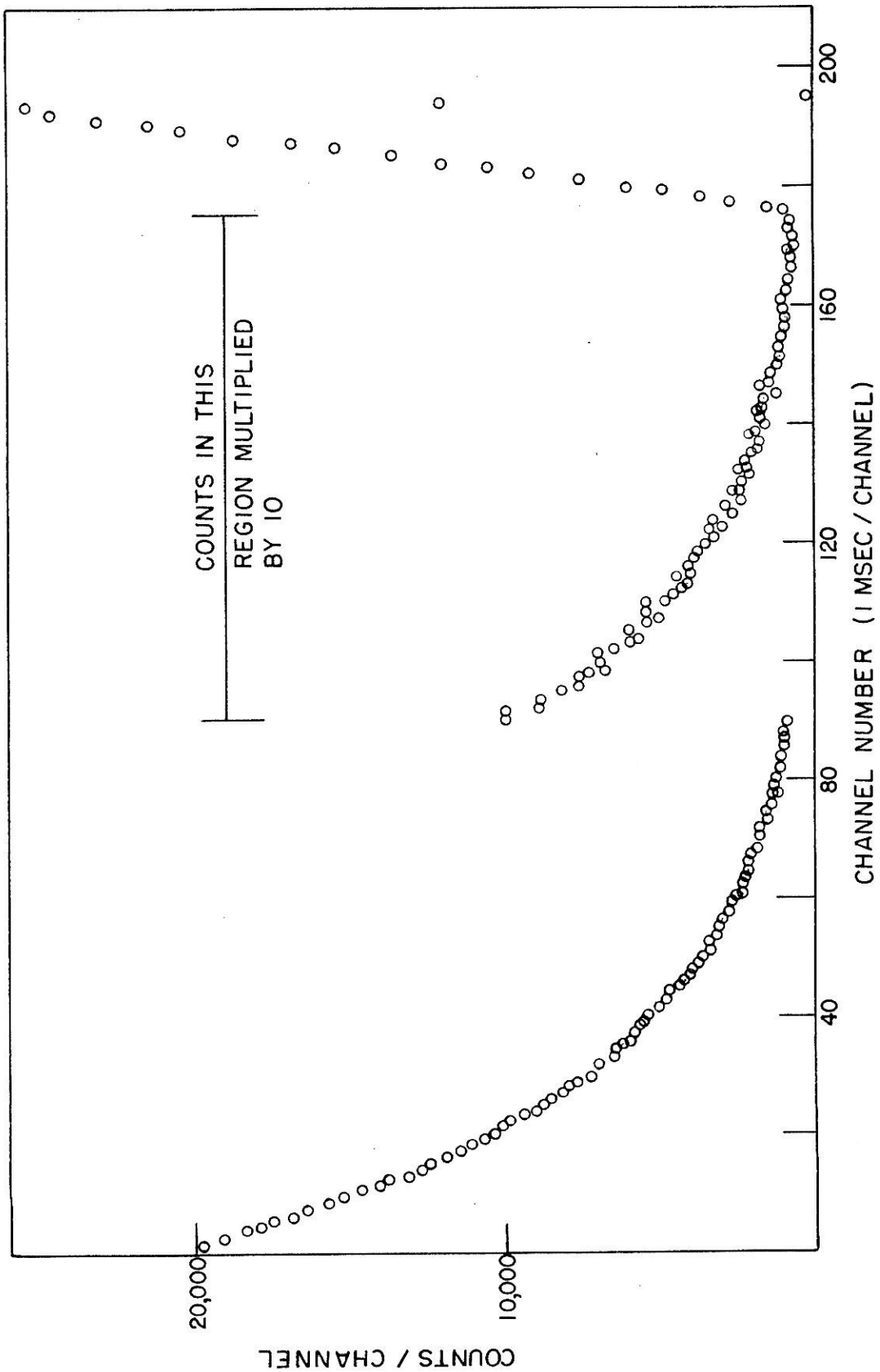
COUNTS IN THIS
REGION MULTIPLIED
BY 10
20,000
10,000
COUNTS / CHANNEL
40
80
120
160
200
CHANNEL NUMBER (1 MSEC / CHANNEL)

Figure 9. Plot of $\ln n_i$ vs. t for the B^{12} decay. This plot is uncorrected for background. The division into three sections, (a), (b), and (c), refers to the discussion in section IV A. (See page 98 ff.)

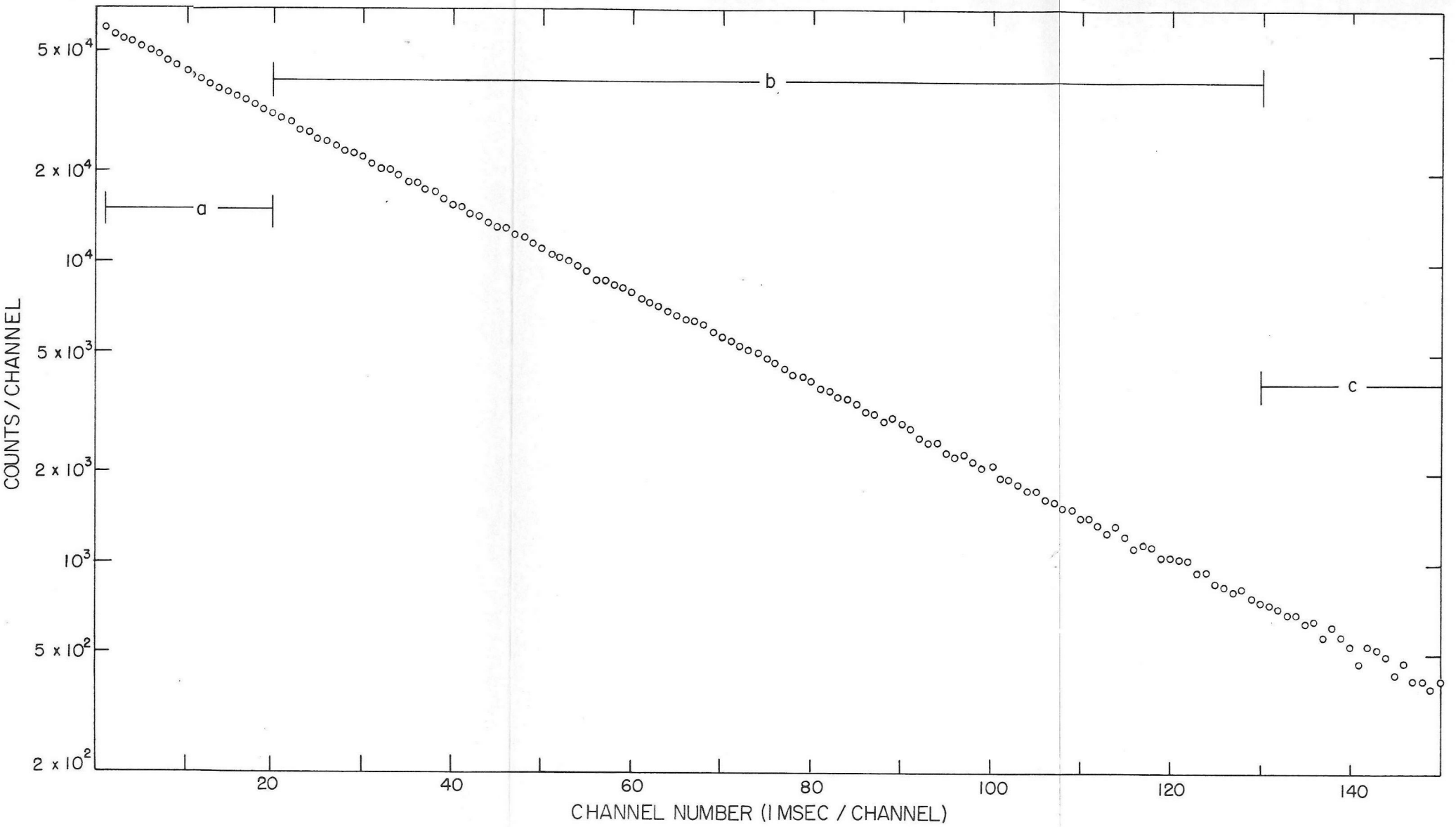
5 x 10^4
2 x 10^4
10^4
5 x 10^3
2 x 10^3
10^3
5 x 10^2
2 x 10^2
COUNTS / CHANNEL
a
b
c
20
40
60
80
100
120
140
CHANNEL NUMBER (1 MSEC / CHANNEL)

Figure 10. Beta particle spectra (B^{12} decay) taken at three different counting rates. There is no apparent change in the position or location of the peak. (See page 102 ff.)

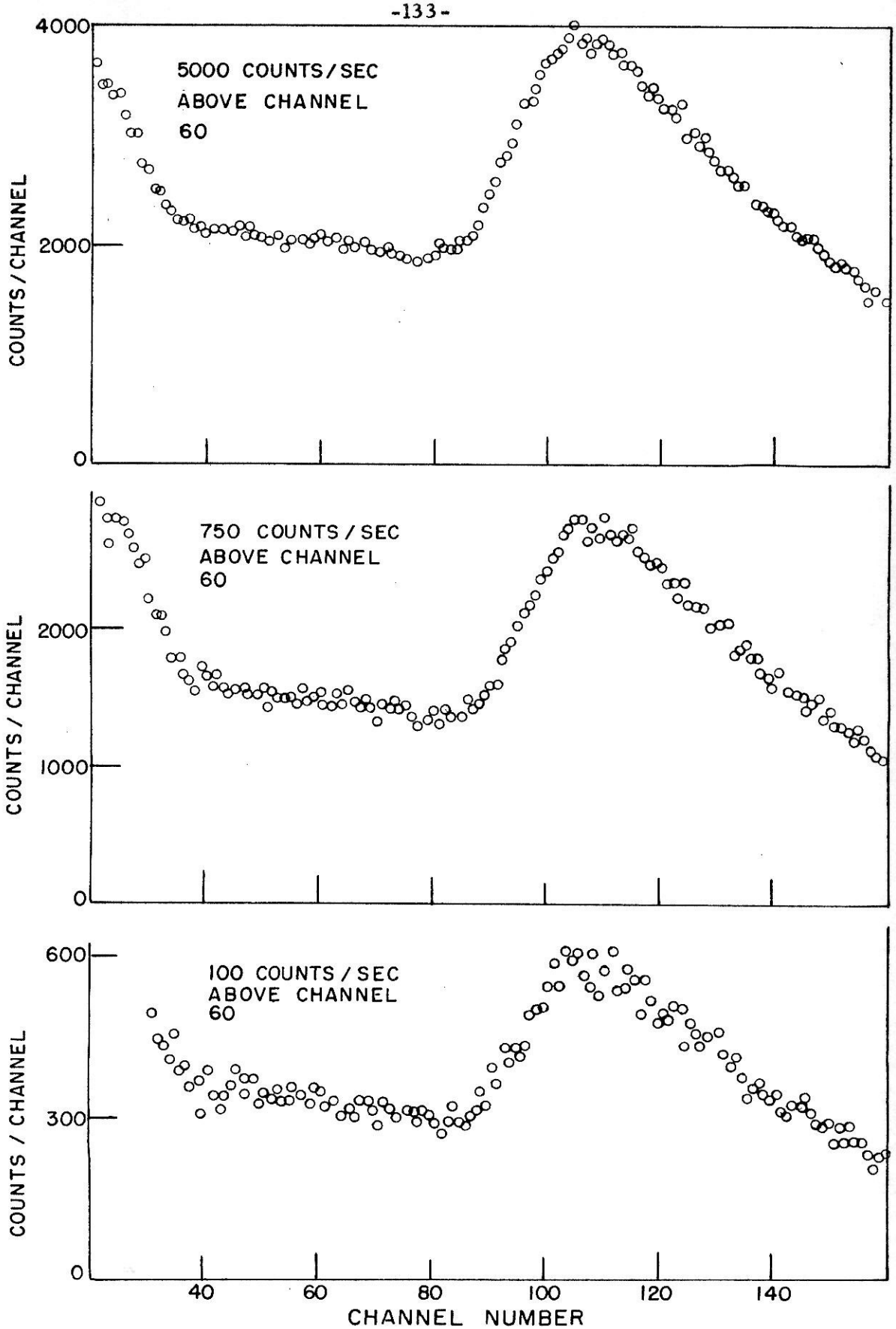
4000
2000
0
COUNTS / CHANNEL
5000 COUNTS / SEC
ABOVE CHANNEL
60
2000
1000
0
COUNTS / CHANNEL
750 COUNTS / SEC
ABOVE CHANNEL
60
600
300
0
COUNTS / CHANNEL
100 COUNTS / SEC
ABOVE CHANNEL
60
40
60
80
100
120
140
CHANNEL NUMBER

Figure 11. Plot of $\ln n_i$ vs. t for N^{12} decay, uncorrected for background. This measurement was made using an enriched B^{10} target. (See page 104 ff.)

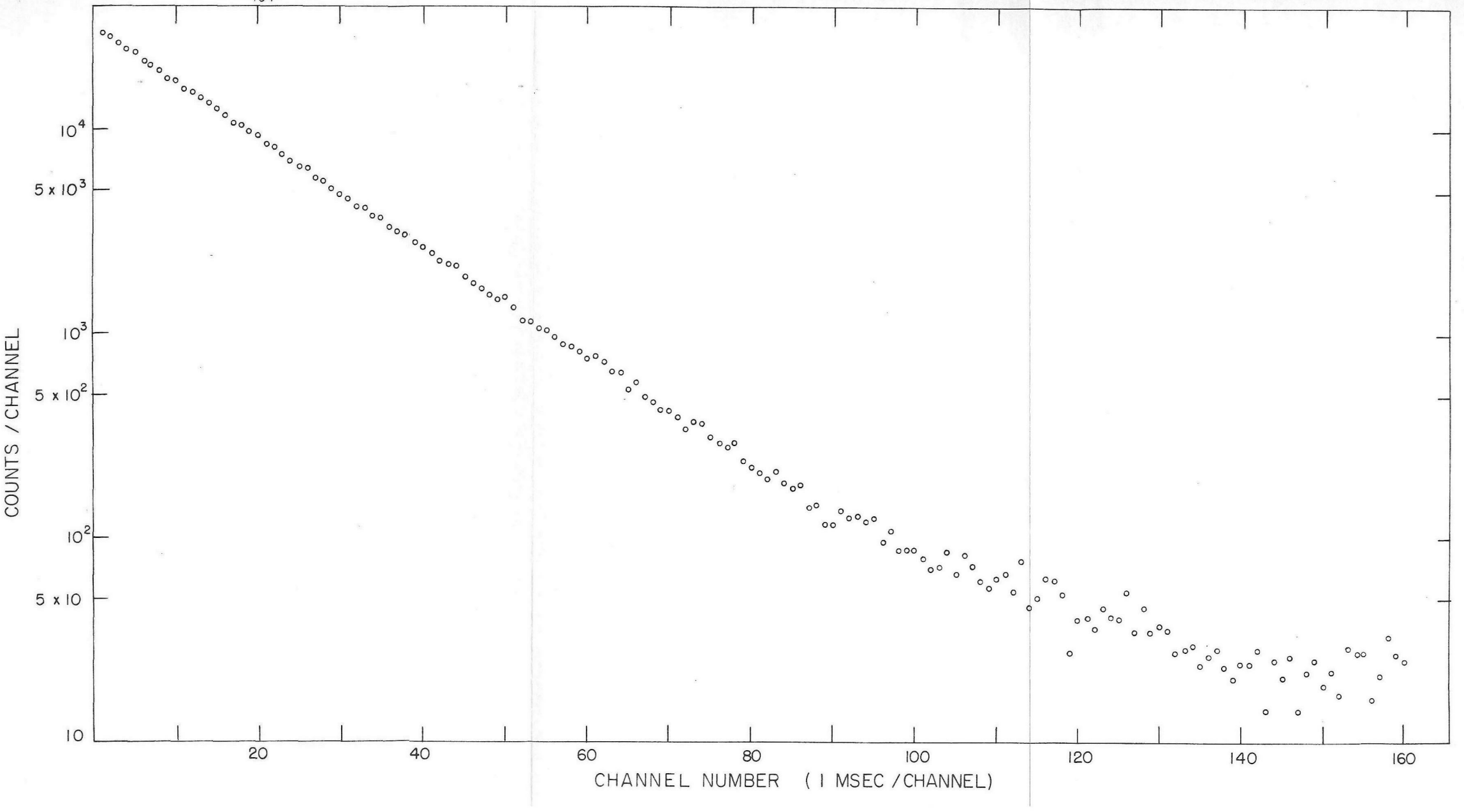
COUNTS / CHANNEL
10^4
5 x 10^3
10^3
5 x 10^2
10^2
5 x 10
10
20
40
60
80
100
120
140
160
CHANNEL NUMBER (1 MSEC / CHANNEL)

Figure 12. Plot of $\ln n_i$ vs. t for N^{12} decay obtained with a natural boron target. (See page 106 ff.)

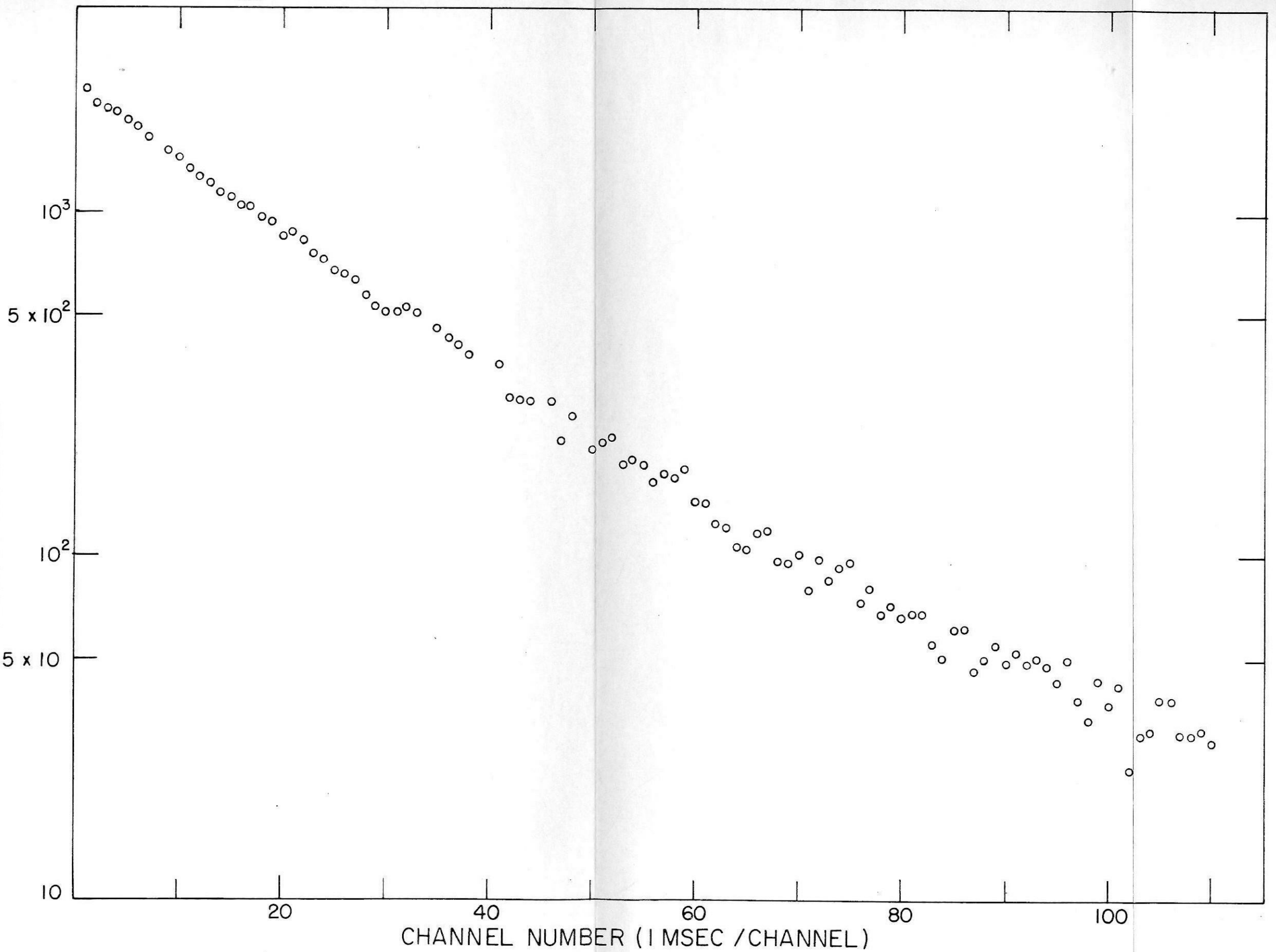
COUNTS / CHANNEL
10³
5 x 10²
10²
5 x 10
10
20
40
60
80
100
CHANNEL NUMBER (1 MSEC / CHANNEL)

Figure 13. Plot of $t_{1/2}(B^{12})_a$ vs. $(B^{12}/N^{12})_a$. The significance of this figure is explained in section IV B. (See page 107.)

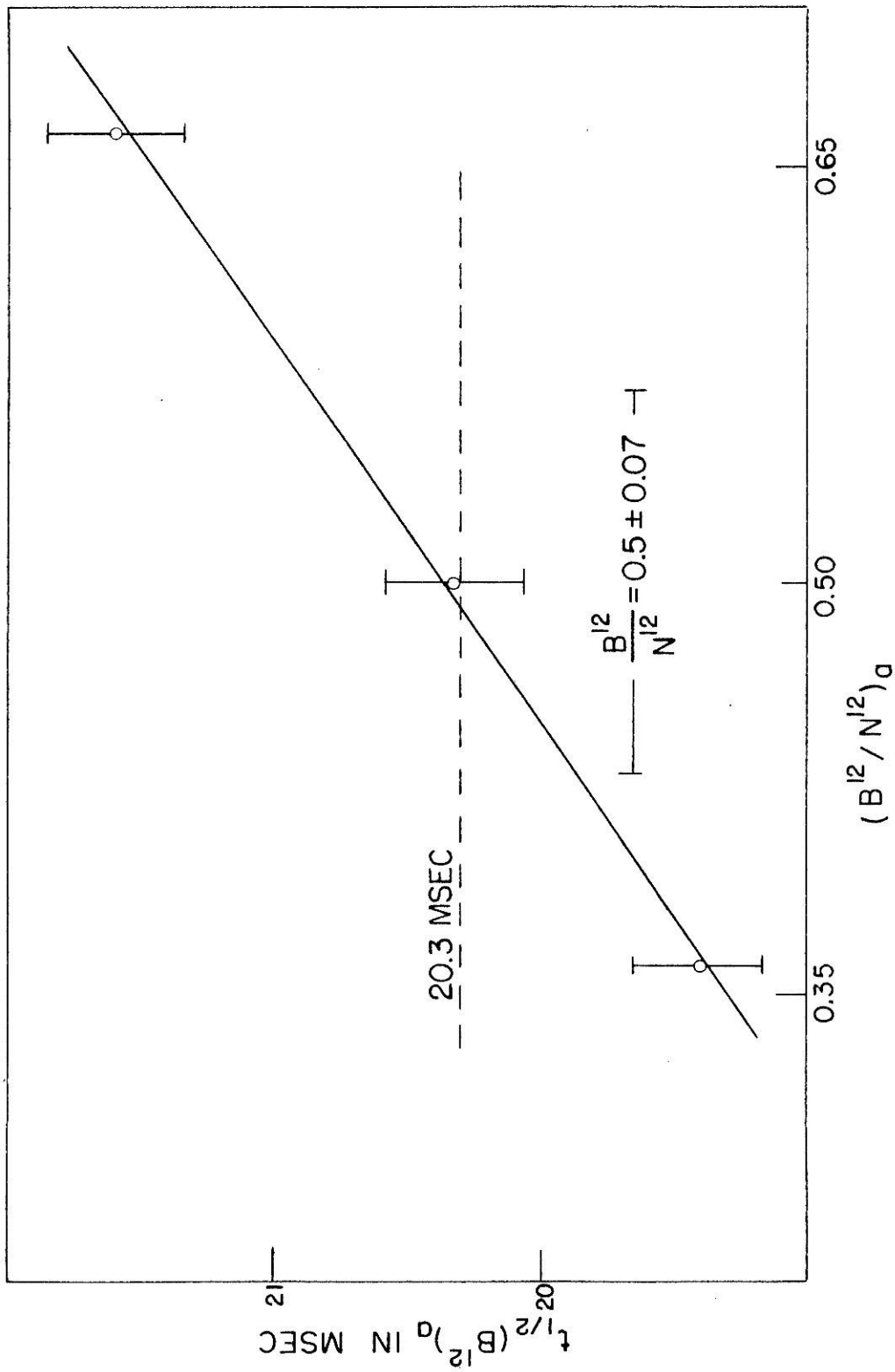
$t_{1/2}(B^{12})_Q$ IN MSEC
21
20
0.35
0.50
0.65
$(B^{12}/N^{12})_Q$
20.3 MSEC
$\frac{B^{12}}{N^{12}} = 0.5 \pm 0.07$

Figure 14. Figure 11 corrected for background. The division into sections (a), (b), and (c) refers to the discussion in section IV B. (See page 107 ff.)

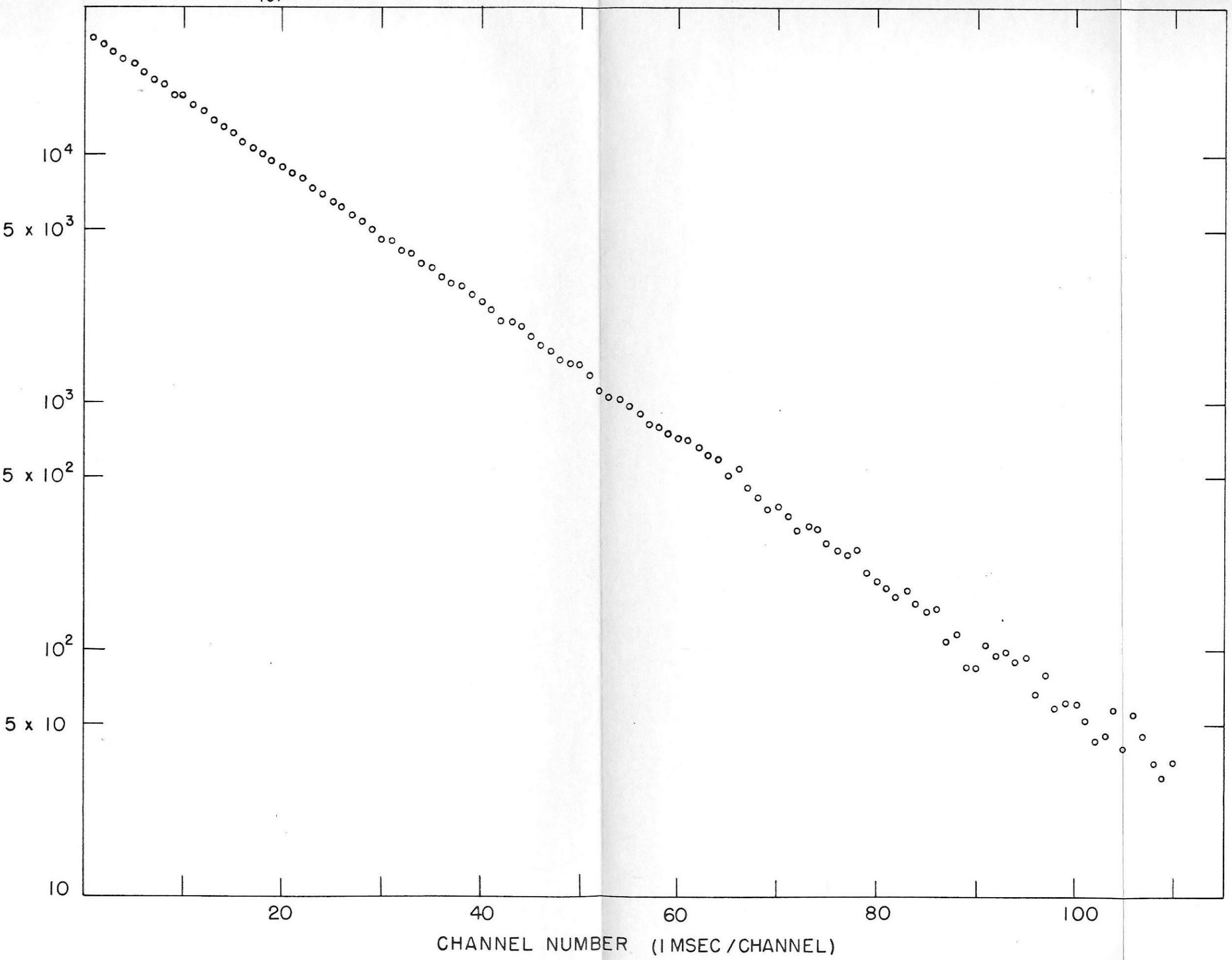
COUNTS / CHANNEL
10⁴
5 x 10³
10³
5 x 10²
10²
5 x 10
10
20
40
60
80
100
CHANNEL NUMBER (1 MSEC / CHANNEL)

Figure 15. Illustration for discussion in appendix II. (See page 120.)

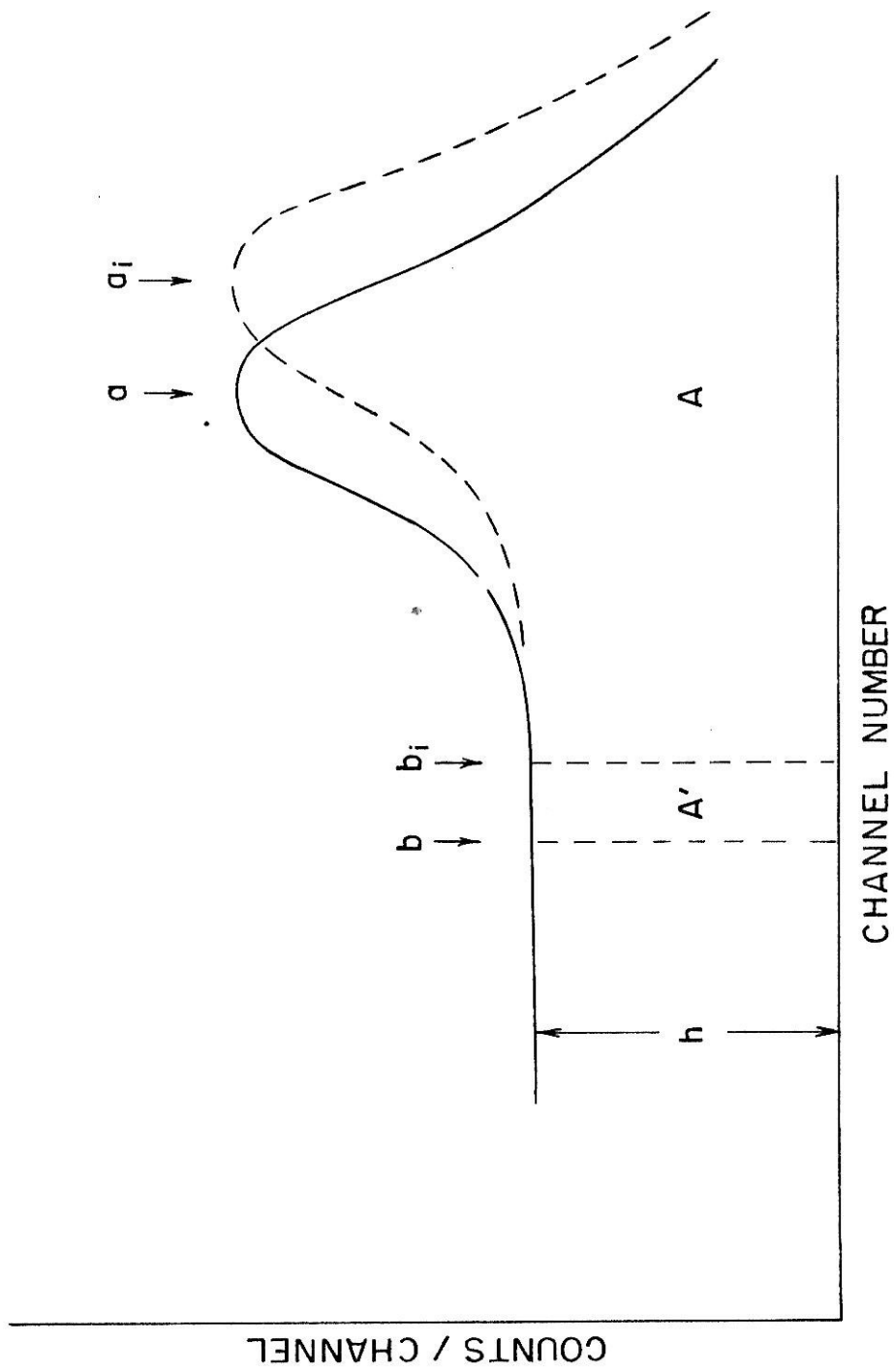
COUNTS / CHANNEL
CHANNEL NUMBER
a_i
a
A
b_i
b
A'
h